Fluctuation Spectroscopy of Single Plasmonic Nanostructures

New perspectives due to improved time resolution

Dissertation

zur Erlangung des Grades
"Doktor der Naturwissenschaften"
am Fachbereich Chemie, Pharmazie und Geowissenschaften
an der Johannes Gutenberg Universität Mainz

Irene Ament

geboren in Frankfurt am Main

Mainz, 2011

JOHANNES GUTENBERG
UNIVERSITÄT MAINZ

Diese Arbeit entstand im Zeitraum März 2008 bis November 2011 am Institut für Physikalische Chemie, Johannes Gutenberg Universität Mainz.

Dekan: [personal data removed]

Erster Gutachter: [personal data removed]
Zweiter Gutachter: [personal data removed]

Tag des Prüfungskolloquiums: 10. Januar 2012

I acknowledge the Carl Zeiss Stiftung for providing me a PhD scholarship.

To my family

It doesn't matter how beautiful your theory is,
it doesn't matter how smart you are.
If it doesn't agree with experiment, it's wrong.
Richard P. Feynman

Abstract

Plasmonic nanoparticles are great candidates for sensing applications with optical read-out. Plasmon sensing is based on the interaction of the nanoparticle with electromagnetic waves where the particle scatters light at its resonance wavelength. This wavelength depends on several intrinsic factors like material, shape and size of the nanoparticle as well as extrinsic factors like the refractive index of the surrounding medium. The latter allows the nanoparticle to be used as a sensor; changes in the proximate environment can be directly monitored by the wavelength of the emitted light. Due to their minuscule size and high sensitivity this allows individual nanoparticles to report on changes in particle coverage.

To use this single particle plasmon sensor for future sensing applications it has to meet the demand for detection of incidents on the single molecule level, such as single molecule sensing or even the detection of conformational changes of a single molecule. Therefore, time resolution and sensitivity have to be enhanced as today's measurement methods for signal read-out are too slow and not sensitive enough to resolve these processes. This thesis presents a new experimental setup, the 'Plasmon Fluctuation Setup', that leads to tremendous improvements in time resolution and sensitivity. This is achieved by implementation of a stronger light source and a more sensitive detector. The new setup has a time resolution in the microsecond regime, an advancement of 4-6 orders of magnitude to previous setups. Its resonance wavelength stability of 0.03 nm, measured with an exposure time of 10 ms, is an improvement of a factor of 20 even though the exposure time is 3000 times shorter than in previous reports. Thus, previously unresolvable wavelength changes of the plasmon sensor induced by minor local environmental alteration can be monitored with extremely high temporal resolution.

Using the 'Plasmon Fluctuation Setup', I can resolve adsorption events of single unlabeled proteins on an individual nanorod. Additionally, I monitored the dynamic evolution of a single protein binding event on a millisecond time scale. This feasibility is of high interest as the role of certain domains in the protein can be probed by a study of modified analytes without the need for labels possibly introducing conformational or characteristic changes to the target. The technique also resolves equilibrium fluctuations in the coverage, opening a window into observing Brownian dynamics of unlabeled macromolecules.

A further topic addressed in this thesis is the usability of the nanoruler, two nanospheres connected with a spacer molecule, as a stiffness sensor for the interparticle linker under strong illumination. Here, I discover a light induced collapse of the nanoruler. Furthermore, I exploit the sensing volume of a fixed nanorod to study unlabeled analytes diffusing around the nanorod at concentrations that are too high for fluorescence correlation spectroscopy but realistic for biological systems. Additionally, local pH sensing with nanoparticles is achieved.

Contents

List of Figures

List of Tables

1 Introduction

Nanotechnology is a relatively young topic for research but has become more and more important over the last decades. Investigation of the number of publications in the Web of Knowledge with 'nanoparticle' as the buzzword reveals an exponential increase since the 1970s. The word 'nano' goes back to either the Greek word 'nannos' or to the Latin word 'nanus'. The translation in both cases is 'dwarf'. In physics, it is therefore used as a prefix to abbreviate values in the order of 10^{-9}. Due to the dramatic increase in surface to volume ratio, nanoparticles can exhibit characteristics totally uncommon for particles of much larger size but of the same material. Examples are higher catalytic efficiencies or higher stability. In a number of commercially available products nanoparticles can already be found. To name only a few of them: In textiles, nanoparticles provide water resistance without significantly reducing breathability and surfaces are designed with nanoparticles to be self-cleaning. Also optical characteristic of nanoparticles are exploited: Sunscreens and cosmetics use titanium dioxide nanoparticles as physical sun blockers as they absorb UV light.

Metal nanoparticles provide strong optical response caused by the light excited quasi-particle - the plasmon. An incoming electromagnetic light wave induces an oscillation of the conduction electrons. If the frequency of the illuminating light matches the eigenfrequency of the electrons, efficient scattering and absorption can be observed.

Romans used metal nanoparticles to color glasses in the 4th century AD even though the origin of the color was not understood then. A nice example is the Lycurgus cup exhibited in the British Museum. Many church windows from the Middle Ages also owe their colors to silver and gold colloids suspended within the glass. One famous example is Sainte Chapelle in Paris [1]. However, it was not until 1857 that Michael Faraday published his pioneering work on the coloring characteristics of colloidal gold. Half a century later (1908) Gustav Mie derived the theory for the particle-light interaction by solving the Maxwell equations for spherical objects. For metal nanoparticles this is important as it quantifies the color observed. In 1912, Richard Gans extended this description to spheroidal shapes. Nowadays, the interaction of light even with complex particle shapes can be solved numerically.

These days, interest in plasmonic nanoparticles has grown tremendously. One major area is sensing, e.g. surface enhanced Raman scattering (SERS) due to strong enhancement at interparticle gaps called hot spots or nanolenses [2]. The use of plasmonics also increases in applied physics like wave guiding technology or the integration of nanoscale components in electronics and optics [3]. The growing demand for data storage could also be met by optical recording mediated by surface plasmons in gold nanorods [4]. Even the fairy tale item 'cloak of invisibility' could become reality by developments in negative refractive index materials [5, 6, 7]. Light-driven nanoscale plasmonic motors have recently been achieved as a step towards nano-machines [8, 9]. Less fiction-like and beneficial to health care are plasmon sensors that test for pregnancy, prostate cancer, heart attacks, or HIV [1]. Here, improvements on the utility for everyday life are an important future task. The requirements are multifaceted, ranging from inexpensiveness, to rapid and accurate read-out to easy handling by inexperienced users. Current research pursues not only sensing but also the potential to include plasmonic particles for cancer treatment. For this, the photo thermal effect in addition to selective binding driven by surface functionalization to malicious cells are aspects [10].

Most plasmon sensors on the market only exploit the presence or absence of nanoparticles and do not yet take advantage of the particle sensitivity to changes in its environment monitored by a resonance wavelength shift. Researchers investigated this possibility in the last decade with the finding that this shift can either be read out from a nanoparticle dispersion or even better from a single particle measurement. Latter one does not suffer from sample polydispersity and senses on the attoliter scale. Therefore it is the method of choice for measurements of individual molecules. So far, this single particle plasmon sensor was used besides others to study molecule coverage of the whole sensor. Time resolution and spectral sensitivity of setups at the beginning of my thesis were too slow and little sensitive to detect a single adsorbing molecule or even its conformational change. Therefore, I maximized the temporal and spectral resolution with which plasmonic spectra can be acquired.
In most common systems to detect a spectrum of a single plasmonic nanoparticle, the major restricting component is the weak light source, typically a halogen lamp. Additionally, condensors are needed to focus a maximum amount of light under a steep angle onto the sample to achieve dark field illumination. Due to the geometry of the condensor the illuminated area is larger than needed and photons are wasted. In contrast, a white light laser provides a collimated beam of light with a high density of photons. With this device, 'dark field'-like illumination of the sample can be achieved easily. The beam is coupled into a prism to obtain total internal reflection at the surface where the sample is deposited. The second major improvement for achieving high time resolution is an electron multiplied charge coupled device (EMCCD) with enhanced sensitivity due to electron multiplication during read-out. If used in combination with the previously mentioned halogen lamps, the time resolution of full spectra can be decreased to approximately 100 ms, while still obtaining reasonably low spectral noise. However, combining the EMCCD with the white light laser, a drastic improvement into the microsecond regime can be achieved.
Following plasmonic spectra with this improved spectral and temporal resolution allows me to use plasmonic nanoparticles as sensors for environmental changes on small time scales, e.g. single unlabeled protein binding events. This ultimate sensitivity has not been reached so far. However, as it will be possible to resolve adsorption processes, conformational changes of proteins and the influence of a slightly altered amino acid sequence of the respective protein, the findings presented here might even affect research of other fields, namely biology. Addition-

ally, the setup allows me to uncover fluctuations in the coverage of the plasmonic sensor, information generally hidden from larger sensors but very useful for studying binding dynamics in equilibrium and non-equilibrium conditions. Thus, not only is the sensor miniaturized but the new principle of fluctuation sensing is introduced to plasmonic sensing.

Before I describe the new setup in detail, Chapter 2 presents the principle theory of plasmons and their optical properties. I start with introducing the theory of Drude and Sommerfeld, a relatively simple model for the motion of electrons in a metal, predicting most features of all metals qualitatively and quantitatively correct. Then I present the concept of plasmon sensing, fundamental for the work of this thesis. Insight into further important features of plasmonic particles, plasmon coupling and nanoparticle heating, are also given. These two effects play a major role for particles in close proximity, a situation I investigated. To have a good understanding of the nanoparticle illumination, I describe the evanescent wave created by total internal reflection, the type of illumination used in the experiments. The chapter concludes with an introduction to optical forces on particles, important for nanoparticles exposed to strong electromagnetic fields.

Prior to more advanced studies with high time resolution, I investigated the response of particles to an environment change of the entire surrounding. Chapter 3 shows how single nanoparticles can be used for local pH-sensing. The nanoparticle pH-sensor has the advantage over dyes commonly used for this purpose to provide a long term stable signal as they neither blink nor bleach. I present the accomplishment of the necessary functionalization with a pH responsive polymer and show data verifying the respective response. As each of these pH-sensors reacts only to the volume directly surrounding it, the possibility to map pH-distributions e.g. within a single cell is given. Even though this is an interesting study the limitation in sensitivity and time resolution manifested motivated me to construct a setup with improved time resolution and sensitivity features.

The Plasmon Fluctuation Setup combines the advantages of a much stronger light source and a more sensitive detector (Chapter 4). With this an improvement in temporal resolution of 4-6 magnitudes compared to earlier setups is realized. Furthermore, its performance concerning spectral resolution as well as stability is enhanced as I also show in this chapter. With this setup I investigated three systems: single nanorods as molecular sensor, dimers as plasmon ruler, and single nanorods as sensors for diffusers.

Chapter 5 shows the detection of individual unlabeled proteins. Such an enhanced sensitivity allows to investigate the molecule binding without the need for labels which possibly alter the conformation or characteristic behavior of the analyte. I include additional experiments confirming the hypothesis of having single molecule events. Furthermore, I provide a proof of principle experiment that analyzes for fluctuations as a new and powerful tool to investigate binding kinetics. Such equilibrium fluctuations can only be observed for sensors limited in their reactive surface to a few tenth of molecules as the fluctuation is otherwise hidden by the number of parallel events.

The usability of the nanoruler recently introduced for nanoscale distance and orientation sensing applications is investigated in Chapter 6. Here, assemblies of two spherical nanoparticles connected by a spacer molecule, called dimer or nanoruler, are studied under intense illumination. I found out that this strong illumination with visible light induces the particles to approach each other, eventually resulting in complete collapse of the space between them. Therefore, their convenience for distance sensing application in improved setups is questionable but they might serve other demands like nanoshutters or positioners.

In addition to the study on dimers under strong illumination, I approached the possibility of using these dimers to determine the stiffness of the spacer molecule by investigation of distance fluctuations. This study can be found in Chapter 7 where I provide a number of experiments to learn about this method. Astonishingly, a mysterious slow distance fluctuation was discovered which could not be significantly influenced due to environment changes and was not matching the value predicted by theory.

Plasmon correlation spectroscopy, a method related to fluorescence correlation spectroscopy, is explained in Chapter 8. Here, the sensing volume of a plasmonic nanoparticle is used to sense unlabeled diffusers. The advantage of plasmon correlation spectroscopy over common methods is the increase in accessible concentrations to values as found in biological systems. Despite profound theoretical investigations finding reasonable sensor dimensions this study was not yet completed to experimental difficulties.

Finally, the thesis is summarized in Chapter 9 followed by a short Appendix including information about particle synthesis (A) and functionalization (B). Also technical devices and mathematical concepts used in this thesis are described (C).

2 Plasmons in a Nutshell

Noble metal nanoparticles show bright colors under illumination. This optical phenomenon is owed to the combination of two major factors: the free electron cloud present in metallic materials and particle sizes smaller than the penetration depth of light. The generated, so-called, particle or localized surface plasmon can be investigated in suspensions as well as at single particle level. Throughout this work I will refer to localized surface plasmons simply as 'plasmons'[1].

In the following chapter I give a brief summary of the theory of plasmons relevant to this thesis. First, in Section 2.1 I introduce the features of extinction and scattering spectra for the two cases of ensemble and single particle measurement as the understanding of these spectra is essential. To get a picture of the plasmon process a theoretical explanation is then given, using the theory of Drude and Sommerfeld. Several models used in this thesis to mathematically predict plasmonic spectra are also presented. Therefore, I introduce the quasi-static approximation model (QSA) followed by extending the computational models to arbitrary shaped particles. Thus, the boundary element method (BEM) is presented for more complex implementations. As plasmonic nanoparticle spectra are influenced by the particle's environment they can be exploited for sensing applications. This principle, central to the work I present in this thesis, is briefly introduced in Section 2.2. Another interesting attribute of plasmonic nanoparticles is their strong plasmonic interaction if placed in close proximity. The importance and characteristics of such optically coupled nanoparticles is discussed in Section 2.3. As this work is carried out under high illumination powers, the aspect of heating has to be considered. Information on nanoparticle heating due to absorption of illumination light can be found in Section 2.4. Also related to the special illumination is the occurrence of an evanescent wave created via total internal reflection at the sample interface. The necessary theoretical background is given in Section 2.5. Finally, information about optical forces can be found in Section 2.6. This is provided as optical forces are assumed as one mechanism for an effect later discussed within this work.

As the entire field of plasmonics is broad and can only be briefly introduced here, I would like to refer the interested reader additionally to very good reviews on the field of plasmonics that have been published recently [11, 12, 13].

2.1 Plasmon spectra

Looking at a nanoparticle suspension by eye under different illumination angles reveals a characteristic color change. This effect is due to two different types of light-particle interactions: absorption and scattering. In front of a dark background only the scattered light is visible. In front of a bright background extinction becomes visible (see Figure 2.1a and b). Extinction appears when light

---

[1] There are also surface plasmon polaritons which are electromagnetic waves propagating at an extended 2D interface between a plasmonic metal and a dielectric [1].

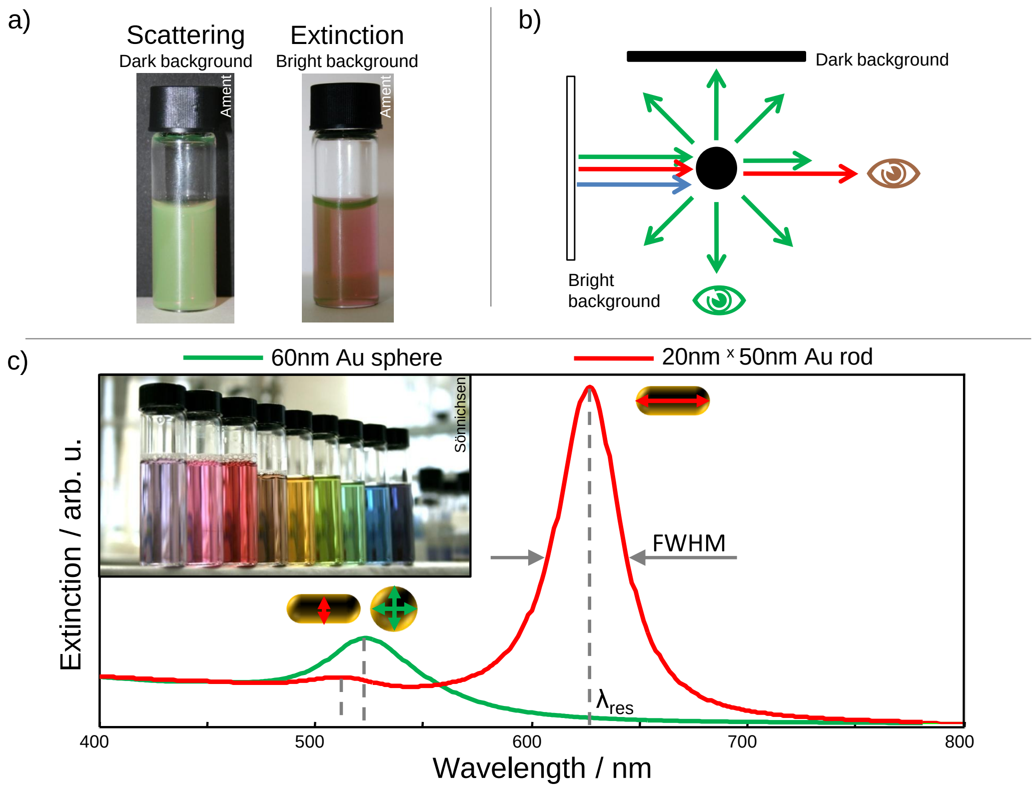

Figure 2.1: a) Photograph of the same solution of nanoparticles in front of a dark and a bright background. In front of a dark background only the scattered component can be observed, whereas in front of a bright background the color arises from the absence of the scattered in the transmitted light. b) Sketch of the different processes and the occurring colors. c) The curves show the extinction spectra of a 60 nm Au sphere (green) and a 20 nm × 50 nm Au rod (red). For the sphere only one resonance peak is present. For the rod there are two peaks presenting the short and the long axis. The inset shows a variation of possible colors arising from samples of different shape, size and material.

transmitting a sample is not only altered due to absorption but the sample also scatters part of the light away from the incident direction of the beam. In general, spectra can be acquired from single particles or ensembles. First, a glance at typical single particle extinction curves: in Figure 2.1c the spectra of a gold sphere and a gold rod are shown, respectively. The run of these spectra shows peaks for which I first want to introduce two definitions: The wavelength of the maximum of a peak is called resonance wavelength, λ_{res}. The width of a peak is characterized by the full width at half maximum, $FWHM$. For a sphere only one distinct resonance peak is present. In the case of a rod, two peaks appear, one at longer wavelengths and one at about the sphere resonance wavelength. These peaks belong to the long and the short axis of the particle, respectively. What is remarkable is that the resonance position of the longitudinal peak is dependent on the aspect ratio of the particle. Furthermore, we get from the single particle spectrum insight into the damping of the system as it is directly connected to the $FWHM$ of the corresponding peak.

However, acquiring such a single particle extinction curve is difficult due to the strong background. Thus, more commonly the ensemble spectrum is measured. Therefore, a particle suspension is analyzed by measuring the transmitted light. In this case the detected light is manipulated by all particles present in solution, resulting in a different meaning of the *FWHM*. Here, resonance peaks from all particles present will superimpose, leading to a broadening of the curve as the particles are not monodisperse, but slightly differ in size and shape.
The investigation of the plasmon at a single particle level can be accomplished via the single particle scattering spectrum. In a microscope, such a scattering spectrum can be obtained by illuminating the particle either with dark field or total internal reflection illumination. In both cases, no direct illumination light will be gathered by the microscope objective. The sample picture consists therefore only of bright diffraction limited spots on a dark background (see Figure 4.6). A nice analogy is the presence of stars during the day, but only being visible in the absence of the strong background of our sun, namely at night. This kind of spectrum is the spectrum mainly acquired in this thesis.

After giving some general information about plasmonic spectra and the methods to measure them, I discuss the theoretical background of plasmons in the next paragraph.

2.1.1 Drude-Sommerfeld model

A number of physical properties of metals can be well explained qualitatively and quantitatively by the model of the free electron gas. Drude was the first one who transferred the kinetic gas theory to metals, assuming electrons to be point like and non-interacting, except for direct collisions with total loss of directional information. A quarter decade later, after the introduction of quantum mechanics, Sommerfeld applied the Pauli exclusion principle to the speed distribution of electrons [14].
Interaction of an oscillating external force, an electromagnetic wave, with this free electron gas will lead to oscillation of the electron cloud with respect to the fixed positive nucleus of the atoms. The resulting movement of the electrons can be treated as a damped harmonic oscillator. Using these assumptions and solving the dynamic equation will give the dielectric function:

$$\epsilon(\omega) \quad = \quad 1 - \frac{\omega_p^2}{\omega(\omega + i\gamma_0)} \tag{2.1}$$

The plasma frequency is denoted $\omega_p = \sqrt{\frac{ne^2}{\epsilon_0 m^*}}$ with n as density of free electrons and m^* as their effective mass[2]. Fitting Equation 2.1 to values obtained from bulk experiments measured on nanometer thick layers by Johnson and Christy [15] introduces the parameter ϵ_∞ [16].

---

[2] The band structure of the electron orbitals is the origin of the effective mass. The effective mass can take different values depending on the position of the electron within the band.

$$\epsilon(\omega) = \epsilon_\infty - \frac{\omega_p^2}{\omega(\omega + i\gamma_0)} \approx \epsilon_\infty - \frac{\omega_p^2}{\omega^2} + i\frac{\gamma_0\omega_p^2}{\omega^3} \tag{2.2}$$

The approximation on the right hand side of Equation 2.2 is valid for $\omega \gg \gamma_0$ which holds down to near-infrared frequencies for materials used here.

This frequency dependent dielectric function $\epsilon(\omega) = \epsilon' + i\epsilon''$ describes most of the optical properties exhibited by plasmonic particles of the material rather than the complex index of refraction $\tilde{n} = n + ik$ (for conversion $\epsilon = \tilde{n}^2$, $\epsilon' = n^2 - k^2$, and $\epsilon'' = 2nk$) [17]. Side remark: Additional factors which influence the exact resonance position of a particle are the atomic surface roughness, the end-cap geometry and the amount of particle charging [18, 19, 20, 21]. The real part of ϵ gives insight into the amount of polarization of the material whereas the imaginary part holds information about the dissipated energy. Kramers-Kronig relation describes the conversion of the real and imaginary part into each other [22]. The quantitative relation between dielectric function and scattered or absorbed spectrum for particles much smaller than the wavelength of the incident light is discussed in Section 2.1.2. Prior to this, I give a brief overview on the damping mechanism relevant for electrons moving in metal nanoparticles.

Damping mechanism

The theoretical results stated above, show good agreement for particles bigger than 10 nm. In the case of smaller particles the dielectric function differs from the values of the bulk material and starts to be size dependent. The explanation is the mean free path[3] of an electron exceeding the particle dimension itself, leading to a *surface-scattering effect* which is inversely proportional to the particle's dimension [23].

If the photon frequency enters the material dependent regime of *interband transitions,* discrepancies to Equation 2.2 appear. In this regime, ϵ is influenced by optically excited transitions of electrons from the d-band into the conduction band. This takes place at an energy of ∼1.7 eV (∼730 nm) for gold and ∼2.4 eV (∼517 nm) for silver [24]. Thus, measured and predicted imaginary parts of the dielectric function show discrepancies for shorter wavelengths.

Furthermore, the electron oscillation can be disturbed due to scattering events of electrons with e.g. impurities or phonons that lead to a dephasing. For more detailed information on damping mechanisms in general I can refer the reader to Hu et al. [25].

---

[3] This mean free path is related to the relaxation constant (also called bulk damping constant) γ_0 in Equation 2.2.

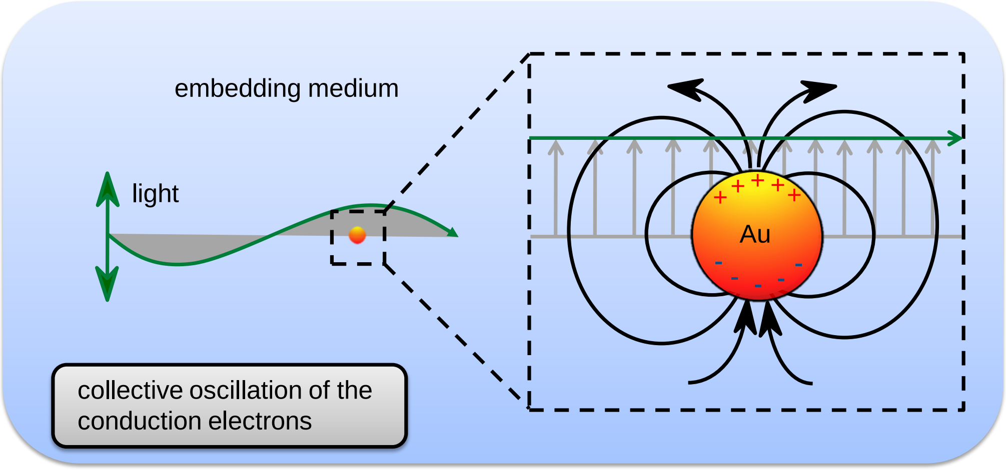

Figure 2.2: A noble metal nanoparticle penetrated by an electromagnetic field. As the particle's dimensions are much smaller than the wavelength of the light it can be assumed that every point within the particle feels the same phase. This is the assumption of the quasi-static approximation.

2.1.2 Quasi-static approximation

In the quasi-static approximation (QSA) particle sizes much smaller than the wavelength of the illuminating light ($r << \lambda$) are considered. Each point of the particle feels the same phase of the light wave (see Figure 2.2) and electrostatic calculations can be carried out using the boundary conditions of a spheroidal particle surface [23]. No excitation due to the magnetic field occurs within QSA. The scattering and absorption cross sections calculate as follows:

$$C_{\text{scat}} = \frac{k^4}{6\pi\epsilon_0^2} \mid \alpha \mid^2, \quad C_{\text{abs}} = \frac{k}{\epsilon_0} Im(\alpha), \quad I_{\text{scat, abs}} = \frac{I_0(\omega)}{A} C_{\text{scat, abs}} \tag{2.3}$$

$C_{\text{scat, abs}}$: scattering / absorption cross section

$k = 2\pi\sqrt{\epsilon_{\text{m}}}/\lambda$: wave vector

ϵ_{m}: dielectric constant of the embedding medium[4]

λ: wavelength of the light in vacuum

$\epsilon_0 = 8.854 \cdot 10^{-12} \frac{\text{A s}}{\text{V m}}$: vacuum permittivity

α: polarizability of the particle

$I_0(\omega)/A$: light intensity per area

---

[4] Within this thesis the dielectric function of glass and water is approximated to a constant value.

Interestingly, also Rayleigh's law $C_{\mathsf{scat}} \propto 1/\lambda^4$ can be found in Equation 2.3 if we assume only a weak wavelength dependence of α.
The polarizability α can be deduced from the electric displacement field $D = \epsilon_0 E + P$ with the electric field E and the polarization density $P = N\alpha\vec{E}_{\mathsf{local}}$ (N number of dipoles per volume; $N = 1/V$ in the case of a single particle). Here, the local electric field $\vec{E}_{\text{local}}$ seen by an atom is the sum of the external field $\vec{E}_{\mathsf{ext}}$ and the electrical field $\vec{E}_{\mathsf{N}}$ caused by neighboring atoms. With $\vec{E}_{\mathsf{N}} = \frac{\vec{P}}{3\epsilon_0}$ it leads to:

$$\alpha = 3\epsilon_0 V \frac{\epsilon_{\mathsf{p}} - \epsilon_{\mathsf{m}}}{\epsilon_{\mathsf{p}} + 2\epsilon_{\mathsf{m}}} \qquad \text{(Clausius Mossotti relation)} \tag{2.4}$$

ϵ_{p}: dielectric function of the metal nanoparticle
ϵ_{m}: dielectric constant of the surrounding medium at optical frequencies

From Equation 2.4 the presence of a pole at

$$\epsilon_{\mathsf{p}} = -2\epsilon_{\mathsf{m}} \tag{2.5}$$

can be seen. This condition can be fulfilled by noble metals and is the source of the existence of a resonance position. Noticeably, the direct influence of the embedding medium on the resonance position makes plasmonic nanoparticles perfect candidates for environmental sensors.

QSA for spheroids

As particles under investigation are often of spheroidal shape, it is necessary to extend the polarizability, α, to be able to calculate the plasmon spectra of these particles, too. In 1912, the first analysis of a plasmon spectrum for an ellipsoid was made by Richard Gans. For ellipsoids of sizes much smaller than the wavelength of the illuminating light he predicted the split of the plasmon resonance into two peaks. He analytically calculated the polarizability of an ellipsoid as a function of particle dependence to be [26]:

$$\alpha_{\mathsf{x,\,y,\,z}} = \frac{V(\epsilon_{\mathsf{p}} - \epsilon_{\mathsf{m}})}{\epsilon_{\mathsf{m}} + L_{\mathsf{x,\,y,\,z}}(\epsilon_{\mathsf{p}} - \epsilon_{\mathsf{m}})}, \quad V = 4\pi abc/3 \tag{2.6}$$

Here $L_{\text{x, y, z}}$ is a geometry factor for the respective axis given by:

$$L_{\mathsf{x}} = \frac{1-e^2}{e^2}\left(-1 + \frac{1}{2e}\ln\frac{1+e}{1-e}\right), \quad L_{\mathsf{y,\,z}} = \frac{1-L_{\mathsf{x}}}{2}, \quad e^2 = 1 - \left(\frac{b}{a}\right)^2 \tag{2.7}$$

The described ellipsoid has the diameters a, b, and c with $a \geq b = c$. In the case of a sphere, the eccentricity, e, is zero and the geometry factor, L, is 1/3. Similarly, for a ellipsoid with the dimensions $a = b \geq c$ a geometry factor can be defined.

QSA for functionalized particles

Very often, nanoparticles are surrounded by a material with a different refractive index. In this work this is introduced by functionalization of the nanoparticles with a biomolecule or simple adsorption. To accurately simulate this situation a slight variation of the polarizability has to be considered. Liu and Guyot-Sionnest approximated the polarizability of spheroids with a shell under the conditions $a_{\mathsf{p,\ s}} \geq b_{\mathsf{p,\ s}} = c_{\mathsf{p,\ s}}$ to be [27]:

$$\alpha_{\mathsf{i}} = V_{\mathsf{all}} \frac{\{(\epsilon_{\mathsf{s}} - \epsilon_{\mathsf{m}})[\epsilon_{\mathsf{s}} + (\epsilon_{\mathsf{p}} - \epsilon_{\mathsf{s}})(L_{\mathsf{i}}^{(\mathsf{p})} - fL_{\mathsf{i}}^{(\mathsf{s})})] + f\epsilon_{\mathsf{s}}(\epsilon_{\mathsf{p}} - \epsilon_{\mathsf{s}})\}}{[\epsilon_{\mathsf{s}} + (\epsilon_{\mathsf{p}} - \epsilon_{\mathsf{s}})(L_{\mathsf{i}}^{(\mathsf{p})} - fL_{\mathsf{i}}^{(\mathsf{s})})][\epsilon_{\mathsf{m}} + (\epsilon_{\mathsf{s}} - \epsilon_{\mathsf{m}})L_{\mathsf{i}}^{(\mathsf{s})}] + fL_{\mathsf{i}}^{(\mathsf{s})}\epsilon_{\mathsf{s}}(\epsilon_{\mathsf{p}} - \epsilon_{\mathsf{s}})} \tag{2.8}$$

$V_{\mathsf{all}} = 4\pi a_{\mathsf{s}} b_{\mathsf{s}} c_{\mathsf{s}}/3$: volume of the coated particle
$f = a_{\mathsf{p}} b_{\mathsf{p}} c_{\mathsf{p}}/a_{\mathsf{s}} b_{\mathsf{s}} c_{\mathsf{s}}$: volume fraction of metal particle from covered particle
ϵ_{p}: dielectric function of the core nanoparticle
ϵ_{s}: dielectric function of the shell medium
ϵ_{m}: dielectric constant of the surrounding medium
$\mathrm{i} = 1,\ 2,\ 3$
$L_{1,2}^{(\mathsf{k})} = (1 - L_3^{(\mathsf{k})})/2, \quad L_3^{(\mathsf{k})} = \frac{1-e_{\mathsf{k}}^2}{e_{\mathsf{k}}^2}(-1 + \frac{1}{2e_{\mathsf{k}}} \ln \frac{1+e_{\mathsf{k}}}{1-e_{\mathsf{k}}})$: geometrical factors
$e_{\mathsf{k}}^2 = 1 - \frac{c_{\mathsf{k}}^2}{a_{\mathsf{k}}^2}$ (k=p, s): eccentricity

In the case of a biomolecular shell the dielectric function ϵ_{s} simplifies to $\epsilon_{\mathsf{s}} = n^2 = 2.25$ which is in first approximation true for all biomolecules [28]. More accurate estimations, for the case when single molecules adsorb, can only be carried out with numerical methods. In this thesis the boundary element method (see Section 2.1.3) is used.

Limits of QSA

As already mentioned in Section 2.1.1 there are limits for particle sizes smaller than the mean free path of the electrons in bulk material. For very small particles quantum mechanical effects have to be considered as the number of electrons is limited.

If the nanoparticle dimension exceeds the regime valid for QSA, meaning not all spots of the particle feel the same phase anymore, Equation 2.3 no longer holds true. For these large particles the plasmon spectra have to include higher multipole terms. Furthermore, for large particles the penetration depth of light has to be taken into account.

2.1.3 Numerical methods for arbitrary shaped nanoparticles

With the equations introduced so far the response of spherical or spheroidal particles to an incident electromagnetic field can be calculated with high accuracy within the given restriction of size. To gain information about the spectra of plasmonic nanoparticles in the presence of an additional close by particle or molecule numerical solutions have to be considered. First, I want to give a short overview over the major methods and then describe briefly the boundary element method (BEM) as simulations for complex systems in this thesis are based on this method.

To this date, several different methods have been suggested to calculate the plasmon spectra of nanoparticles within more complex configurations in the incidence of illumination. Purcell and Pennypacker [29] introduced the **discrete dipole approximation (DDA)** in 1973 to calculate light interaction with dust particles in space. As the name suggests, this method divides the arbitrary shaped nanoparticle into N polarizable elements to approximate cross-sections of extinction, absorption, and scattering. For each element the Clausius-Mossotti relation (Equation 2.4) with the corresponding volume V is considered and the differential equations, describing the interaction of a dipole with the others and the external field, are solved [30].
In the last decade further approaches like the **finite difference in the time domain method (FDTD)**, based on the propagation of the electromagnetic field defined on a spatial grid through consecutive time steps, became popular [31].

Boundary element method (BEM)

The numerical approach applied within this thesis is the boundary element method (BEM). Within BEM the particle surface gets discretized into small triangles for which appropriate boundary conditions are imposed by the continuity condition of the parallel components of the electric and magnetic fields. The system of surface-integral equations obtained in this manner is transformed into a set of linear equations and then solved with established mathematical methods.
The BEM software used in this work was written by [32] and from the University of Graz (Austria). The present version (MNPBEM-Version 11) allows calculating particles of manifold shapes. Furthermore, implementations for coated particles, coupled particles, coupled particles of different materials and particles on a surface are possible. All this is kindly provided to our group in a Matlab-toolbox.

2.2 Plasmon sensors

It is well known that noble metal nanoparticles are good sensors for refractive index changes in their direct environment [33]. This can be understood by imagining the electromagnetic field lines penetrating the outer medium (see Figure

2.2). Mathematically this can be derived from the dependence of the resonance position on ϵ_{m} (Equation 2.5). Keeping all other parameters constant besides the environment, allows the use of the resonance position as indicator for changes in the local environment. These changes can either be a solvent exchange [34], or, more interestingly, the binding of small particles or molecules to our sensor [35]. In the case of dense layer coverage this leads to the relation [36]:

$$\Delta\lambda_{\mathsf{max}} = S_\lambda \Delta n_{\mathsf{ads}}[1 - \exp(-2d/l_d)] \tag{2.9}$$

Here, S_λ is the bulk refractive-index sensitivity of the nanoparticle, Δn_{ads} is the change in refractive index induced by the adsorbate, the size of the adsorbate is incorporated by d, whereas l_d is the sensing distance of the nanoparticle[5]. An increase in the refractive index of the surrounding medium is therefore reflected in a red shift of the resonance wavelength.

Optimized choice of the Sensor

To achieve the maximum wavelength shift, especially necessary if the volume of adsorbing analyte is small, the sensing particle has to be optimized in shape, size and material. To improve the sensitivity, S_λ, defined as wavelength change per refractive index change, $\Delta\lambda/\Delta n$, the particle shape can be optimized. A spherical particle has a much weaker sensitivity than a rod shaped particle. Furthermore, rods with a high aspect ratio outperform low aspect ratio rods. Mathematically this can be seen from Equations 2.3, 2.6 and 2.7. Nanoparticles with sharp tips further improve the sensitivity due to the generation of hot spots [38]. Nevertheless, in this case the very limited adsorption area in the hot spot is disadvantageous. Of course also rod shaped particles show a field enhancement and the connected sensitivity dependence from the attachment position on the rod (see Table 5.1 and Figure 5.8). However, in the case of rods this effect is still acceptable. Thus, normally the selected shape for this thesis is a rod.

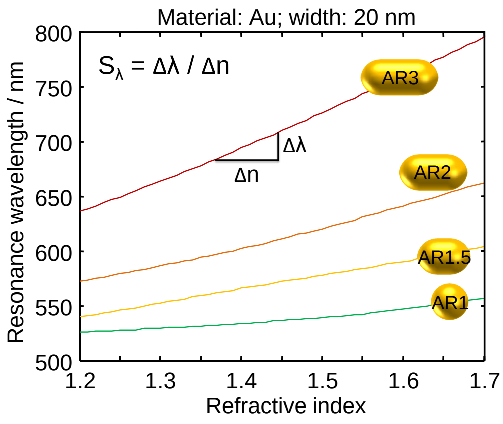

Figure 2.3: QSA simulation for gold particles in different refractive indices. The width simulated for all particles is 20 nm.

Additionally, a metal with a strong wavelength dependence of the real part of the

---

[5] The factor two in the exponential appears due to normalization reasons. For further details see [37].

dielectric function would be advantageous. Limitations of the Plasmon Fluctuation Setup (see Chapter 4) cut the possible resonance wavelength down to be between 500 nm and 700 nm. This rules all metals out except gold, silver[6] and potassium which have a comparable $\epsilon(\lambda)$ dependence [39]. Potassium is not further taken into account as its reactivity makes it too dangerous. The chemical stability of gold is much better compared to silver. Thus, even though the imaginary part of silver is smaller, and therefore the plasmon peak is sharper, the metal of choice in this thesis is gold.

Specific biorecognition

To achieve a specific binding of the analyte onto the sensor a matching receptor has to be introduced. Coating the nanoparticle initially with this receptor will trade off the specificity with a decrease in sensitivity as the most sensitive region is directly around the particle (Equation 2.9) [40]. It must also be noted that a high surface binding efficiency as well as a large mass density of the biomolecule are requirements for inducing a large resonance shift [37].

2.3 Coupled nanoparticles

In the last few years, the field of nanoscience has also evolved into investigation of well defined nanostructures made out of a small number of nanoparticles. This interest is due to the change in resonance frequency when the nanoparticles are brought into proximity. At a first glance this is easy to understand as the embedding media influences the resonance position as discussed in Section 2.1.2 and 2.2. In the case of two approaching nanoparticles the field lines overlap, leading to a coupling of the plasmon.

In the case of nanoparticles in proximity to each other the electric field seen by a single particle will be altered due to the near-field of the other particles. Therefore, the electric field is the sum of the incident light field and the near-field of surrounding particles: $E = E_0 + E_{\mathsf{nf}}$. This leads to a change in resonance frequency called plasmon coupling. Furthermore, the electric near-field in the interparticle gap is strongly enhanced up to several magnitudes and a hot spot is created [41].

Large aggregates

For the first time in 1996 Mirkin and coworkers used plasmon coupling for sensing purposes [42]. DNA functionalized nanospheres were incubated with counter DNA strands, leading to an hybridization induced assembly of the particles. As this

---

[6] Silver spheres have a resonance below the stated regime. Only differently shaped particles like rods or triangles can be investigated with the Plasmon Fluctuation Setup.

assembly is accompanied by a strong red shift of the resonance position, this constitutes a sequence-specific sensor for trace amounts of DNA strands. In the presence of higher amounts of DNA, nanoparticles form huge clusters, settling on the bottom of the vial and the solution turns colorless. Since then, even more universal sensing methods were developed using conjugation polymers and single stranded DNA to inhibit or trigger the aggregation of gold nanoparticles in the presence of a broad range of targets [43].

2.3.1 Dimers of spheres

The simplest system of coupled nanoparticles consists of two identical spheres. Here, a polarization dependent splitting of the resonance wavelength into two resonances occurs. The resonance position obtained with light polarized parallel to the interparticle axis is strongly red shifted. The smaller the gap between the particles the bigger the red shift. In contrast we find a very weak blue shift compared to the individual particle when illuminated with light polarized perpendicular to the interparticle axis (see Figure 2.4). Several models try to explain and predict the coupled resonance wavelength qualitatively as well as quantitatively.

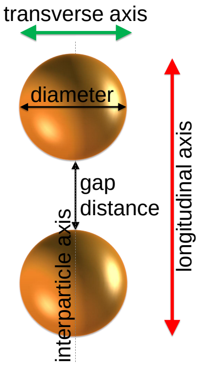

Figure 2.4: Parameters used for dimer description

In 2003, scientists approached their experimental results of the interparticle coupling with theoretical explanations: Rechberger et al. visualized the coupling effect of the induced particle dipoles with springs [44]. Whereas the approximately exponential shift decay with increasing particle spacing made Su et al. suggest a mechanism already known from quantum mechanics, namely photon tunneling [45]. Despite the nice picturing of the situation, no clear mathematical description of the dependence of the shift on the separation distance is given in their publications.

Such a mathematical description can be found in two further models which I will briefly present: The hybridization model and the excition-coupling model. Both have in common that they describe the separation dependent coupling quite well for larger separation distances. However, they are still lacking the case of nearly touching particles. Further theories accounting this situation separately are discussed later in this chapter.

Hybridization model [46, 47]

In the hybridization model the electrons of the conduction band are simulated as an incompressible, charged liquid. The positively charged nucleus is uniformly distributed inside the particles boundaries and fixed in space. In the absence of an electromagnetic field the electron liquid, too, is homogeneously distributed in the particle, thus no dipole moment is formed. If light falls onto the system, the

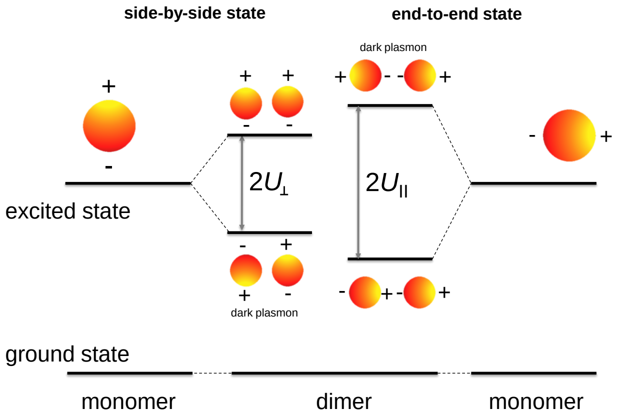

Figure 2.5: Hybridization model for sphere dimers. In the case of illumination perpendicular to the interparticle axis the side-by-side state is realized, for parallel illumination the end-to-end state. Only the symmetric modes are bright. The asymmetric modes are dark. The value for the splitting energy *U* is larger for parallel illumination.

electron liquid is forced out of the equilibrium position and charge separation takes place (see Figure 2.5). The dynamics of the plasmon oscillation can be modeled with Coulomb interaction, keeping in mind the essential condition of the system size being much smaller than the illumination wavelength.
This model gives a detailed understanding of the energies and the extinction cross sections of dimers. However the model lacks the description of higher multipole interactions which have to be considered if particles are in close proximity.

Exciton-coupling model [24]

In the exciton-coupling model the effects seen for nanoparticle coupling are related to the very similar behavior of chromophore dimerization. Assuming that every particle is a point like dipole leads to an interaction approximated by Coulomb's law:

$$E = E_0 + \frac{\xi\mu}{4\pi\epsilon_0 g^3}, \quad \xi = 3\cos\theta_1\cos\theta_2 - \cos\theta_{12} \tag{2.10}$$

E: electric field of a coupled particle
E_0: electric field of a single particle
ξ: orientation factor
μ: dipole moment of the monomers
g: distance between the dipoles
θ_1: angle between dipole 1 and interdipole axis
θ_2: angle between dipole 2 and interdipole axis
θ_{12}: angle between dipoles

with the interaction energy:

$$U = -\frac{\xi \mid \mu \mid^2}{4\pi\epsilon_0 g^3} \tag{2.11}$$

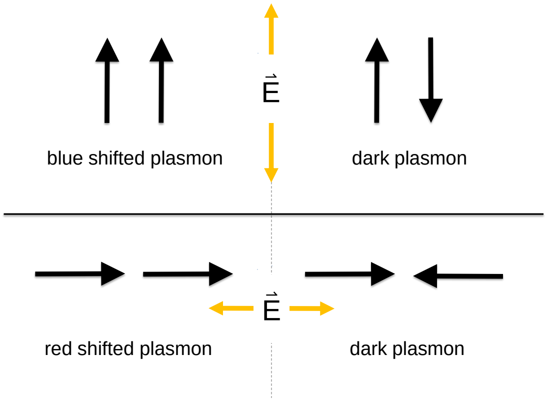

Figure 2.6: Symmetric and antisymmetric configurations of dipole arrangements are shown. In the upper part of the figure the particle dimer is illuminated with light polarized perpendicular to the interparticle symmetry axis. The coupled particle has a blue shifted resonance. In the lower part of the figure the illumination light is polarized parallel to the interparticle axis. Here, the resulting plasmon resonance is red shifted. As no light is emitted in the antisymmetric modes they are called dark plasmons.

As the orientation of the dipoles is predetermined by the polarization of the incident light, only symmetric or antisymmetric configurations are imaginable (see Figure 2.6). However, the antisymmetric ones are not possible as the dipoles are oriented oppositely and are of equal size. Thus, they are called 'dark plasmons'[7]. For illumination parallel to the interparticle axis we obtain the values $\xi = 2$ and $U < 0$. Negative interaction energy implies an attractive interaction leading to a red shift of the resonance wavelength. For illumination perpendicular to the interparticle axis $\xi = -1$ and $U > 0$. This implies a repulsive interaction and therefore a blue shift. This shift is smaller than in the parallel case as the interaction energy is twofold smaller.

In the hybridization model as well as the exciton-coupling model, experimentally measured shifts can be qualitatively and quantitatively well explained if particle separation is larger than approximately 0.2 times the particle diameter. The exciton-coupling model has additionally the advantage to describe the coupling of nanorods, whereas, the hybridization model cannot provide this information. Furthermore, the author of the exciton-coupling model has been able to find a universal scaling law which describes the dependence of the resonance shift on the gap distance for differently sized nanoparticles. I present this universal scaling law in the next paragraph.

2.3.2 Distance sensing with dimers

Several authors have shown an exponential distance dependence of the resonance wavelength on interparticle gap distance [45, 49, 50]. In 2007, Jain et al. were able to derive a universal scaling law covering differently sized nanoparticles. They

---

[7] Yang et al. managed to study dark plasmon modes within octahedral gold nanocrystal dimers by using a TIR setup [48].

introduced a normalization of the wavelength shift with the resonance wavelength of the individual particle, $\Delta\lambda/\lambda_0$, as well as a normalization of the gap distance with the particle size, g/D. With this parametrization a consensus of the measured data points for different particle sizes can be found.

$$\frac{\Delta\lambda}{\lambda_0} \approx k \cdot e^{-g/0.2D} \tag{2.12}$$

$\Delta\lambda$: resonance shift compared to individual particle
λ_0 : resonance position of individual particle
g: gap distance
D: particle diameter
k: scaling factor for maximum plasmon shift; condition dependent

This universal scaling behavior of the distance decay of plasmon coupling in metal nanoparticles is exponential. Keeping in mind that the near-field decay is inversely proportional to the third power of the distance [46, 51] a nearly exponential decay is a good approximation [50]. Furthermore, Jain et al. investigated systems with different metal types, shapes and surrounding media by simulation and compared published experimental data with the finding that Equation 2.12 is valid for all of these cases [50]. The decay length, also refereed to as near-field coupling depth, is always ~0.2 times the diameter [24]. The scaling factor k can vary slightly depending on the surrounding medium and the type of metal. This is reasonable as it predetermines the maximum coupling strength which is dependent on factors like the surrounding medium or the metal type. As an example, electromagnetic fields in silver are much more intense compared to gold where the interband damping already occurs. Furthermore, it needs to be mentioned that this scaling law is only accounting for dipole interactions and is proven to be valid for gap distances bigger than $0.1\,D$. The true distance dependence accounting for multipoles has to be done numerically and should produce a steeper curve. Especially for nearly touching particles, as discussed in the next paragraph, the multipole approach has to be considered.

Nearly touching particles

For gap distances smaller than ~0.2 times the particle dimer the resonance position is further in the red compared to the earlier presented universal scaling law from Jain et al. [52]. This red shift is expected by including multipole interactions in the scaling behavior of nanoparticles [46]. Additionally, further studies of nanodimers near the conductive contact limit emphasizes the appearance of supplementary peaks which are assigned to the hybridization of the main dipole mode with a higher-order multipole mode [53, 54]. E.g. the rise of a quadrupole resonance is assumed at gap distances approximately 0.06 times smaller than the particle radius.

The numerical handling of nearly touching dimers becomes a serious challenge as the smallest size in a system determines the amount of calculations needed to simulate accurately. Madoyan et al. have developed a new method to quickly determine the resonance position of coupled nanospheres in close proximity [55]. The idea of the method is the reduction of the wave equation to the Laplace equation with corresponding boundary conditions. This leads to a shortening of computational time with a higher accuracy due to rapid convergence of the iteration procedure. Additionally, they proved their semi-analytical method to be in good agreement in the regime of a gap distance bigger than particle radius.

Touching particles

The situation alters again if going from nearly touching particles to actual contact. As soon as a conductive bridge between the particles is established, the resonance wavelength blue shifts again [53]. Romero et al. explain this blue shift with the release of before piled up charges at the interparticle gap. The charge can now oscillate through the entire connected dimer. As before for nearly touching particles near the contact point, additional multipole peaks are present in the spectrum. For a particle not having the form of a dumbbell but rather one of a rod these multipole peaks vanish.

Heterodimers, hollow dimers, giant dimers and nanonecklaces

The coupling of nanospheres of different size or material are examined in literature and reveal interesting otherwise hidden effects. Coupling two particles of different size will exhibit the otherwise dark plasmon mode as a weak bright plasmon. This is due to the differently sized dipole moments which cannot cancel each other out. This effect was experimentally proven by Sheikholeslami et al. and is consistent with the plasmon hybridization model [56]. Nevertheless, in comparison to the symmetric mode, the antisymmetric mode is much weaker in intensity. In general, the exciton-coupling model also explains the measured resonances well. However, it is only valid for system dimensions much smaller than the wavelength of incident light. Otherwise the particles feel different phases of the electromagnetic field and, as in QSA (see Section 2.1.2), retardation effects have to be considered [57].

Further studies on the spectrum changes of heterodimers were carried out by Brown et al. [58]. They find that the dipole of the smaller particle can couple double efficiently to both the dipole and higher multipoles of the larger nanoparticle introducing additional peaks in the plasmon spectrum. Furthermore, heterodimer spectra are also strongly sensitive to the interparticle distance. In a heterosystem, destructive interference of in phase and out of phase oscillations, bright and dark plasmons, might even lead to Fano resonances as they were described by Mirin et al. for septamers [59].

Similar studies about the scattering spectrum of other unusual shapes like hollow sphere dimers, large nanoparticle dimers or even nanonecklaces are also present in literature [51, 60, 61, 62].

Dimers of nanorods

Theoretical investigation of a dimeric rod system with side-by-side and tip-to-tip configuration was started in 2003 [63]. Six years later, the experimental studies followed also including a variable interparticle angle. Tabor et al. prepared rod shaped gold nanoparticles which were synthesized by lithographic methods [64]. They found a slightly altered interaction equation which has approximately a $\cos^2\theta$ dependence. Here, one nanorod is fixed with its long axis on the interparticle axis. θ describes the rotation of the second nanorod to this angle. Further measurements on coupled gold nanorods at variable distances and in different geometries were carried out in the Mulvaney laboratory [65] with the elucidation of new hybridization interactions which are introduced by different interaction geometries. A detailed mathematical analysis of the coupling phenomenon based on dipole-dipole interactions, also providing equations for the scattering cross sections of interacting rods, can be found in the publication of Shao et al. [66].

2.3.3 Conclusion

In the last decade scientists have noticed the high potential of coupled nanoparticles for sensing applications. The distance and orientation dependence of coupled nanoparticles can be exploited for this purpose. However, to reach this goal models with reliable predictions for the experimentally measured spectral characteristics of coupled systems are required. Today, the most popular theory, applicable for medium distances, is the exciton-coupling model. The author of this model also introduced the universal scaling law, practicable for dimer systems of different materials, shapes and environments. In the more difficult case of nearly touching dimers qualitative descriptions are available today. This knowledge I will use in Chapter 6 to calibrate and analyze my dimer system.

Besides optical nanoparticle coupling the nanoparticle heating due to light absorption is also an important effect for this thesis. Thus, I will give a brief introduction into this subject within the next section.

2.4 Nanoparticle heating

One of the interaction paths of electromagnetic waves with metal nanoparticles is via absorption (see Section 2.1). The relationship of the power density to the total absorbed power P is $P = \int p(r)dr = C_{\text{abs}}I$. Obviously the absorbed power is maximal if the illumination wavelength is in resonance with the particle. If not only one wavelength is used all scattering cross-sections have to be accounted for with the corresponding illumination intensity.

To reach a steady state temperature distribution a certain time is needed. This time depends on the characteristics of the system's material, the mass density ρ and the thermal capacity c_p. Estimations of the time scale lead to [67]:

$$\tau \sim R^2 \frac{\rho c_\mathsf{p}}{\kappa} \tag{2.13}$$

R: typical length of the system

ρ: mass density in $\frac{\mathsf{kg}}{\mathsf{m}^3}$

c_p : thermal capacity in $\frac{\mathsf{J}}{\mathsf{kg\ K}}$

κ: thermal conductivity in $\frac{\mathsf{W}}{\mathsf{K\ m}}$

This characteristic time is described by the material constants of the slowest participating process. As the thermal conductivity for gold is much larger than for water ($\kappa_\mathrm{Au} = 318\,\frac{\mathrm{W}}{\mathrm{K\ m}} \gg \kappa_{\mathrm{H_2O}} = 0.6\,\frac{\mathrm{W}}{\mathrm{K\ m}}$), it is reasonable to use $(\rho c_\mathrm{p}/\kappa)_{\mathrm{H_2O}} = 1.43 \cdot 10^{-8}\,\frac{\mathrm{m}^2}{\mathrm{s}}$[8] as characteristic value of the system. A typical sphere size in this thesis is $R = 30\,\mathrm{nm}$, thus, the resulting time scale calculates to $\tau \sim 62\,\mathrm{ns}$. Comparison of this time scale with the repetition rate of the white light laser used (80 MHz → one pulse every 12.5 ns) accounts for the treatment as a continuous wave laser. If this would not be the case, a time dependent analysis had to be taken into account. In literature, this is done for femtosecond laser pulses [68, 69].

After I have shown that a steady state configuration will be reached, I will discuss how the temperature distribution looks. Due to the high thermal conductivity of gold a homogeneous temperature ΔT_NP inside the particle can be assumed if the particle size is moderate. In the case of a sphere, an analytical solution can be found, resulting in the establishment of a $1/r$ decay of the temperature outside the particle:

$$\Delta T(r) = \Delta T_\mathsf{NP} \frac{R}{r} \tag{2.14}$$

For other geometrical shapes the solution has to be found numerically. Notice that the absorption of water in the visible regime can be neglected. ΔT_NP is given by Baffou et al. to be [67]:

$$\Delta T_\mathsf{NP} = \frac{C_\mathsf{abs} I}{4\pi R \kappa_\mathsf{surrounding}} \tag{2.15}$$

Figure 2.7 shows the temperature increase calculated by Equation 2.15 for gold spheres of several sizes in water (blue) and for a 60 nm gold sphere in polymer (gray) with $\kappa_\mathrm{polymer} = 0.2\,\frac{\mathrm{W}}{\mathrm{K\ m}}$.

---

[8] In literature the term $\rho c_\mathrm{p}/\kappa$ can also be found as thermal diffusivity D.

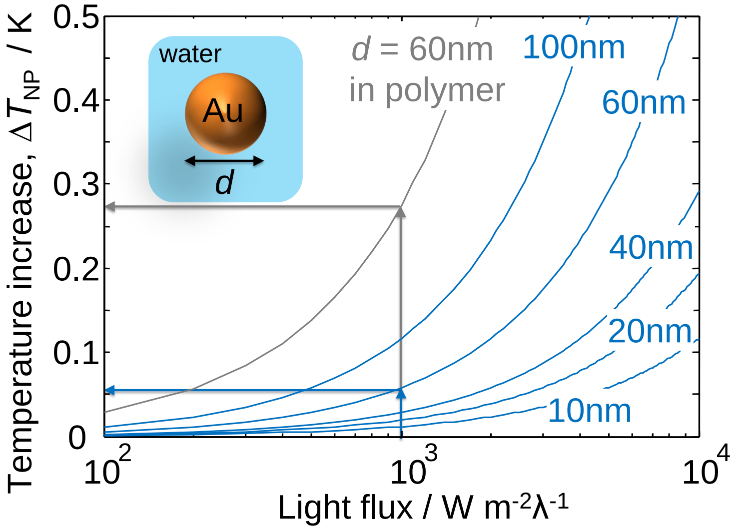

Figure 2.7: Calculated temperature increase for differently sized Au nanospheres in water. The gray line shows the temperature increase of a d = 60 nm Au sphere surrounded by polymer. The laser intensity of the Super-K Power white light laser is $10^3\,\mathrm{Wm^{-2}}\lambda^{-1}$ and the respective temperature increase is marked with arrows.

Notice, the strong illumination of nanoparticles can also lead to a melting and reshaping of the metal itself. As a result rods show a blue shift of the resonance wavelength when transforming into spheres [70, 71]. Similar transformation into spheres is also observed for other original nanoparticle shapes [72]. This kind of transformation was not seen during my experiments, only the creation of bubbles when illuminated with the SuperK-Extreme white light laser with a focused beam at 100 % power was observed.

Optical heating of dimers

In Section 2.3 the variation of the resonance wavelength in a dimeric structure was discussed. Also the creation of hot spots due to the enhanced near-field was mentioned before. With this background it is not surprising that also the temperature of closely situated nanoparticles is altered in comparison to the temperature of individual particles when illuminated. Govorov et al. calculated the total temperature change to be dependent on the number of assembled particles as well as the assembling structure. For a one dimensional structure in the limit of $N_{\mathrm{NP}} \gg 1$ he estimated:

$$\Delta T_{\mathrm{tot},\,t} \approx \Delta T_{\mathrm{max,0}} \frac{R_{\mathrm{Au}}}{g} ln[N_{\mathrm{NP}}] \tag{2.16}$$

$\Delta T_{\mathrm{max,\,0}}$: temperature increase at the surface of a single nanoparticle
g: gap distance
N_{NP}: number of interacting nanoparticles

The maximum temperature change reached with a dimer of 60 nm diameter particles is situated at the interparticle gap and is approximately twice as high as the temperature of a single particle. For the temperature increase of a single particle see Equation 2.15. The temperature will probably be even less as the mandatory condition of $N_{\mathrm{NP}} \gg 1$ is not sufficiently reached.

We can summarize that nanoparticle heating is an interesting effect but should only play a minor role for the work presented in this thesis. The maximum expected temperature increase is reached for the case of a polymer coated particle dimer and is less than 1 K. Despite this predicted non relevance of the effect, I will show in Chapter 6 that nanoparticle heating might be important.

As nanoparticle heating is a growing field I will give a short excursion into the subject in the following paragraph.

Heating a surrounding matrix

A very interesting application area is the photo thermal treatment of cancer cells [10, 73, 74, 75]. Particles with resonance wavelengths in the near-infrared regime are optimal candidates as tissue is transparent for these wavelengths. Due to heating of nanoparticles specifically localized in mutated cells, their cell death can be induced. But how much heat is really located within the direct environment of a particle? As one focus of this thesis is on PEG coated particles, I will briefly reflect some work of Govorov et al. [76]. They considered a gold nanoparticle covered with a polymer layer of thickness d_{polymer}. The heat released from the particle will first heat the polymer layer before reaching the surrounding water. Depending on the thickness of the polymer layer the heat is distributed according to one of the following processes: For thin layers the entire polymer feels the same mean temperature. An increase of the temperature results in a linear thickness increase. For thicker shells a two phase model is more accurate. The inner part of the polymer is already heated whereas outer regions are not influenced yet. In this scenario thermal expansion will also increase the polymer size with increasing light intensity. The time scale for such a stretching process lies in the millisecond regime. This theoretical derivation was shown to agree with an experiment where a nanoparticle was coated with a PEG layer. As indicator CdTe particles were attached in a flower like structure. Changing the light flux periodically resulted in a periodic variation of the emitted photo luminescence of the CdTe particles as the altered distance to the gold particle varied the strength of the quenching [77]. It should be noted that for functionalized particles ΔT_{NP} will be increased as the heat conductivity of a polymer is smaller compared to water and the absorption cross section increased. This can be also seen in Figure 2.7. Further experimental investigations focus on the melting of a surrounding ice matrix [78] which is checked by time resolved analysis of the Raman signal with the finding that this method allows to estimate the heat power generated by illuminated nanoparticles.

2.5 Total internal reflection illumination

The illumination mode of the Plasmon Fluctuation Setup mainly used for this thesis is via total internal reflection. Here, an evanescent wave, created at the surface where the sample is deposited, illuminates the nanoparticles. To have a good understanding of the light actually reaching the particle, I give a theoretical overview of the topic.

2.5.1 Basic concept

If a light ray passes from an optical thicker into an optical thinner medium, the ray is diffracted away from the axis of incident. At the critical angle the beam travels parallel to the medium boundary. Larger incident angles lead directly to total internal reflection. To determine the critical angle, Snell's law $\frac{sin\theta_\mathsf{i}}{sin\theta_\mathsf{t}} = \frac{n_\mathsf{t}}{n_\mathsf{i}}$ has to be used with the condition $\theta_\mathsf{t} = 90°$. The critical angle for a glass-water-interface is 62.4°. But, if no light could enter the thinner medium the story would end here and the basis of this thesis - evanescent illumination - would be missing. Therefore, lets move on to a more detailed consideration of the problem [79]. Thus, a reminder of Fresnel's equations which are valid also for condition of total internal reflection:

$$\begin{aligned}
q_{\mathsf{r}\perp} &= \frac{E_{\mathsf{r}\perp}}{E_{\mathsf{i}\perp}} = -\frac{n_\mathsf{rel} f_{\theta_\mathsf{i}} - 1}{n_\mathsf{rel} f_{\theta_\mathsf{i}} + 1} = -\frac{\sin(\theta_\mathsf{i} - \theta_\mathsf{t})}{\sin(\theta_\mathsf{i} + \theta_\mathsf{t})} \\
q_{\mathsf{t}\perp} &= \frac{E_{\mathsf{t}\perp}}{E_{\mathsf{i}\perp}} = \frac{2}{n_\mathsf{rel} f_{\theta_\mathsf{i}} + 1} = \frac{2\cos\theta_\mathsf{i}\sin\theta_\mathsf{t}}{\sin(\theta_\mathsf{i} + \theta_\mathsf{t})} \\
q_{\mathsf{r}\|} &= \frac{E_{\mathsf{r}\|}}{E_{\mathsf{i}\|}} = \frac{n_\mathsf{rel} - f_{\theta_\mathsf{i}}}{n_\mathsf{rel} + f_{\theta_\mathsf{i}}} = \frac{\tan(\theta_\mathsf{i} - \theta_\mathsf{t})}{\tan(\theta_\mathsf{i} + \theta_\mathsf{t})} \\
q_{\mathsf{t}\|} &= \frac{E_{\mathsf{t}\|}}{E_{\mathsf{i}\|}} = \frac{2}{n_\mathsf{rel} + f_{\theta_\mathsf{i}}} = \frac{2\cos\theta_\mathsf{i}\sin\theta_\mathsf{t}}{\sin(\theta_\mathsf{i} + \theta_\mathsf{t})\cos(\theta_\mathsf{i} - \theta_\mathsf{t})}
\end{aligned} \tag{2.17}$$

q: ratio of reflection (r), or transmission (t) with polarization
    $\perp$ perpendicular or $\|$ parallel to the plane of incidence
E_r, E_t, E_i: reflected, transmitted and incident field vectors
$n_\mathsf{rel} = \frac{n_\mathsf{t}}{n_\mathsf{i}}$: relative refractive index
$f_{\theta_\mathsf{i}} = \cos\theta_\mathsf{t} / \cos\theta_\mathsf{i} = \frac{\sqrt{n_\mathsf{rel}^2 - \sin^2\theta_\mathsf{i}}}{n_\mathsf{rel}\cos\theta_\mathsf{i}}$: ratio of the ray cross sections
θ_i: angle of incident
θ_t: emergent angle

As a side remark, it is interesting to note that if linearly polarized light is subject to total internal reflection the polarization state is found to be elliptically polarized. This implies a phase difference Δ between the components of the electric field. This phase difference is always positive with a maximum at $\tan\frac{\Delta_\mathsf{m}}{2} = \frac{1 - n_\mathsf{rel}^2}{2n_\mathsf{rel}}$ [79]. Under carefully selected conditions total internal reflection can produce circularly polarized light from linear polarized light.

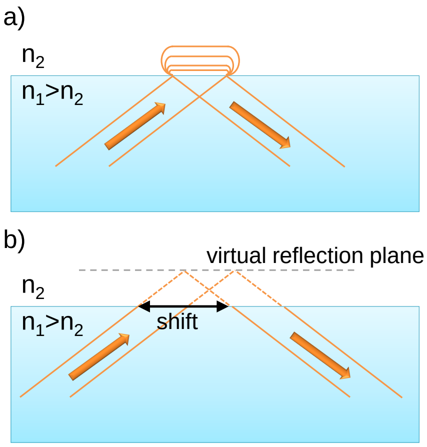

Figure 2.8: Visualization of a) an evanescent wave and b) the Goos-Hähnchen shift.

The mathematical explanation for total internal reflection is the mandatory condition of continuous tangential components of the electromagnetic field. To fulfill this demand at the interface of total internal reflection, the transmission ratio q_t has to be non-zero. An explanation to help visualize this is that the surface wave enters via diffraction at one boundary of the size limited spot with the result of energy leaking into medium 2 (see Figure 2.8a). The inserted energy is transferred back into medium 1 at the other side of the spot. The so introduced energy shift is called Goos-Hähnchen shift. A visualization for this effect is that the light beam is reflected at the virtual plane positioned inside the second medium at a distance in the magnitude of the penetration depth of the actual reflection plane (see Figure 2.8b).

The created surface wave, the evanescent field, can be described by plane waves as $\vec{E}_t = \vec{E}_{0,t} e^{i(\vec{k}_t \vec{r} - \omega t)}$ [80]. One feature of such an evanescent wave is that at least one component of k is imaginary and therefore no propagation in this direction takes place. As $\vec{k}_t \vec{r} = (k_t \sin\theta_t)x + (k_t \cos\theta_t)z$ and according to Snell's law $\cos\theta_t = \pm(n_t^2 - n_i^2 \sin^2\theta_i)^{1/2}$, we can conclude for the condition of TIR where $\sin\theta_i > \frac{n_t}{n_i}$:

$$k_t \cos\theta_t = \pm i k_t (n_i^2 \sin^2\theta_i - n_t^2)^{1/2} \equiv \pm i\beta \tag{2.18}$$

The parameter β describes the exponential decay of the evanescent wave with increasing distance to the surface. Analogously, we find $\sin\theta_t = \frac{n_i}{n_t}\sin\theta_i$. Combining all these pieces leads to the following equation for the evanescent wave:

$$\vec{E}_t = \vec{E}_{0,t} e^{-\beta z} e^{i(k_t x \sin\theta_i \frac{n_i}{n_t} - \omega t)} \tag{2.19}$$

Incident light with the polarization state either within the plane of incidence or perpendicular to it will create the same polarization mode within the evanescent wave. Nevertheless, the orientation of the pointing vector in the evanescent wave has altered and points now parallel to the reflecting surface. Also the amplitude of the two components is altered within the evanescent wave. For an incident angle of 72° and a glass-water-surface the parallel and perpendicular ratio of transmission q_t are plotted in Figure 2.9.

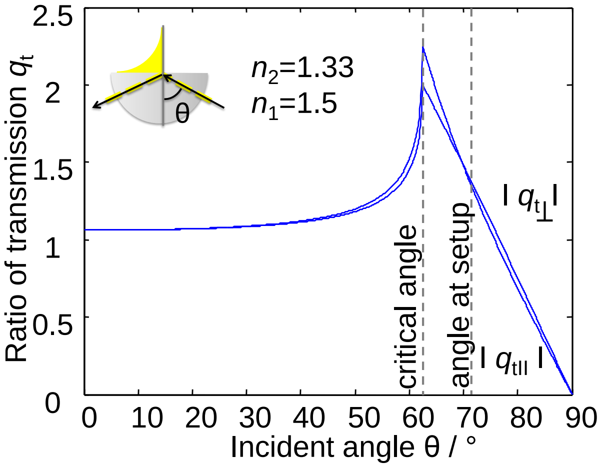

Figure 2.9: Polarization of the evanescent wave. Notice that the ratio of transmission can be bigger than 1. This is not in contradiction to the law of energy conservation as the energy is given by $f_\alpha n_{\mathsf{rel}} q_{\mathsf{t}}^2$.

After this general description of the basic concept of total internal reflection including information about the origin, the ratio of transmission and the obtained polarization states of the evanescent wave depending on the polarization of the incident light, I will now focus on the penetration depth of the evanescent field.

2.5.2 Penetration depth

In the previous section I have shown how to calculate the evanescent wave from Fresnel's and Snell's laws. Here, I will focus on the parameter β, which describes the exponential decay of the evanescent field. Due to the decaying field the scattered intensity of a particle is strongly dependent on its distance to the surface [81]. As we can see in Equation 2.18, β is dependent on four crucial factors: the angle of incidence, Θ_{i}, the wavelength of the reflected light, λ, and the refractive indices of the two media n_{i} and n_{t}. The inverse of β is defined as decay length. The distance dependent intensity is then described as follows:

$$I(z) = I_0 \exp(-z/\gamma), \quad \gamma = 1/\beta = \lambda/(2\pi\sqrt{n_{\mathsf{i}}^2 \sin^2\theta_{\mathsf{i}} - n_{\mathsf{t}}^2}) \tag{2.20}$$

I_0: scattering intensity at the surface

z: distance to surface

γ: penetration depth of the evanescent field[9]

λ: incident wavelength

n_{i}: refractive index of the substrate

n_{t}: refractive index of the medium over the substrate

θ_{i}: angle of incident illumination (see Figure 2.10)

---

[9] In literature other authors refer to a penetration depth of only half of the here presented height [82, 81].

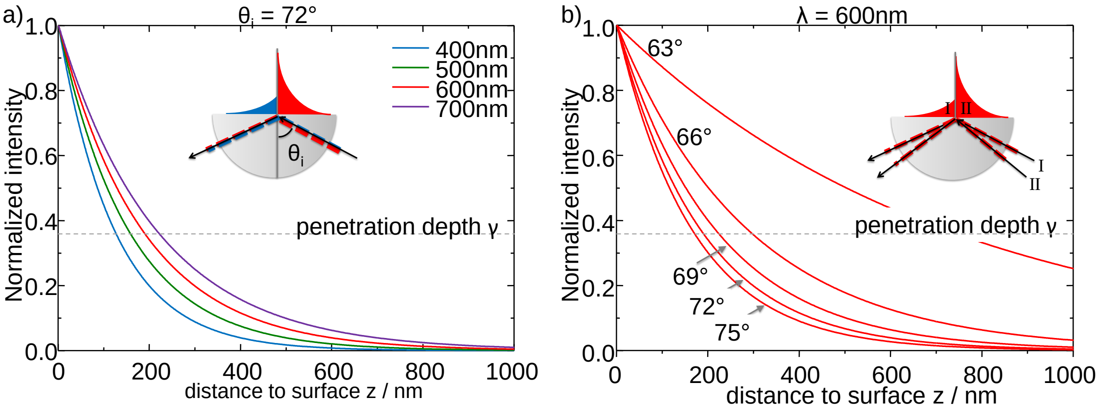

Figure 2.10: Penetration depth γ of the evanescent field in dependence of a) the wavelength and b) the angle of incidence.

The distance dependent intensity behavior is plotted in Figure 2.10 for several wavelengths and angles of incidence. With an illumination angle as used in the Plasmon Fluctuation Setup and with a mean illumination wavelength of 600 nm, a penetration depth of approximately 200 nm is achieved. An interesting remark is the effect of multiple scattering between particle and surface. It has been demonstrated that for large penetration depths this multiple scattering is increased leading to a non-exponential intensity profile [83].

After this section on the evanescent field created under total internal reflection, I will discuss the optical forces induced by such electromagnetic fields. In comparison I will present the optical forces generated by a Gaussian beam.

2.6 Optical forces

In optical fields all kinds of objects are exposed to forces. One example of such a force is the radiation pressure which plays a major role in astrophysics, e.g. during the birth of a star. The gradient force is a further example with great relevance to this work as it is felt by micro- and nanoparticles. Pioneering work of Ashkin was carried out on the subject of microscopic particle trapping in 1986 [84]. Since then, optical trapping of micrometer-scale particles has become a well established field. Shaping the light beam allows manipulation of the particle's movement. Due to the huge success on the micrometer length scale, scientists were inspired to move on to even smaller particles. Here, the challenge is the fall off of the responsible gradient force with the particles volume. Intrinsic forces, like Brownian motion, acting on the particle can easily destroy the trapped state [85]. In the following chapter I will present the subject of optical forces in more detail.

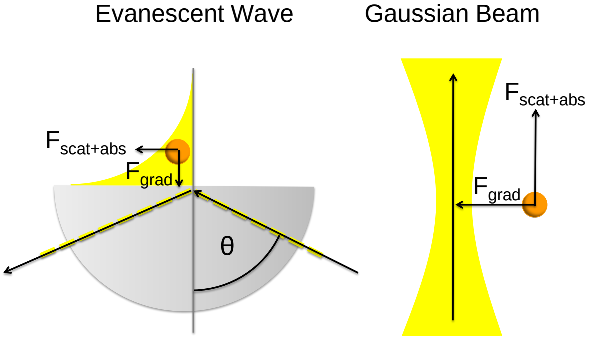

Figure 2.11: Optical forces in different illumination configurations. In the presence of an evanescent wave the gold particle is attracted towards the surface by the gradient force. Additionally, absorption and scattering force push the particle in the direction of the incident beam, but parallel to the surface. In the case of a Gaussian beam profile the gold particle is attracted inside the beam by the gradient force. The scattering and absorption components introduce a force parallel to the ray.

2.6.1 Trapping forces

In all cases of optical trapping two components need to be considered: the gradient contribution that attracts the particle towards the highest field value and the scattering/absorption component that pushes the particle in direction of the incident wave vector [86]. These two components are present regardless of the illumination method. Nevertheless, the individual direction will differ depending on the exact configuration. Figure 2.11 shows qualitatively the occurring forces for total internal reflection illumination and a Gaussian beam. The sizes of the respective forces are derived to be [87, 88]:

$$F_{\text{grad}} \propto Re(\alpha) \tag{2.21}$$

$$F_{\text{abs}} \propto Im(\alpha) \tag{2.22}$$

$$F_{\text{scat}} \propto \mid \alpha \mid^2 \tag{2.23}$$

α: see Clausius Mossotti relation (Equation 2.4)
$F_{\text{scat}} \ll F_{\text{abs}} \bigcap F_{\text{grad}}$: only absorption and gradient force need to be considered

Further analysis identifies the scattering and absorption force always to be positive. For the gradient force a material dependence exists for the sign. Gold is always attracted towards the highest field gradient. In contrary, silver shows two regimes. Depending on the wavelength used the particle can either be attracted or repulsed from the highest field location (see Figure 2.12).

For completeness, I will now briefly discuss the trapping of rods, especially as interesting experiments have recently been accomplished in this field. The conditions of forces are altered in the case of rods as two resonance peaks are present with perpendicular oscillation direction. In the case of a rod, where only the longitudinal plasmon is excited by linearly polarized laser light with a wavelength longer than the resonance wavelength, will align along the long axis. For rods in

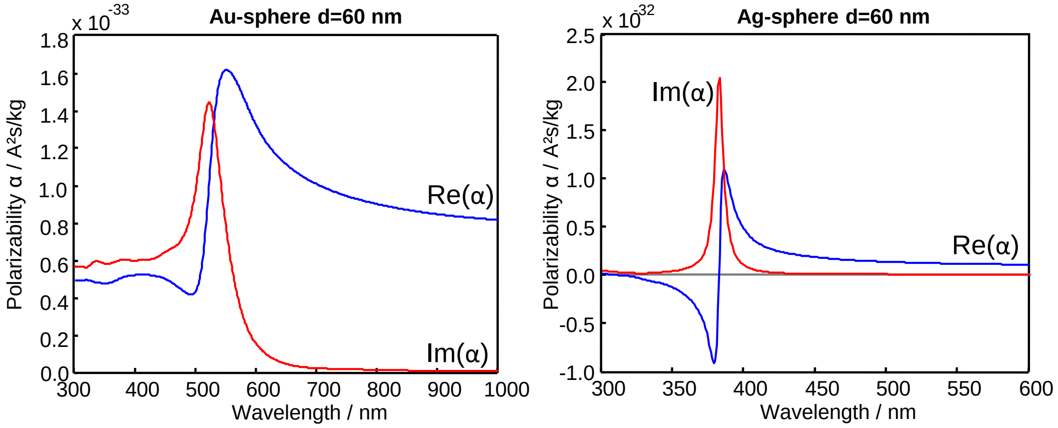

Figure 2.12: Real and imaginary part of the particle polarizability shown for silver and gold. As the imaginary part is proportional to the absorption force we obtain a positive value for both metal types. For the gradient force the sign is material and wavelength dependent.

solution this orientation has experimentally been shown [85, 88]. But as the orientation of rods in a trap is a complicated issue, as it depends on volume and aspect ratio of the trapped particle [88], other studies also show other possible arrangements depending on particle dimensions. Further, the orientation perpendicular to the electric and magnetic field is possible if the particles are large compared to the beam waist [89]. Recently Tong et al. even demonstrated periodic rotation of individual plasmonic silver and gold nanostructures using a single beam of linearly polarized near-infrared laser light [90]. Briefly, they used a laser at 830 nm with power density of 15-30 MW/cm^2 on the sample. The nanoparticle rotation was induced by rotation of laser polarization. The laser focus was situated in a manner that the absorption force pushed the particle onto the glass surface. Hence, the particle was hindered from moving away. Observation of the rotation was carried out with polarized white light illumination in a dark field microscope. Another field of particle trapping covers the immobilization of particles onto a surface. The manipulation and deposition of nanoparticles with a high precision can be achieved with focused laser beams [91, 92, 93].

Noticeable for an illumination with an evanescent wave, as in total internal reflection mode, is the angle dependence of the incident light. Lower gradient forces are obtained under larger incident angles θ_i. This is due to the amplitude of the electromagnetic field felt by the particle (see Section 2.5). But where is the best trapping regime? Another look at the curve for gold in Figure 2.12 provides an answer for gold spheres. The best wavelength is slightly red shifted with respect to the resonance position, more precisely at the right shoulder of the resonance peak, at a height of half the maximum intensity. Here, the real part of α has its maximum value. This wavelength induces the strongest gradient force. Nevertheless, the imaginary part is at half maximum intensity. Consequently the absorption force will still be of notable size. It can be further reduced by shifting the resonance further into the red regime. Gradient forces there drop, but stay at a usable level. Trapping in this regime resembles trapping of high refractive index dielectric nanoparticles [94]. Under these non-resonant conditions the first experiments of metal nanoparticle trapping were carried out in 1992 by Svoboda and Block [95].

For nanoparticles with sizes much larger than the penetration depth of light only the outer shell of the particle can interact with the electromagnetic field. This gives rise to a quadratic relationship between particle radius and force [94].

It must, however, be mentioned that due to the strong illumination needed for trapping, heating of the particle cannot be avoided (see Section 2.4). This makes trapped metal nanoparticles less interesting for biological experiments due to the possibility of serious damage of sample tissue. Furthermore, the temperature increase causes changes in the dielectric function and therefore introduces variations of the trapping condition [96].

2.6.2 Optical forces between illuminated nanoparticles

The configuration of the system discussed now is similar to the system of dimers discussed before (see Figure 2.4). Furthermore, the origin of the attractive force between nanoparticles in close proximity is closely related to the red shift in resonance wavelength of coupled nanoparticles. As we have seen in Section 2.3, the electromagnetic field will induce a dipole in each particle. If the polarization of the light is parallel to the interparticle axis, the dipoles are oriented head to tail and the force is attractive. With perpendicular polarization the dipoles are oriented in parallel with the positive charge in the same direction and the resulting force is repulsive. Hallock et al. predict this dipole-dipole interaction force, as it is caused by the illuminating light, to scale linearly with the intensity or alternatively the square amplitude of the electric field E^2. In the situation of two particles, the electric field gradient is introduced bidirectional by the particles themselves. Each particle is attracted towards the hot spot between them [97].

Further theoretical studies show different, not monotonic results in the magnitude of force. Chu and Mills find theoretically the attractive force to be strongly distance dependent with maximum forces at distinct gap sizes [98]. Here, the optical forces are largely overruling the van der Waals force by several magnitudes.

For silver dimers, a repulsive wavelength regime is in agreement to the repulsive forces also depicted for one particle. Choosing the illumination wavelength correctly will therefore introduce a stable separation distance [99].

Experimental work so far is limited. Nevertheless, some interesting publications should be mentioned. Svedberg et al. used optical tweezers to move a single silver nanosphere into the direct environment of another already immobilized sphere [100]. Due to the optical force between the two particles an optical binding was realized. Investigated was the close approach by surface enhanced Raman scattering (SERS). Individual particles did not show a signal whereas in close configuration a signal was measured, induced by the hot spot between the two particles. Astonishing in this experiment is that for SERS enhancement, particles have to be approximately within one particle radius distance, but the dimension of the optical trap is defined by the beam waist which is in the order of 1 µm. Conclusively, there has to be a strong attractive force between the two particles.

Another related research, carried out in the Feldmann labs, reports on a coupling strengthening between two silver particles in an optical trap followed by a spontaneous escape from the trap [101]. The strengthening of the interparticle trapping force between two spheres is followed via a gradual plasmon redshift. Reasons for the destabilization of the trap are still discussed. The two considered candidates are strong heating with induction of increased Brownian motion and change in the gradient force due to the resonance change of approaching particles.

The dimerization of two gold spheres in solution induced by a NIR laser was recently shown by Tong et al [102]. Noticeable is the reversible dimerization regulated by the illumination of the laser. If the laser is turned off two 'green' spots are released, indicating single Au particles.

Heterodimers

In the case of two non-identical nanospheres, a breaking of the symmetry occurs. The sign of the force can change in comparison to a homodimer, resulting in a repulsive interaction between the particles for parallel illumination. Vice verse an attractive interaction for perpendicular illumination is possible [103]. However, in a detailed analysis the wavelength dependence of these effects also has to be considered. To give a visualization of this situation we can picture the difference of resonance frequency depending on the size, resulting in a dephasing of the two oscillations. As the resonance position of spheres only changes with tremendous size variations, it is not of interest in homodimers even though the standard deviation of monomer sizes is quite broad.

Hot spot trapping

Also the hot spot between two nanorods with a tip to tip configuration can be used for trapping and sensing simultaneously. A diffusing particle will be attracted towards the high field intensity between the particles. There, it can be monitored by the resonance wavelength of the system. A recent exciting experiment is the trapping and sensing of 10 nm metal particles using a lithographically produced plasmonic dipole antenna [104]. As trapping laser a 808 nm laser is used and the diffusing particle is attracted into the interparticle gap as the near-field is elevated there. The detection of the captured nanoparticle which is causing a red shift of the system's resonance wavelength is done with a common white light illumination in dark field mode.

2.6.3 Conclusion

In the last section, I have introduced the two major optical forces, absorption and gradient force, felt by an illuminated nanoparticle. The absorption force is an impulse force pushing the particle in direction of the Poynting vector of the light. The gradient force is material and wavelength dependent. For a gold particle this force is attractive in direction of the highest field gradient. If the illuminated particle is a rod, the polarization of the incident light as well as the nanoparticle volume and aspect ratio have to be considered to determine the trapping orientation.
I have also addressed the question of optical forces between illuminated nanoparticles, as this dimer system is studied in Chapter 6, with the finding that to this day different, partially contradicting theories are discussed. In my eyes, the most reasonable one is given by Hallock et al. [97] as their theory explain my findings best. A linear scaling of the interaction force with the light intensity is assumed. Furthermore, they predict that particles once pulled together do not leave this configuration anymore as they are stabilized by van der Waals force.

I conclude that the large number of recent publication about optical forces on nanoparticles shows the potential of this topic for future projects. The possibility provided by optical forces seems manifold: exact particle direction and positioning, light induced switches on the nanoscale, or the induced aggregation/separation of nanoparticles perhaps even in living cells.

3 A Single Nanoparticle as a pH-Sensor

Methods to measure the pH of solutions in large volumes are well established with methods such as pH-paper or pH-electrodes. However, the measurement of pH in localized environments, e.g. in living cells, is not straight forward due to their small size and the environmental demand for vitality, but still of high interest for understanding biological processes within the cell metabolism.

Attempts to build pH-sensors based on nanoparticles consisting of e.g. silica or polymers are numerous, including non plasmonic particles functionalized with pH-responsive polymers [105, 106, 107]. To read-out the pH, the size of the particle was determined via light scattering. Despite the use of nanoparticles, the read-out method still requires a relatively large sample volume commonly in the micro liter regime. A promising strategy to further reduce this volume includes single plasmonic particles and will be presented in this chapter.

3.1 Basic concept of plasmonic nanoparticle pH-sensing

Single *plasmonic* pH-sensors may be used to map pH-changes on small objects, e.g. vesicles in biological cells, without the problem of photo-bleaching, which is always a complicating factor for organic dye based pH-sensors [108]. Therefore, the pH can be investigated over longer periods in time compared to dye based experiments. Another advantage of using nanoparticles as sensors is the recently shown ability of using plasmonic nanoparticles for photo thermal therapy of cancerous cells [109]. In the future, nanoparticles might therefore combine sensing and treating abilities in one [110]. In the next paragraph I give a brief summary of existing methods of plasmonic pH-sensing in literature.

The earliest pH-sensors made from plasmonic particles are based on the aggregation of nanoparticles in response to a change in the environment [42, 111, 112]. Due to plasmon coupling the color of the solution changes (see Section 2.3) which indicates that the target is present. Another popular strategy is the grafting of smaller plasmonic satellite particles onto a core particle via a responsive polymer [113]. If the surrounding condition is now changed, the distance between the satellites is altered and coupling strength is modified, resulting again in a color change of the solution. Also, routes where the refractive index of the particle's functionalization induced by altering surrounding conditions varies are demonstrated in ensemble measurements [114, 115, 116]. In reports by Li et al. as well as by Nuopponen and Tenhu, the spectral shift of plasmonic nanoparticles coated with pH-responsive polymer was determined via simple extinction spectra measured on ensembles of particles. They did not fully exploit the major advantage of nanoparticles, i.e. the very limited sensing volume due to their diminutive size.

Despite the well known possibility of using these nanoparticles in single particle experiments, to my knowledge, no studies on single pH-responsive nanoparticles can be found in literature. Therefore, I extended the plasmon sensor concept to

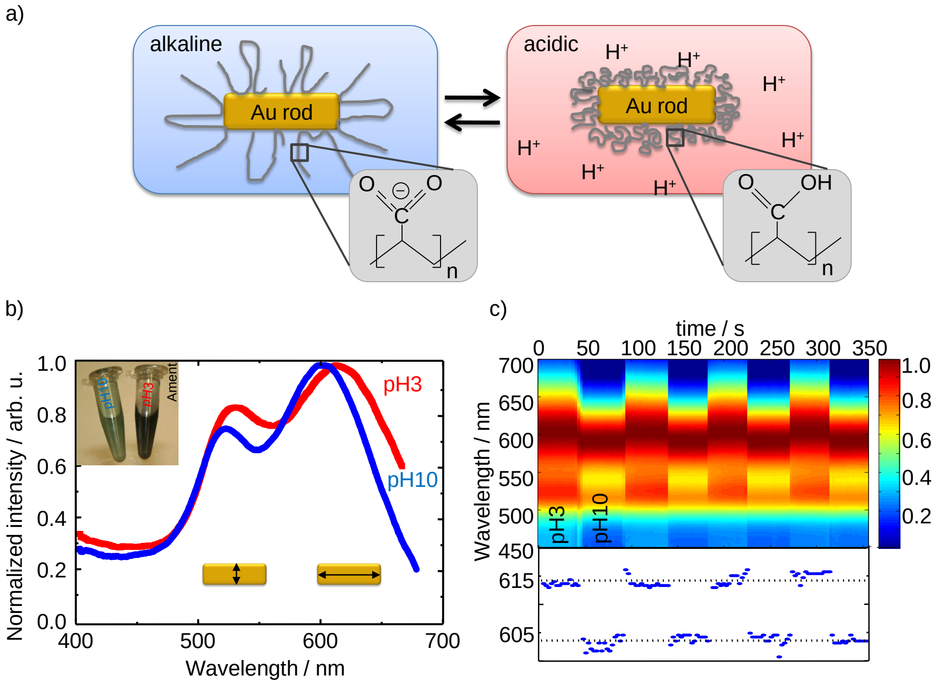

Figure 3.1: a) Concept of a plasmonic pH-sensor. The nanoparticle is functionalized with a pH-responsive polymer. As a result of a pH-change the refractive index of the local environment changes. b) Ensemble spectrum of gold rods with pH-sensitive coating at pH 3 (red) and pH 10 (blue). The two peaks correspond to the short and the long axis of the rods. c) Continuous trace of the normalized extinction spectrum of a pH-sensitive nanoparticle solution. Starting at pH 3 then changing to pH 10. In the lower part of the graph the respective resonance wavelength is plotted.

single particle pH-measurements using poly(acrylic acid) (PAA) as pH-responsive polymer coating, delivering the local pH of the environment. The charges of the carboxylic side groups depend on pH-conditions and therefore the packing density changes when the pH-value is varied [117] (see Figure 3.1a). The sensor is responsive to the local pH in an attoliter volume and is sensitive to pH-changes between pH 3 and pH 10. Single particle spectroscopy on the particles was performed via dark field microscopy with the 'fastSPS' setup (see Appendix C.1).

Prior to presenting the experimental findings, I provide a Section on sample preparation in case the reader is interested in these details.

3.2 Sample preparation

Coating of gold nanorods with poly(acrylic acid)

PAA with an average molar weight of 450 kg/mol was purchased from Aldrich. 1Ethyl-3-[3-dimethylaminopropyl]carbodiimide hydrochloride (EDC) was purchased from Thermo Fisher Scientific. L-Cysteine was purchased from Merck. Hydroxylamine hydrochloride was purchased from Sigma Aldrich. All chemicals

were used as received. Deionized water (18 MΩ) from a Millipore system was used throughout.
The gold nanorods were prepared by the method described in Appendix A using 10 µl of 0.04 M silver nitrate per 10 ml growth solution. For the coating of gold nanorods with PAA 1 ml of the original particle solution was centrifuged (5470 rcf, 10 min) and resuspended twice in deionized water to remove the excess of surfactants and unreacted products.
For the ensemble measurements, the pellet was filled up with 1 ml of PAA solution with a concentration of 200 µg/ml.
For single particle measurements the polymer had to be bound covalently to the nanorods to avoid the removal during pH-adjustment. To achieve covalent binding, the polymer first had to be coupled via EDC-coupling to cysteine which then covalently bound via a sulfur group to gold. Therefore, PAA was dissolved at 10 mg/ml in 2-(morpholino)ethanesulfonic acid (MES) buffer solution (0.1 M). For complete dissolution, the mixture was treated in the ultrasonic bath for 1 h and left overnight on a shaking table. EDC and cysteine were dissolved separately in phosphate-buffered saline (PBS: 0.01 M phosphate buffer, 0.0027 M potassium chloride and 0.137 M sodium chloride) solution. Directly after preparation, 1 ml EDC solution and 1 ml cysteine solution were mixed with 10 ml PAA solution (concentration cysteine and EDC: 2.22 mM, concentration PAA: 0.022 mM) and shaken overnight. The pellet of gold rods was then filled up with 1 ml of the cystein coupled PAA solution (0.2 mg/ml). In order to break the thiol bonds 10 µl hydroxylamine with a concentration of 0.13 M was added. This mixture was then shaken for half an hour before usage.

Microscope slide preparation and deposition of PAA-coated rods

Roti-Liquid Barrier Marker was purchased from Roth and applied to a Hellmanex cleaned microscope slide surrounding a 2 x 2 cm^2 rectangle. Then, 5 µl of the PAA functionalized nanorod solution was dropped onto the glass slide. Subsequently, 10 µl of 1 M sodium chloride solution and 100 µl deionized water were added. After 10 min of incubation, 400 µl of deionized water was added.

3.3 Ensemble measurements

As proof of principle I first investigated gold rods with electrostatic bound PAA in ensemble measurements (see Appendix C.2). The pH was adjusted by adding 1 M hydrochloric acid (HCl, Merck) or 1 M sodium hydroxide (NaOH, Merck). The extinction spectrum of a bulk measurement shows two maxima (see Figure 3.1b). Each maximum belongs to one of the two axes of a rod. In both axes the expected reversible shift can be seen. Since the peak of the long axes is more influenced and more intense, analysis focuses on this peak. The resonance position in acidic conditions was in mean (614.3 ± 1.0) nm (the error quoted is the standard deviation of all measurements under the same pH-conditions; 60

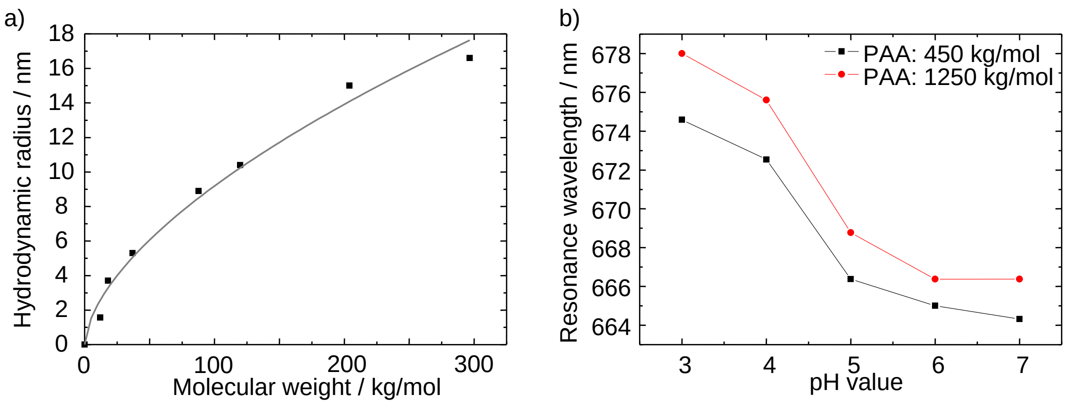

Figure 3.2: a) Hydrodynamic radius of PAA polymers of different molecular weight taken from Reith et al. [118]. The gray curve is a fit with the equation for the Flory radius $R_H = aN^{0.6}$ resulting in a monomer length *a* of approximately 0.14 nm. N is the number of monomers in the chain and was calculated via the monomer molecular mass of approximately 94 g/mol also taken from the stated literature. b) Resonance wavelength of nanorods coated with PAA of molecular weights of 450 kg/mol and 1250 kg/mol incubated in buffer solutions of different pH.

measurements in acidic conditions – 62 measurements in alkaline conditions). In an alkaline environment I obtained a mean peak value of (603.7 ± 0.9) nm. This corresponds to an average shift of 10.6 nm between pH 3 and pH 10. Figure 3.1c shows the results of the continuous measurement over four repetition cycles. I obtained the expected reversible shift. Increasing or decreasing the pH further did not shift the resonance position any further into the respective wavelength direction. Therefore, complete protonation/deprotonation of the side groups was achieved. Investigating the resonance position in acidic conditions more carefully reveals a slight shift (1.7 nm in four cycles) to higher wavelengths during the four repetition cycles. An explanation might be the accumulation of NaCl in the solution over time. Furthermore, the change in refractive index was accompanied by a change of the surrounding polymer layer thickness [117]. Luckily this did not need to be considered here, as the dense polymer layer could be assumed to be in the size regime of the diameter of the coiled PAA polymer. To verify this, literature values were fitted with the equation for the Flory radius $R_H = aN^{0.6}$ to determine the monomer length a knowing N the number of monomers in the chain [118, 119] (see Figure 3.2). Then, the diameter of the PAA used could be estimated to approximately 45 nm. Thus, the sensing distance is much smaller than the polymer dimension and only the refractive index change is of interest. QSA calculations of the two conditions with refractive indices of 1.5 and 1.4 for the coiled configuration and the stretched configuration, respectively, resulted in a resonance shift of 18 nm. The slightly smaller experimental shift of 11 nm is reasonable and might be attributed to the assumptions of refractive index values for the calculation.

From literature it is known that charges can influence the resonance wavelength [21]. To rule this out as a possible reason for the obtained resonance shifts,

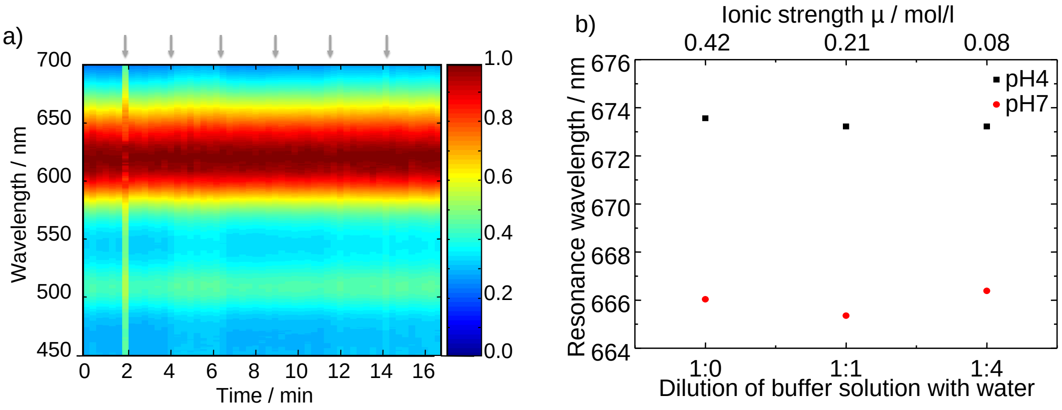

Figure 3.3: a) Independence of the resonance wavelength of an uncoated rod from the pH-value of the surrounding solution. Gray arrows indicate the pH-change. b) Independence of the resonance wavelength from the ionic strength of the phosphate/citrate buffer solution for two prepared pH-values.

I carried out two control measurements. First, I repeated the same ensemble measurement in changing pH, but with CTAB-coated rods. No shift could be determined in this case (see Figure 3.3a). This identifies the structural change of the polymer as the source of the shift. Second, I investigated the resonance position in dependence of the ionic strength[10] of the solution prepared by simple dilution with pure water. No correlation between ionic strength and resonance shift was observed (see Figure 3.3b).

3.4 Single particle measurements

The sample used so far was not stable enough to be used for reversible nanosensors in single particle experiments. When exchanging the liquid to adjust the pH, the polymer was washed away and the particles lost their pH-response. Hence, a covalently bound polymer coating was necessary. This was accomplished using EDC-coupling [120]. An amide bond was formed between cysteine and PAA, the cysteine was then covalently bound with its thiol side group to the gold rod. For investigations in the microscope, the sample was immobilized on a glass slide[11]. In order to remove floating particles the water was exchanged several times. Here, and in all later exchanging-steps, I used a pipette and exchanged only approximately 70 % of the solution as I did not want the surface to fall dry. After these washing steps, the water was replaced with a phosphate/citrate buffer to control the pH of the system. The buffer solutions used matched pH 3 and pH 7 and were controlled with a pH-meter (QpH 70, VWR). They allowed changing the pH and buffering it at the desired pH. As a control, the pH was checked after the

---

[10] The ionic strength I is defined as $I = \frac{1}{2}\sum cZ^2$ with c molar concentration of the ion and Z charge of that ion.

[11] I have not used a flow cell to be able to directly access the solution to measure the current pH.

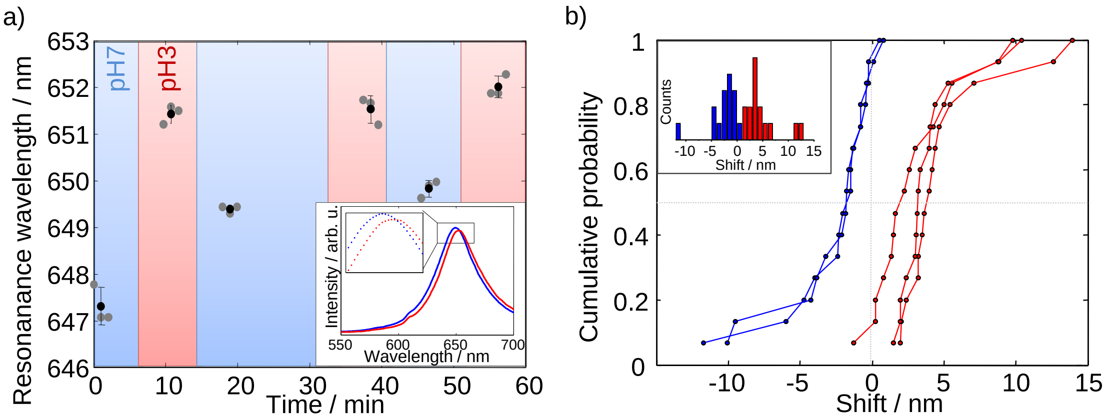

Figure 3.4: a) Resonance wavelength of a single nanoparticle in changing pH-conditions tracked over time. The inset shows the entire resonance peak of the different spectra. c) Statistical data of plasmonic pH-sensors. Shown is a cumulative probability of the shift into the acidic (red) and back to basic (blue) for several cycles.

exchange with pH-paper. The spectral shift of the resonance position of different particles was investigated with a dark field microscope. I monitored the spectrum of the same particle in differently buffered environmental pH-conditions. Thus, I gained information about the dependency of the resonance position on the pH. The setup used is described in Appendix C.1. In the single particle experiments I took three measurements for each buffered pH-condition with a time separation of one second. Exposure times were 30 seconds. After measuring in one pH-condition, the buffer solution was exchanged stepwise to the other pH before starting a new series of measurements. This procedure was repeated for three cycles. Initially, the particles were immersed in phosphate/citrate buffer adjusted to pH 7; one exemplary selected particle (see Figure 3.4a) displayed a resonance wavelength of (647.3 ± 0.4) nm (the error quoted is the standard deviation from three independent measurements). Exchange of the surrounding solution with pH 3 adjusted phosphate/citrate buffer shifted the resonance position to (651.4 ± 0.2) nm. Further exchanges of the solution showed nicely the reversible shift of the resonance position. In the chosen particle the first shift is larger than later ones. Similar behavior, one shift being bigger than others, could be seen for other particles, too. I explain this unexpected behavior with an optimization of the polymer folding. In the inset of Figure 3.4a, scattering spectra of the two conditions for the discussed particle can be seen. One spectrum was taken from acidic (red) pH and one from alkaline (blue) pH-conditions. The same data as above is available for 15 particles measured in the same experiment in parallel. These data are plotted in a cumulative probability plot shown in Figure 3.4b. Considering all particles, I observed a median shift of 4.8 nm after the first exchange of liquid. Resonance shifts between acidic and basic condition in later cycles were: -2.6 nm, 3.1 nm, -2.7 nm, 4.0 nm. As the size of the shift was influenced by the number of bound PAA molecules as well as from the binding position, which differ statistically from particle to particle, I observe a large deviation in the shift from one to another

particle. This indicates the necessity of the carried out statistic. However, the different shifts of one particle will always stay approximately same size. As the blue shifts were smaller then the red shifts, a general small red shift was overlaying the reversibility of the system. As discussed earlier, the reason might be the optimization of the polymer folding behavior differing for each folding event. Further investigations for clarifying the effect need to be carried out.
As a control experiment, I tried to investigate CTAB gold rods in our dark field setup. Incubating with pH 7 buffer washed particles away, thus, no investigation was possible.

Comparison of the shift in the ensemble measurement and in the single particle measurement reveals a difference in magnitude. The shift in the single particle experiment is only approximately half the size of the shift in the ensemble measurement. This might be explained with the immobilization of the particles on the glass slide. Therefore, the polymers attached on the lower side of the rod were not affected by the pH-changes as solution could not enter this region easily.

3.5 Conclusion

pH-sensitive particles were prepared by using either simple incubation method or EDC-coupling to functionalize the gold nanorods with a pH-responsive polymer coating. This composition features a pH-dependent resonance position of the plasmon peak, which was investigated in ensemble measurements as well as in dark field single particle measurements. I have been able to show the reversible shift in both cases. To my knowledge, this reversible pH-behavior of single rods is shown here for the first time. The presented pH-sensor neither blinks nor bleaches and can be a good alternative to dyes. Another advantage of single nanoparticles as sensors is the small probing volume. Therefore, the local detection of changes in an attoliter volume is possible.

4 Plasmon Fluctuation Setup

Interesting effects on molecular scale such as reversible binding events normally happen on short time scales requiring a setup that maximizes time resolution. At the start of my work, time resolution to measure single plasmon spectra was in the regime of several tenths of seconds. This long exposure time was required to acquire a sufficient number of photons as dark field microscopy setups were mainly equipped with a halogen lamp for illumination and a charge coupled device (CCD) camera for detection. Recently, two interesting new products for improving the capability of a plasmon detection setup have become commercially available: white light lasers (WLL) for stronger illumination and electron multiplied charge coupled device (EMCCD) cameras for better detection. These two components are the key components of the Plasmon Fluctuation Setup presented in this thesis and have the following advantages: the WLL increases the number of photons at the sample and therefore the number of photons scattered by the sample. The EMCCD camera improves spectral resolution at short time scales due to the implemented electron multiplication. Besides the camera is equipped with a 'crop mode' read-out mode, allowing one to acquire particle spectra with rates up to 20 kHz, a frame rate not reached with older CCDs.

In the following chapter, I describe the newly developed Plasmon Fluctuation Setup and discuss its specialties in comparison to instruments used so far. Characteristics of the Plasmon Fluctuation Setup are a much faster acquisition time and an improved spectral sensitivity. Furthermore, I study the influence of the existing noise terms in respect to the quality of the measurements.

4.1 Experimental setup

Figure 4.1a shows a scheme of the experimental setup. The core of the device consists of an upright transmission microscope (Zeiss Axioskop). For illumination I included a supercontiuum white light source (Koheras SuperK-Power) with a wavelength range from 460 nm to 2400 nm and total output power of 2.8 W. Further characteristics of the WLL are a visible spectral power density above 1 mW/λ in the regime of 470 nm-670 nm, a pulse width of 5 ps, and a repetition rate of 80 MHz. The light of this WLL is coupled onto the sample via total internal reflection (see Section 2.5), achieved with a glass half cylinder situated directly under the sample holder. The evanescent wave created by total internal reflection illuminates the sample. The scattered light coming from the sample is collected by a 40x air objective (CP-Achromat, NA 0.65) and transmitted to a dispersive element (Specim ImSpector V8). An EMCCD camera (Andor iXon DV885) is the detector.

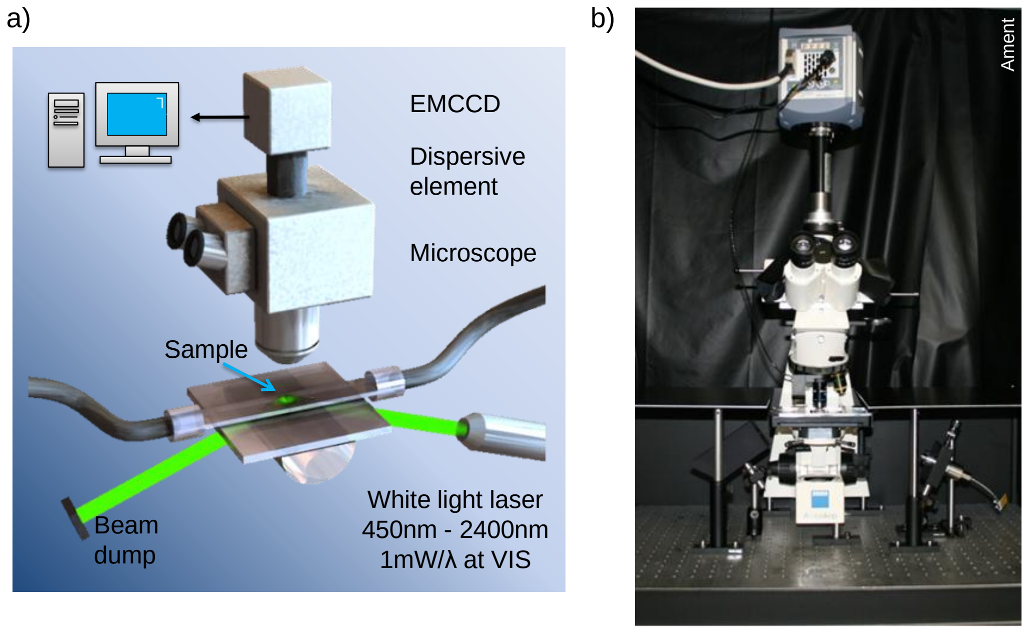

Figure 4.1: Plasmon Fluctuation Microscope. To improve time resolution and sensitivity of the setup two main changes in comparison to other plasmon investigation setups are implemented. To increase the intensity of the illumination a supercontiuum white light source is coupled in via total internal reflection. Furthermore, the sensitivity of the detector is amplified by introduction of an EMCCD camera.
The 3D visualization of the microscope was done by .

Crop-mode

The 'crop mode' read-out is the fastest read-out mode available for this camera. It uses the area of the sensor chip not needed for data acquisition as fast memory. Thus, no light is allowed to fall onto this area as it would spoil the quality of the signal. Therefore, a second slit at the position of the entrance slit of the dispersive element is introduced in the detection pathway. As the two slits are perpendicular to each other they act as pinhole; only light from a small area is transmitted to the spectrometer and then to the detector.

Special setup characteristic

The configuration of illumination introduces some characteristics special for this setup. Especially the use of the half cylinder which couples the light beam onto the sample introduces some further effects. First, the illuminated area is ellipsoidal with a maximum power density at the center and a Gaussian intensity distribution towards the edges of the spot. Measuring the spot size with a color image at the ocular position determines the spot size ($1/e^2$ intensity drop) to be $1.13\,\mathrm{mm}^2$. Second, due to the spatial dimension of the ray, not all parts of the beam hit the half cylinder with the same angle. The inner region hits the surface of the half cylinder at 0°, whereas, for outer regions a slightly bigger angle is the case. Therefore, the outer regions are refracted in direction of the center of the ray. The half cylinder effectively focuses the laser beam. Furthermore, this focusing effect is wavelength dependent, creating a color fringe at the boarders of the spot at the TIR surface. The dimension of the inhomogeneous illumination is calculated to be approximately 6 µm. With a magnification objective of 40x, the entire field of view which is approximately 0.6 mm in diameter is illuminated homogeneously and the effect is negligible. Third, the intensity of the scattered light from a particle depends on its distance to the TIR surface (see Section 2.5).

Distance dependence of the scattering intensity

To quantify this effect of distance dependency of the particle to the surface in scattering intensity, I have probed the evanescent field intensity with 60 nm Au spheres, positioned at different distances to the surface. This was achieved by particle functionalization with PEG in different thicknesses. Two things can be learned from this experiment. First, functionalized particles further away from the surface scatter exponentially less light. However, as the dimension of the nanoparticle is not negligible and the particles with thin polymer layer additionally feel the glass substrate, it is not straight forward to obtain the penetration depth from the fit in Figure 4.2. Second, the scattered intensity of a naked particle is decreased due to the lower surrounding refractive index. Thus, the functionalization is not negligible (see Figure 4.2).

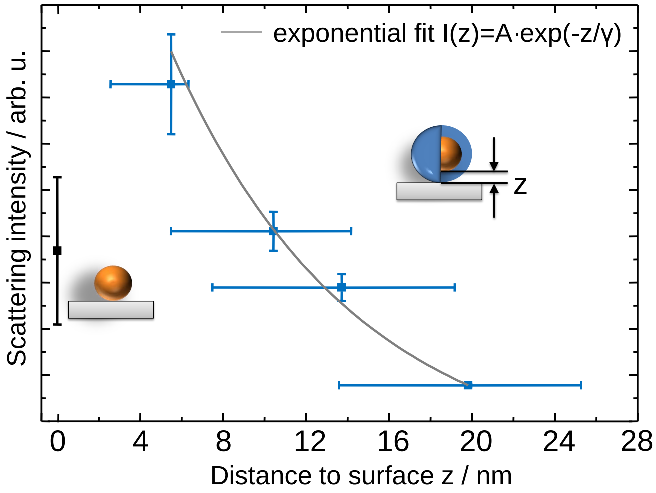

Figure 4.2: Scattering intensity of 60 nm Au spheres plotted versus their distance from the TIR surface. Details on the distance approximation can be found in Section 6.2. The black data point is taken from a citrate sphere without further functionalization. The blue data points correspond to PEG functionalized spheres. The distance of 20 nm was reached with additional BSA-biotin-streptavidin functionalization of the glass surface. The error of the scattering intensity is the mean standard deviation. The distance error reflects dimensions obtained by different theoretical models (also to be found in Section 6.2).

Limited refractive index of the medium surrounding the nanoparticles

Another illumination related effect is the limit in the refractive index of the sample solution to values below 1.41 induced by the incident angle of illumination. An increase of the refractive index above this value will annihilate total internal reflection at the glass liquid interface, shifting it to the glass air interface above the sample chamber. As particles are still illuminated, observation in the microscope is possible. Nevertheless, an additional interference pattern will superpose the particle spectrum and only careful white light correction on a nearby white scatterer can cancel it out. Side remark: If the latter is not done, the fringes might have another advantage. The sharp peaks of the interference pattern are defined by the distance between the glass slides and do not change their position if spectral changes in the plasmon resonance occur. Due to their sharpness, they might be used in future experiments to resolve small shifts of the under laying plasmon resonance peak.

4.2 Setup calibration

To conclude qualitative data from the measured plasmon spectra it was necessary to calibrate the pixel-to-wavelength relation of the EMCCD. This calibration was carried out with the help of two laser lines (532 nm and 655 nm, wavelengths were checked with a fiber spectrometer (see Appendix C.2)). One laser line after the other was directed onto the detector chip and a frame was acquired. Each laser peak had a width of approximately 5 pixels and was fit with a Gaussian to determine the exact pixel for linear calibration. The slope of the calibration line was calculated to be approximately (0.516±0.002) nm/pixel. As control experiment to verify the calibration obtained I measured one sample of rods in three different setups: The here presented Plasmon Fluctuation Setup, the fastSPS setup (see Appendix C.1) and the Bio Setup constructed by [121]. The good agreement of the data measured for all three setups is shown in Figure 4.3.

Spectral super resolution

The pixel dispersion of the spectrometer used in the Plasmon Fluctuation Setup is around 0.5 nm as derived in the paragraph before. By fitting the measured spectral data points of a spectrum, a large improvement in spectral resolution can be gained. Depending on the demands of the user on time consumption and precision, either a parabolic fit around the resonance peak or a fit with a Lorentz function can be carried out. The computational time for the parabolic fit is much smaller. If a large number of spectra has to be analyzed, the parabolic fit is of advantage. Also, it needs to be noted that for the same data points, a Lorentz fit provides smaller noise values than the parabolic fit. Whether this difference is due

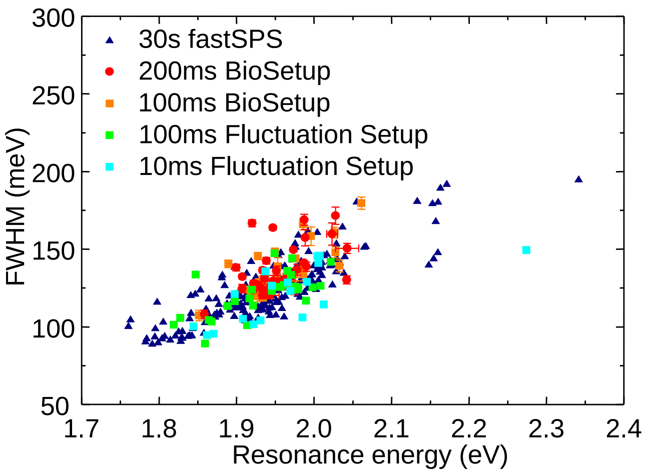

Figure 4.3: As calibration control one sample of rods was measured in three different setups. The fastSPS (see Appendix C.1, data provided by), the Bio Setup [121] and my Fluctuation Setup. Exposure times were adapted with respect to the setup. The high number of dark blue data points is attributed to the automated acquisition in the fastSPS setup not present for either of the other setups. Notice, due to laser safety reasons laser power at the Fluctuation Setup was only set to 20 % for 100 ms and 40 % for 10 ms.

to over estimation of the data or due to better data fitting was not investigated any further.

4.3 Setup performance

To demonstrate the potential of this fluctuation microscope for time resolved data acquisition, the spectral noise of differently shaped particles with changing exposure times were measured (see Figure 4.4). For each exposure time, the optimal gain condition was chosen to maximize signal quality by reaching the maximum number of measurable photons. The sample was prepared in the following manner. Three different kinds of as prepared / bought gold particles (see Appendix A) were diluted 1:50 in water and 5 µl were dropped onto a Hellmanex cleaned microscope slide. For immobilization, 10 µl of 1 M NaCl solution was added. After approximately 30 s a cover glass was put on top of the sample and the gap

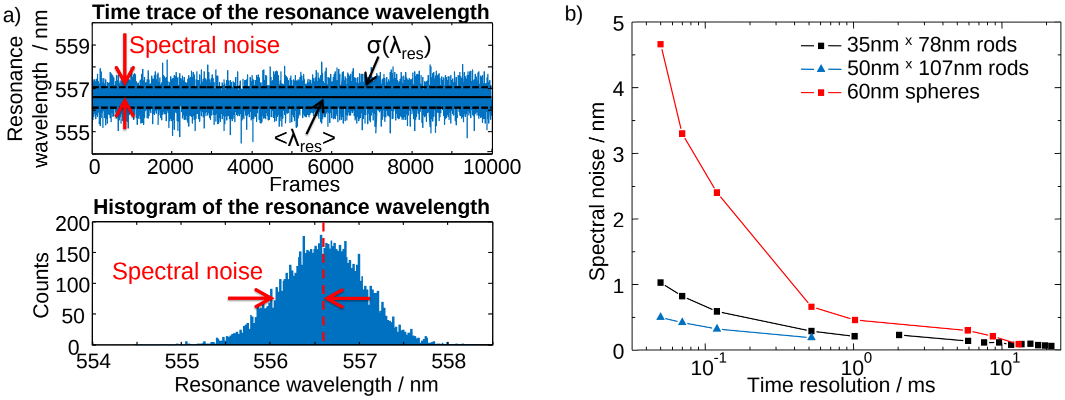

Figure 4.4: a) Definition of the spectral noise as used in this thesis. b) The spectral noise of the Plasmon Fluctuation Setup for differently sized particles is plotted over the respective time resolution. A trade off between time and noise is noticeable.

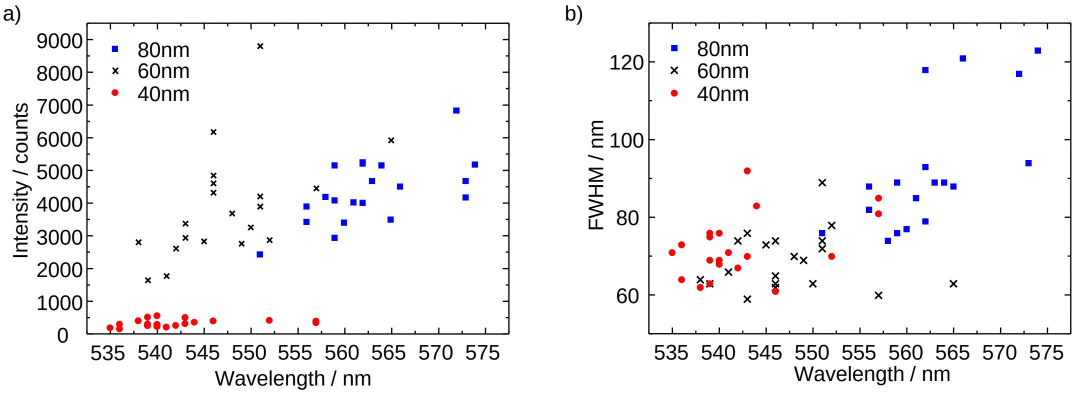

Figure 4.5: Intensity and *FWHM* data of gold spheres with diameters of 40 nm, 60 nm and 80 nm.

between the slides was closed with nail polish to avoid vaporization which would spoil the stability of the measurement. Spheres with a diameter of 60 nm and two kinds of rods with dimensions of 35 nm×78 nm and 50 nm×107 nm were investigated separately. The time trace of a particle spectrum was taken until the camera gathered ten thousand spectra. The standard deviation of the resonance wavelength of these spectra was used as spectral noise (see Figure 4.4a). From the quality plot in Figure 4.4b can be seen that there is a trade off between the spectral sensitivity, meaning the noise, and the temporal resolution of the measurement. To avoid errors in the read-out speed it was verified by an oscillator with the finding that camera software and oscillator value agreed perfectly.

Furthermore, intensity and *FWHM* measurements on gold spheres of different sizes have been carried out. The obtained data is shown in Figure 4.5 and reveals the expected trends of scattering intensity, retardation and damping. Additionally, I acquired data for 20 nm gold spheres. These particles are only barely visible in the ocular which makes it difficult to chose typical particles. Investigation of the resonance wavelength and the *FWHM* of the data taken suggested a bios in the particle selection as they had an average resonance wavelength of 555 nm and a *FWHM* of 122 nm which is much larger than expected. To avoid this systematic error an automated particle finding algorithm should be implemented.

Comparison to previous setups

To measure the scattering spectrum of a plasmonic nanoparticle it is necessary to inhibit the bright background normally obtained with microscopes. This can be achieved either with a dark field condensor or with TIR (for theory on TIR see Section 2.5). A dark field condensor forms the illumination light via an aperture or mirrors to a shallow cone with the sample positioned at its tip. The scattered light from the object can then enter the objective, whereas the illumination light travels with an angle too large to be captured by the objective. So far most dark field setups as well as TIR setups were equipped with halogen lamps. Such light sources provide much less intensity than the WLL used here. Therefore, even with optimal gain conditions, the minimum exposure time is in the 100 ms regime. Figure 4.6 shows a 60 nm sphere sample in direct comparison of a typical dark field setup and my Plasmon Fluctuation Setup with a WLL in TIR illumination.

Side remark: A recently published paper describes a setup for discriminating between 60 nm silver and 80 nm gold spheres with a detection time in the millisecond range. It is based on interferometric measurements on flowing particles and works with two discrete wavelengths and two corresponding photo diodes [122]. Even if they were to achieve same time as in my setup, an entire spectrum is not gathered.

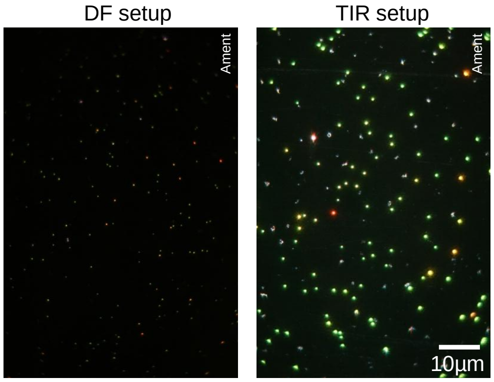

Figure 4.6: Comparison of the Plasmon Fluctuation Setup with a common dark field setup. Both pictures were taken with a 40x CP-Achromat air objective with the same camera settings of 1 s exposure time and ISO200. The same 60 nm sphere sample was used in both measurements as a standard.

4.3.1 Noise

The quality of a measurement is strongly influenced by the amount of noise present during the measurement. The possible noise terms existing in the Plasmon Fluctuation Setup are: laser noise and camera noises, namely shot noise and read noise (dark current noise can be neglected due to the thermoelectric cooling of the camera). To have an estimation of the importance of the different noise terms I investigated each term individually. Furthermore, this quantitative knowledge on different noises allows to simulate the scattering spectra to predict the quality of a measurement.

White light laser noise

The quality of the white light laser is a crucial factor for the performance of the setup. The laser noise was investigated by measuring ten thousand frames of white scattering silica beads at different exposure times covering 5 orders of magnitude. Calculations of the stability of various wavelengths resulted in noise levels of about 1.5 % for the millisecond regime and below 3 % for the microsecond regime. The larger noise at shorter exposure times does probably not originate from the laser, but can be attributed to the smaller number of detected photons. For these short exposure times no scattering particle provided enough photons to achieve a comparable count rate. Also, it can be noted that a noise level below 2 % is in good agreement with information from the supplier, even though it includes further noise sources like shot noise and read noise.

Camera noises

The **shot noise** is the square root of the number of counted photons and implemented in all simulations in such a manner.
The **read noise** was measured for several gain values by subtracting two dark pictures with minimum exposure time and extracting the standard deviation of the noise. As two pictures were used, the noise reduced further by the square root of two. The gain dependent read noise for 20 binned pixels was measured to be $\eta_{\text{read}}(\text{gain}) = 15.903 + 1.151 \cdot \text{gain} + 0.007 \cdot \text{gain}^2$.

4.3.2 Overall microscope collection efficiency

To have a reliable, predictive tool for the optimal choice of sensor particles, it is essential to simulate characteristics of the setup as well as just discussed, occurring noise terms. First of all, the overall microscope collection efficiency was deduced by comparing particle intensities measured and calculated. 25 spectra of 60 nm gold spheres were acquired and then their mean maximum intensity was compared to the maximum scattering intensity of the same particle calculated by QSA. For QSA parameters like the illumination density ($1\,\text{mW}/\lambda/\text{mm}^2$), exposure time (13 ms for 60 nm spheres, 103 ms for 40 nm spheres), bin size of the wavelength range (0.52 nm/pixel), and the refractive index of the surrounding medium (2/3 water, 1/3 glass) were adapted in the simulation to match the condition of the experiment. The transmission efficiency obtained is $(5.4 \pm 2.3)\,\%$. The error is calculated using the standard deviation of the intensity of all particles measured. As an additional control the measurement was repeated with 40 nm gold spheres resulting in a transmission efficiency of $(6.2 \pm 2.3)\,\%$.
A rough estimation of the expected overall microscope collection efficiency was done by simple multiplication of all including factors like objective collectivity (10 %, approximated by geometrical consideration of a NA 0.65 air objective), objective transmittance (∼90 %), spectrometer transmittance for the investigated order of the spectrum (∼50 %) and the quantum efficiency of the camera (55 % at 530 nm). By this I obtained an overall efficiency of 2.5 % from which I conclude the reasonability of the values obtained before.

4.3.3 Baseline stabilization

For reliable long term measurements of resonance wavelengths, a stable baseline is essential (see Figure 4.7). To achieve such a stable resonance position, several precautions have to be considered. It is necessary to exclude any external stress in the flow cell. Even lifting the outer ends of the tubing will cause changes in the resonance position. Therefore, it is advisable to measure in constant conditions like a constant flow or no flow at all. By occasionally flowing fluid, resonance changes via stress and temperature variation are probable to be introduced. Another crucial point is the positioning and focusing of the particle. The maximum

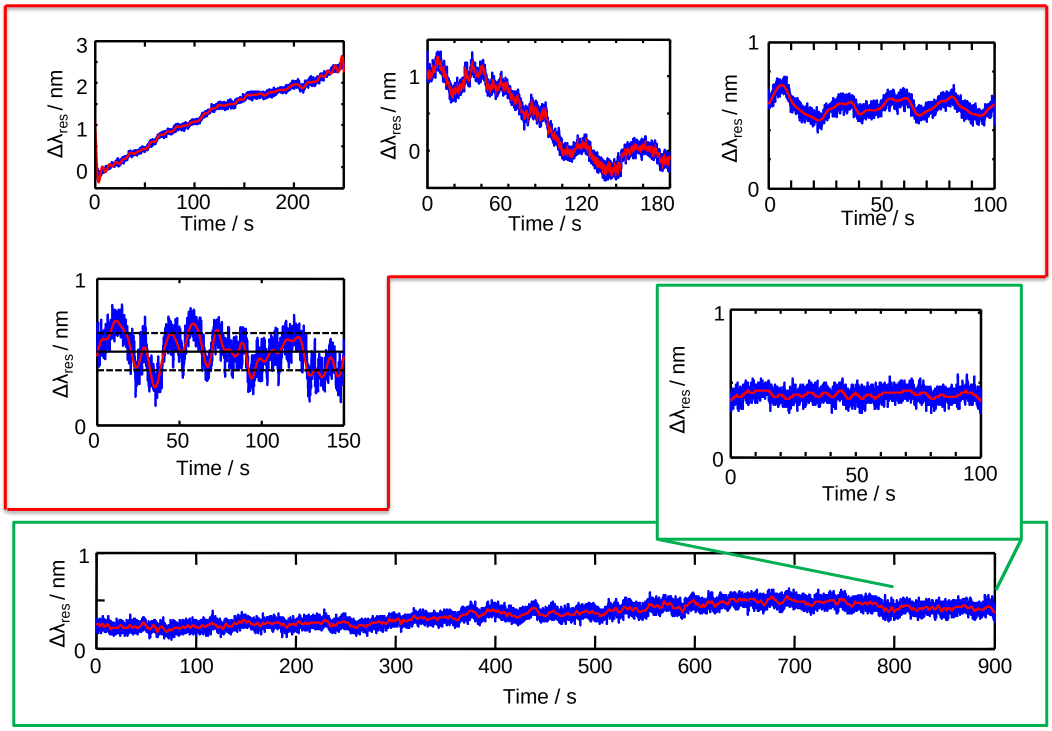

Figure 4.7: Basline stabilization is a crucial aspect for a good measurement. Artifacts seen before stabilization are shown in the red box and include strong red or blue shifts, random fluctuations or somehow periodic signal variations. A good baseline, as it should be established before measurement, is shown in the green box.

intensity has to be adjusted and maintained to provide optimal settings. Minor drifts of the sample stage during measurement will already introduce a shift in the resonance position [123]. Therefore, it is mandatory to not touch the entire optical table during an experimental run.

4.4 Conclusion

The crop mode in combination with the high gain of the EMCCD camera and a powerful supercontiuum white light source was able to improve the time resolution of acquiring plasmonic resonance spectra into the 50 µs regime. The spectral quality in the millisecond regime is at least of comparable quality to earlier generation dark field setups. This is an improvement of at least four orders of magnitude without loss in quality.

The length of a single time trace without disruption can be up to $4{\cdot}10^5$ frames. At an exposure time of 10 ms, giving a cycle time of 13.7 ms, this allows monitoring for 90 minutes. However, stability of the system is here the antagonist.

5 Single Unlabeled Molecule Sensing

In our days, if scientists want to detect single molecules they have to label the analyte with e.g. dyes for sufficient contrast. However, this labeling can induce conformational or property changes to the analyzed molecule. Therefore, finding a method to detect single, label free molecules is a very important task of today's research.

Prior to showing how I solved this challenge using a gold nanorod as sensor, I give a short introduction to the field of plasmonic nanoparticle using with a focus on sensing:
Plasmonic nanoparticles are used in many disciplines in our days. In cellular imaging or immunoassaies they serve as brightly colored labels. Additionally, in cancer therapy nanoparticles are used as heat sources to damage mutated cells. However, even more interesting is the qualification of plasmonic nanoparticles as sensors using their high sensitivity to their direct environment. During the last decades scientists have largely improved the quality of such plasmon particle sensors. The first method exploiting plasmons for sensing was the surface plasmon resonance instrument (SPR). The concept is based on a propagating surface plasmon in a thin gold film [124]. The advantage of using nanoparticles over SPR is the lower influence from bulk refractive index as the sensing distance above the metal is much smaller for nanoparticles [125, 126]. It has been shown recently that the extinction wavelength of an array of nanoparticles can be measured with a precision as low as $5 \cdot 10^{-4}\,\mathrm{nm}$ at a temporal resolution of 1 s [127]. With this method the calcium ion induced conformation change of the protein calmodulin was monitored [126]. This label free technique was also discovered by the pharmacy community as powerful tool for bioprocess studies [128]. The next logical step in plasmon sensing was then to move to single particle experiments. For a single nanoparticle the sensing volume is in the attoliter regime. The corresponding zeptomolar sensitivity was first shown in 2003 [129]. An improvement of the absolute detection limit was the implication [125]. Such a sensor is not simply the miniaturization of a SPR system, but holds information about fluctuations canceling out otherwise (see Section 5.2.5). Additionally, single nanoparticles can be used within living cells, whereas no fixed array of nanoparticles can penetrate them. Another advantage of single nanoparticles as sensor is the high spatial resolution provided by their small size. An interesting experiment based on single particle sensitivity monitors DNA cleavage in real-time and thus is a good example for the sensing capability of noble metal nanoparticles [130]. With a similar, but even more advanced, concept hydrogen sensing was demonstrated in the Alivisatos laboratories at a single particle level [131]. Further improvements down to single molecule sensitivity in living cells or extreme parallelization of biosensing is a realistic perspective in this field [132].

After this introduction I move on to recently published single particle measurements. I repeated these experiments during my thesis to learn about the quality of the measurements and now briefly report on the outcome.

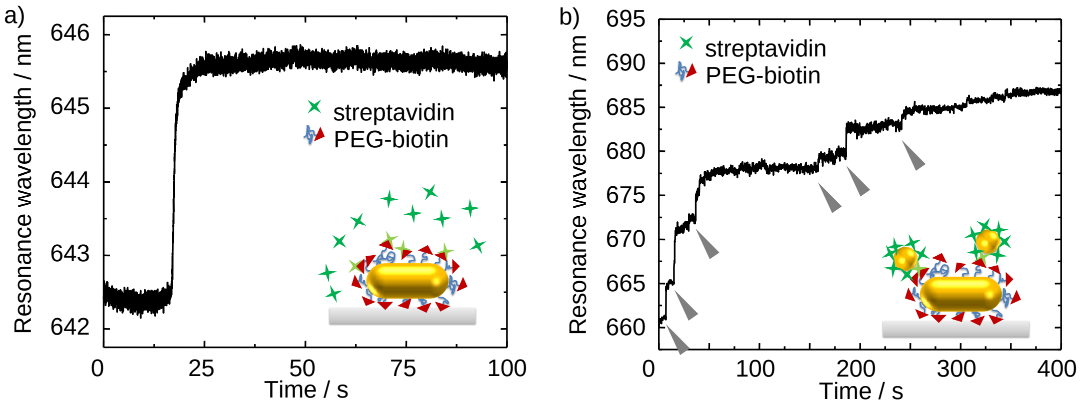

Figure 5.1: a) Full layer sensing of streptavidin on a PEG-biotin functionalized Au rod. b) 20 nm streptavidin functionalized Au spheres attach to a PEG-biotin functionalized Au rod. Attachment steps are indicated with gray arrows.

5.1 Different conformations sensed

5.1.1 Layer sensing

Already in 2003, specific biomolecular recognition based on single gold nanoparticle light scattering was reported by Raschke et al. [28]. They demonstrated a real-time streptavidin sensor based on the plasmon resonance shift of a single gold nanosphere with a sensitivity down to 1 µM streptavidin concentration. The possibility to improve this sensing method by the usage of other shapes besides spheres as sensor was shown in 2008 [133]. On year later, this system of binding proteins to its ligand which is attached to a nanoparticle was further improved by Nusz et al. [134]. They followed the scattering spectrum of a single biotin functionalized nanorod when incubated with streptavidin solution at a time resolution of 10 s. There, a concentration of streptavidin down to 1 nM could be detected. In this publication the advantage of a single particle experiment over ensemble averaging was already pointed out.

The specific recognition of a target molecule is a major requirement for a biosensor. It can be achieved by functionalization of the nanoparticle with a corresponding specific linker molecule. Nevertheless, a tremendous loss of sensitivity due to the reduced sensing volume has to be accepted.

To test the Plasmon Fluctuation Setup presented in this thesis I have carried out experiments of streptavidin binding specifically to a biotin functionalized nanorod with 3000 g/mol PEG as linker (see Figure 5.1a). The used streptavidin concentration was 1.9 µM. In contradiction to the experiments of Raschke et al. [28] who used a concentration of the same magnitude, I do not see a gradual shift over 15 min, but rather an instantaneous (∼1 s) binding.

5.1.2 Au sphere attachment

The next step in history to show the improvement of plasmon sensors was the detection of one to a few labeled molecules. One choice of labeling could be the attachment of a small plasmonic nanoparticle to the molecule of interest. Here, the signal enhances strongly by the plasmon coupling of sensor and label when approaching. However, as the nanoparticle label is larger then the common molecule, preparation is easier if the entire nanoparticle is functionalized with the target molecule. In addition, this increases the binding probability of the labeled system. The first demonstration of such single binding events was reported by Sannomiya et al. in 2008 [135]. As sensor they used a 100 nm Au spheres coated with DNA. The complementary target DNA was labeled with 20 nm Au spheres. The attachment was monitored in real-time. Afterwards the same particles were investigated in SEM to verify the number of attached 20 nm Au spheres.

A similar experiment was also carried out by me. I coated Au nanorods with 3000 g/mol PEG-biotin. After immobilization of the sensor with 1 M NaCl in the flow cell, the 20 nm Au spheres with matching streptavidin coating were flown in. Continuous measurement of the resonance wavelength of the sensor with a temporal resolution of 13 ms showed similar shifts to red wavelengths (see Figure 5.1b).

After being able to reproduce these recently published results, I moved to the holy grail of sensing - the detection of individual, unlabeled molecules. The challenges of this task and my achievements are presented in the next section.

5.2 Single unlabeled protein detection

Well established methods commonly used for single protein detection take advantage of labeling the proteins. A popular example is fluorescence correlation spectroscopy [136]. Another route uses an enzymatic reaction to amplify the signal to make it large enough for detection [137]. Here, an array of standing nanosize cylinders was functionalized to allow the specific binding of horseradish peroxidase. In an additional step these bound molecules catalyze a local precipitation reaction resulting in a further increase of the refractive index. As this refractive index change is proportional to the before bound enzyme molecules, an indirect detection of down to 40 pg/cm^2 is possible. This adsorbed mass corresponds to a single molecule bound per nanoparticle. The time resolved detection of single *unlabeled* molecule binding events would be of even higher interest.

Building sensors with the ultimate sensitivity of detecting unlabeled single molecules would not only be an impressive step in sensitivity but would further allow identification of adsorption and desorption dynamics, otherwise hidden in ensemble measurements. This detection of single unlabeled proteins binding to a surface is in our days the aim of a various number of methods. Very different approaches like optical microcavities (e.g. whispering gallery modes, WGM)

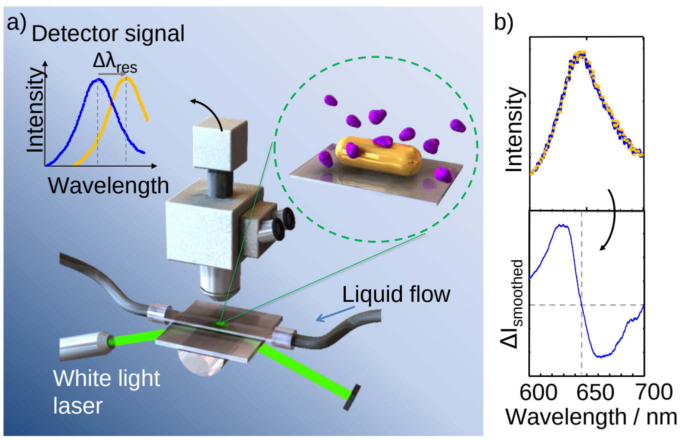

Figure 5.2: a) Illustration of total internal reflection setup with magnified view into the flow cell and optical read-out. b) Measured resonance spectrum of a single Au nanorod with an exposure time of 10 ms before and after single protein attachment and the difference between both. The 3D visualization of the microscope was done by

[138, 139] or surface-enhanced Raman scattering (SERS) [140] are followed. Also non optical routes using electric detection via carbon nanotube [141] or boron-doped silicon nanowire field-effect transistors [142] are taken. However, all of these methods suffer from one or another disadvantage such as difficult sensor fabrication, lacking capability of in vitro experiments, an expensive detection setup or simply a smaller sensitivity.

The idea of using even smaller sensors compared to WGM leads directly to plasmonic nanoparticles. So far this method did not yet reach the ultimate sensitivity as the signal-to-noise ratio with millisecond time resolution was not sufficient. To achieve this ultimate limit of single unlabeled molecule detection, literature proposes many routes to improve plasmon sensitivity. Particles with sharp tips or small interparticle distances give rise to hot spots increasing sensitivity [143]. Besides the choice of optimal size is discussed [144]. Furthermore, the lack of enough illumination intensity limits the sensitivity of today's setups. To my knowledge there was only one paper published until now where the detection of single desorption processes from a nanoparticle was achieved with huge mathematical effort [145]. In contrary, I demonstrate the detection single unlabeled molecule adsorption events by optimizing the sensitivity and time resolution of the setup as described in Chapter 4 (see Figure 5.2). Using a gold nanorod as sensor I see discrete steps in its plasmon wavelength caused by single adsorbing molecules. Therefore, I provide a new tool for label free single molecule detection.

5.2.1 Materials and methods

Before I present my results on single unlabeled protein detection I give a brief summary on materials and methods used.

Gold nanorods were grown in a two step wet chemical synthesis as described in Appendix A. Fibronectin from bovine plasma was purchased from Sigma (F1141-1 mg). Phosphate buffered saline (PBS) and sodium dodecyl sulfate (SDS) were bought from Sigma. PBS solution was filtered with a 20 nm pore size filter before usage. Different concentrations of protein solution were made by diluting fibronectin into PBS solution.

The Plasmon Fluctuation Setup described in Chapter 4 was used. The exposure time for medium rods was 10 ms with a cycle time of 13.7 ms. The gain was adjusted for maximum signal if needed, normally ranging between enabled gain and a gain value of five.

I used 'home-build' flow cells consisting of a glass capillary (2 mm × 0.1 mm) attached with glue to flexible tubing. Thus, a liquid exchange was easily possible. The refractive index between the flow cell and the glass surface illuminated by the white light laser was matched with immersion oil.

Gold nanorods with different dimensions were used in this experiment as sensors. They ranged from small (14 nm × 40 nm, $\lambda_{\text{ensemble}} = 674\,\text{nm}$) over medium (35 nm × 78 nm, $\lambda_{\text{ensemble}} = 635\,\text{nm}$) to large (50 nm × 107 nm, $\lambda_{\text{ensemble}} = 664\,\text{nm}$) rods. Particles were immobilized with 1 M NaCl in the flow cell. Upon inspection in the TIR microscope, they were all clearly visible to the eye. Differences appeared in the intensity as it scales with the particle volume. The sample was rinsed extensively before usage: first with pure water, afterwards with 10 mM PBS. Crucial to the quality of the experiment was the stability of the resonance wavelength. Stabilizing the wavelength normally took about an hour. This might have been due to stress inside the sample stage, drift in focus, or effects due to heating. When a stable resonance wavelength was achieved for several minutes the tubing of the flow cell was put into the protein solution and gravitational force generated the flow. At this time, the measurement was started and no further adjustments at the setup were carried out during measurement.

5.2.2 Time traces showing single protein attachment

In this section I provide data showing the attachment of single unlabeled proteins. Also I present the method introduced by me to identify single steps in the time trace of the resonance wavelength.

As analyte the macromolecule fibronectin was chosen to bind unspecific to the CTAB coated gold rod used as sensor. This system is well known from quartz crystal microbalance (QCM) and the protein is furthermore extensively discussed in literature [146, 147, 148]. To test the chosen system I investigated the binding of fibronectin molecules at different concentrations to gold rods. Therefore, nanoparticles were immobilized in a flow cell and stabilization of the resonance wavelength was allowed [123]. The spectral signal of a single nanoparticle was then monitored over time and the resonance wavelength, $\lambda_{\text{res}}(t)$, was obtained by fitting a parabola through the peak maximum of each frame. Flowing fibronectin into the flow cell reproduced adsorption curves as know from several experiments like SPR (see Figure 5.3a) [149]. To obtain the respective adsorption coefficients, k, the normalized shift of resonance wavelength, $\Delta\lambda_{\text{shift}}(t)/\Delta\lambda_{\text{max}}$, was fit with the exponential function $\Delta\lambda_{\text{shift}}(t)/\Delta\lambda_{\text{max}} = 1 - \exp(-ckt)$. For c the fibronectin concentrations used for each experiment was taken. The adsorption coefficient

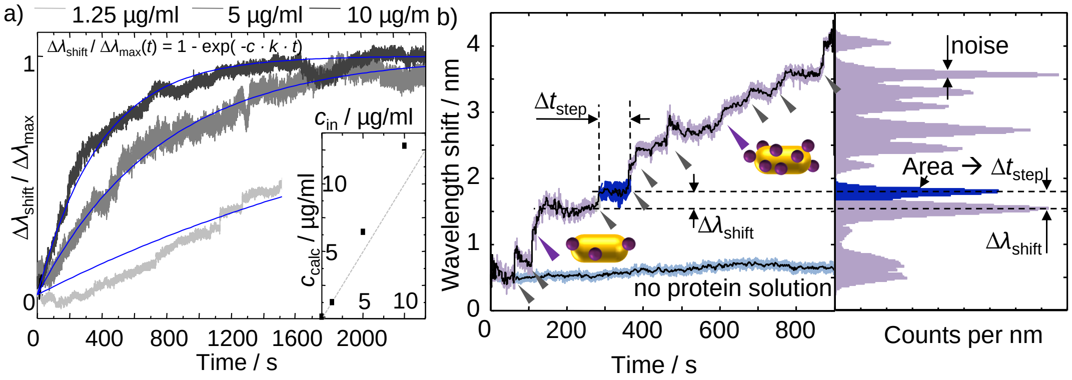

Figure 5.3: a) Adsorption curves of fibronectin at different concentrations on Au nanorods. The blue lines are fitted and give the following adsorption coefficients k: 2.80, 2.62, and 2.59 in$10^{-4}\frac{\mathrm{cm}^3}{\mathrm{s}\,\mu\mathrm{g}}$ respectively from lowest to highest concentration. The inset shows a comparison of the inserted concentrations to the concentrations calculated from the adsorption curves only using a literature value for the adsorption coefficient of fibronectin to gold [147]. The gray dashed line represents the ideal curve. b) Typical time trace (left) showing the resonance wavelength of a single Au nanorod during incubation with protein solution. The black curve shows the FFT denoised signal. The sketches illustrate the number of adsorbed proteins onto the sensing gold rod at this point in time. Histogram (right) of the same time trace showing distinct peaks for each step.

obtained is $k \approx 2.67 \cdot 10^{-4}\frac{\mathrm{cm}^3}{\mathrm{s}\,\mu\mathrm{g}}$ (fit accuracy $1.1 \cdot 10^{-7}\frac{\mathrm{cm}^3}{\mathrm{s}\,\mu\mathrm{g}}$) which is of the same magnitude as the adsorption coefficient $k = 1.014 \cdot 10^{-4}\frac{\mathrm{cm}^3}{\mathrm{s}\,\mu\mathrm{g}}$ taken from literature[12] [147]. The inset of Figure 5.3a shows a comparison of the concentrations inserted to the concentrations calculated from the adsorption curves fitted only using a literature value for the adsorption coefficient of fibronectin to gold.

The interesting new observation can be seen at low concentration of proteins. Real time tracking of a single particle resonance wavelength allowed to follow the adsorption of one molecule at a time. Discrete jumps in the resonance wavelength can be seen in the time trace (see Figure 5.3b). Interesting parameters are the shift, $\Delta\lambda_{\mathrm{shift}}$, caused by a single attaching molecule as well as the average time, Δt_{step}, passing between the steps. Notice, as surface saturation approaches this time interval between adsorption events becomes longer. The optimal concentration for the detection of single steps was 1.25 µg/ml.

To analyze the time traces several ways were tested: i) Sliding average of the standard deviation, where steps occur as increase in the value of the local standard deviation. ii) Sorting the time trace with a cumulative probability allows to find points of inflection as distinct attached protein numbers. iii) Investigation of a histogram of the measured resonance wavelengths where Gaussian peaks appear for each number of attached proteins. Despite finding comparable results for all methods presented here, the easiest analysis of a time trace measured is to

---

[12] The adsorption coefficient in the publication is given in the unit cm/s, which can be converted to the unit used here $\frac{\mathrm{cm}^3}{\mathrm{s}\,\mu\mathrm{g}}$ by multiplication of $\frac{a}{m}$. Foot print area $a = 11 \cdot 10^{-14}\,\mathrm{cm}^2$, dry mass of single protein $m = 7.5 \cdot 10^{-13}\,\mu\mathrm{g}$.

investigate the histogram of the resonance wavelengths measured as shown in Figure 5.3b. Thus, the information contained and its read-out in more detail: The histogram shows several Gaussian peaks where each peak corresponds to a certain number of molecules attached. The maxima are separated by $\Delta\lambda_{\text{shift}}$. The area under the Gaussian peak tells the time Δt_{step} this certain configuration was held. The fact that we do not see discrete delta functions clearly separated from each other is due to the noise of the system. Even a 'naked' rod measured in pure water shows this Gaussian distribution with the $FWHM$ being the noise of the setup.

5.2.3 Control experiments

Even though discrete steps were found in the resonance wavelength of sensing nanoparticles over time, no proof for the actual adsorption of single molecules was given so far. Here, I present a number of control experiments to confirm the hypothesis of single molecule adsorption events: The time between events varies systematic with protein concentration. The shift induced is smaller for smaller proteins. Proteins can be desorbed again. And the full coverage shift matches statistical data.

Proofs for single molecule events

One strong indicator was the fact that the time between steps varies systematically with concentration and fits with calculated diffusion limited adsorption processes. In more detail, the number of protein hits on an area is described by $N \cong cA\sqrt{Dt}$, here c is the protein concentration, A the available surface area of the rod, D the diffusion constant as described in Equation 8.2 and t the observation time [150]. As this equation is only valid for the first few adsorbing molecules[13], I only took the first five events for determination of the attachment frequency into account. Thus, the time of the measurement varied with concentration. The number of attachment events calculated, using good approximations for the values of c, A and D and experimental data are presented in Figure 5.4a. The number of events calculated and measured agrees astonishingly well, even though no probability of adsorption was introduced.

The second strong hint for the observation of single molecule events was the dependence of the step size, $\Delta\lambda_{\text{step}}$, on the size of the protein. As expected, smaller proteins show a smaller shift (see Figure 5.4b). This was tested by cutting the fibronectin dimer into monomers by addition of 5 mM tris(2-carboxyethyl)phosphine (TCEP, Sigma). After 5 min of incubation, the solution was ready to use and handled with the same procedure as the dimer molecule. Notice, at this molecule size the detection limit was reached, thus, selection of single events became difficult. Also I want to point out the fact that not all shifts are of similar height. This

---

[13] Afterwards, the amount of the particle surface already occupied has to be taken into account.

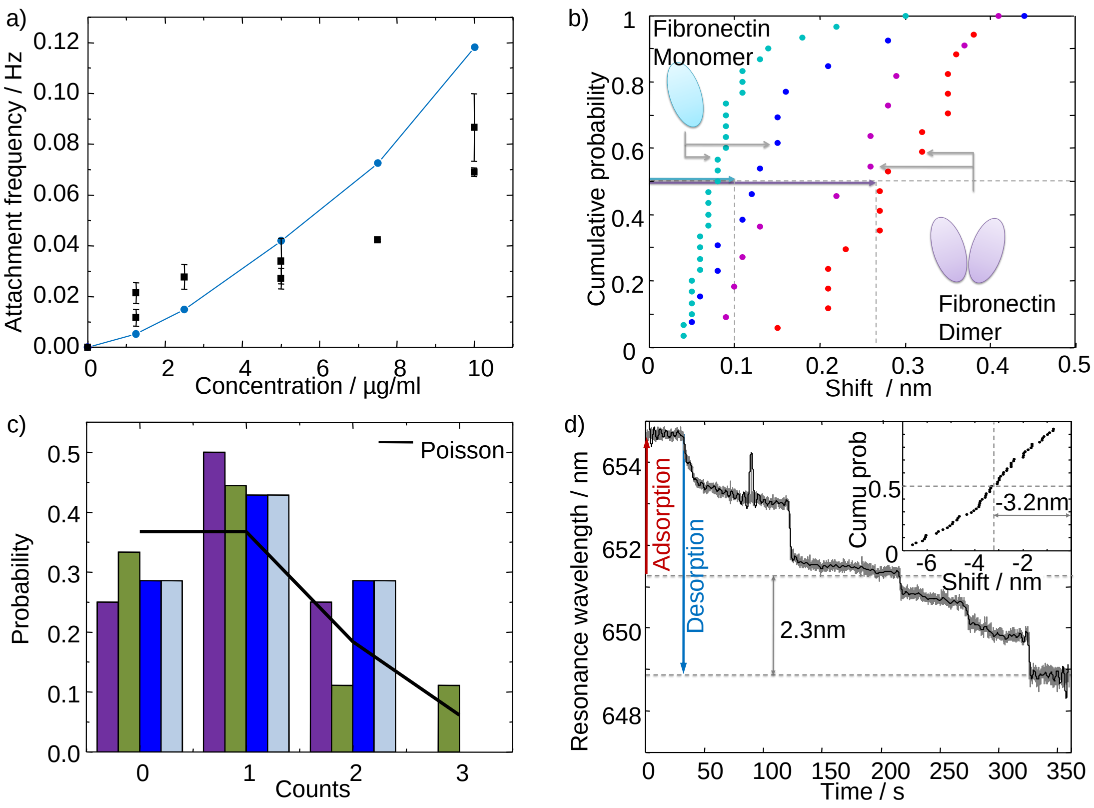

Figure 5.4: a) Influence of fibronectin concentration on attachment frequency. Measured data is plotted in black. Theoretical data is plotted in blue. b) Cumulative probability of the shifts caused by attachment of differently sized proteins. c) Comparison of the arriving times of the protein attachment to the expected uncorrelated event distribution given by a Poissonian. d) Protein desorption in the presence of SDS. The final resonance wavelength is blue shifted compared to the resonance position of the rod before adsorption. The inset shows a statistic of blue shifts caused by SDS after 20 min.

effect is due to the different binding positions on the rod and is discussed in detail in Section 5.2.4 'Boundary element method'.

A typical measure to check if single, uncorrelated events take place is the statistical investigation of the arriving times. If a Poisson distribution is found, evidence for single, uncorrelated events is given. Therefore, the arriving time of the proteins, defined as the time between events, was checked against a Poisson distribution. The entire trace was therefore divided into bins defined by the mean arriving time. Counting the number of events within each bin gave the statistics shown in Figure 5.4c. Checking the distribution measured with a χ^2-test supported the hypothesis with a confidence level larger than 95%.

Additional control experiments

As an additional validation of the single protein adsorption experiment, I measured the desorption of the proteins caused by washing with 0.2 wt% sodium do-

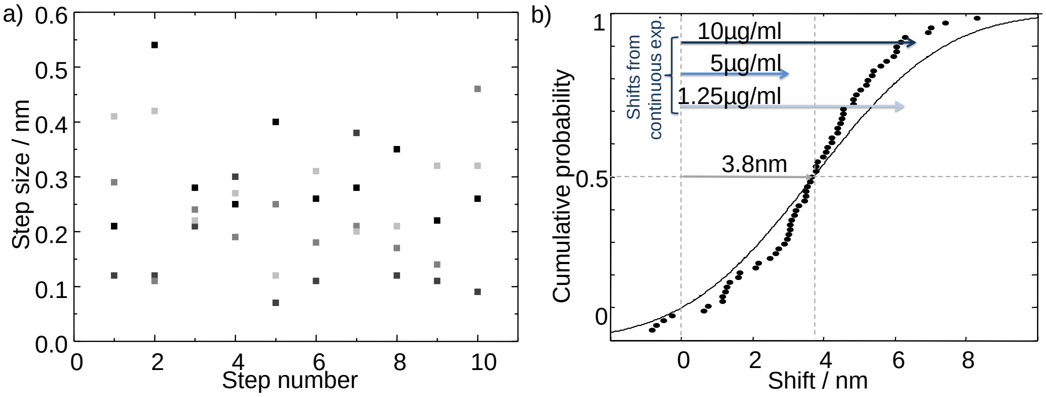

Figure 5.5: a) Step size plotted over the number of the respective attachment to control for systematics. b) Statistic of the full coverage shift of gold nanorods incubated with fibronectin and the final shift observed during continuous data acquisition.

decyl sulfate (SDS, Sigma). Figure 5.4d shows a typical desorption curve. Notice that desorption steps were bigger compared to the adsorption steps and less in number. This hints to the detachment of several proteins at a time. Also the final resonance wavelength of the sensing particle was blue shifted compared to the starting value. This finding was confirmed in a statistical experiment (see inset of Figure 5.4d) carried out at the setup described in Appendix C.1. Two reasons were taken into account for this blue shift. First, the initial gold nanorod was covered by a stabilizing CTAB double layer which was later replaced by the protein and was not restored after protein desorption. Second, SDS is known to induce charges which can also shift the resonance position of a plasmonic nanoparticle [21]. As a control experiment a CTAB coated nanorod was washed with SDS and afterwards exposed to 50 mM CTAB solution or 1 M NaCl solution. In both cases a red shift could be observed, and the hypothesis holds.

I also wondered whether a time dependence can be found in the step height as surface coverage increases. Plotting the step heights of four different time traces in the order of their appearance, no time dependence could be observed - as expected for random attachment (see Figure 5.5a). This finding of history independence is in good agreement to simulations carried out in the next section which also confirm that a protein attaching at a certain position induces the same shift independent from already attached proteins.

Another interesting parameter is the maximum shift, $\Delta\lambda_{\mathrm{max}}$, achieved under full protein coverage of the particle. It contains information about the absolute number of adsorbed proteins. To get inside if full protein coverage was already reached when measuring the adsorption curve (data see Figure 5.3), I compared the maximum shift to values measured at the fastSPS setup (setup described in Appendix C.1) providing statistical data as the shift of a high number of particles can be gathered from one experiment. The data showed good agreement in the shift finally reached (see Figure 5.5b). However, as the particles differ in size and arrangement of the protein coverage the deviation measured in absolute shift is

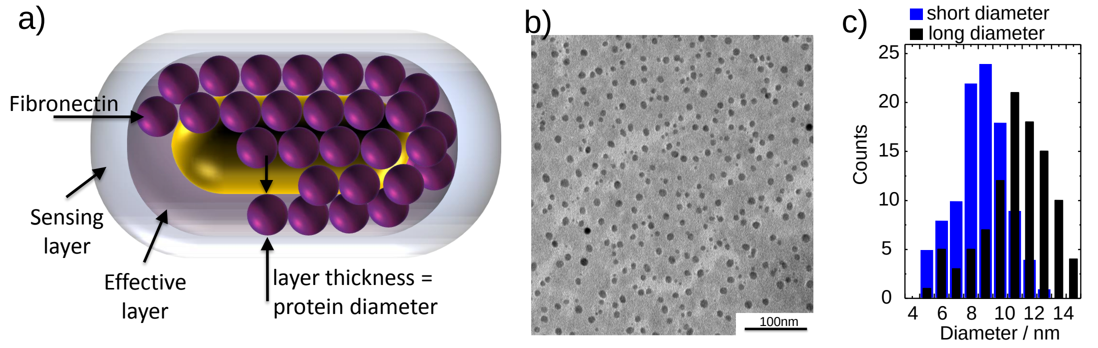

Figure 5.6: a) Parameters for QSA calculation to determine Fibronectin shift. The calculated layer around the gold particle has the same thickness as the diameter of the protein. Notice, the sensing layer will differ in distance for almost all cases. The total number of adsorbed molecules is calculated via the surface of the gold rod and the foot print area of a protein. b) TEM image of stained fibronectin molecules. c) Statistics of the measured dimension. In the case of egg shaped molecules short and long axis are chosen.

expected. Additionally, it should be mentioned that Langmuir adsorption predicts a larger surface coverage for surfaces exposed to higher concentrations. This effect is ignored here as it is masked by the polydispersity of the sample.

5.2.4 Simulation of expected shifts

In addition to the experiments the shift expected per adsorbed molecule was simulated. Therefore, two kinds of theoretical approaches were used with the finding that the size of the steps measured matches well to the sizes calculated.

Quasi-static approximation

The resonance wavelength of a naked gold nanorod and the same nanorod with full protein layer were calculated. To account for the spherical shape of the proteins the refractive index of the layer was adapted to an effective refractive index. Thus, the refractive index of the protein ($n_{\mathrm{protein}} = 1.5$) [28] and the refractive index of the solvent ($n_{\mathrm{solvent}} = 1.33$) as well as the volume occupancy of 60 % (for a layer of spheres compared to the fully filled layer) were accounted. Merging these parameters introduced an effective refractive index for the layer of $n_{\mathrm{eff\_layer}} = 1.432$. The layer thickness used was taken from the molecule diameter of 12 nm found in literature [151]. This value is in agreement with the dimensions we obtained by transmission electron microscopy experiments on stained fibronectin molecules (see Figure 5.6). For simplicity the fibronectin dimension was recalculated to match a hard sphere. The shift thus obtained was divided by the maximum number of attaching molecules, where a molecule was again assumed as a hard sphere with the attachment area of its shadow. This shadow, also called foot print area, is in good agreement with values from literature [152]. Results calculated with

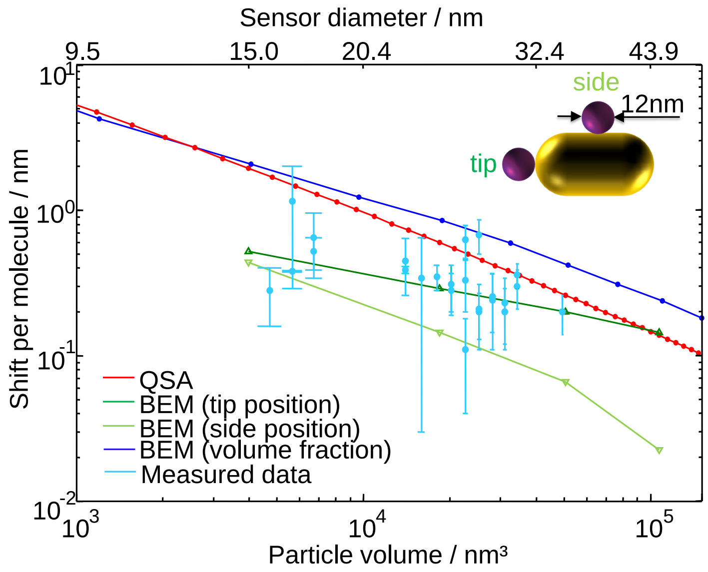

Figure 5.7: Comparison of theoretical and experimental shifts induced by single protein binding events. The red curve corresponds to QSA calculations where the full layer shift was divided by the number of attached molecules. The green curves are pure BEM simulation with side (light green) and tip (dark green) attachment. The dark blue curve results from BEM simulations including volume fraction. Measured data points are included in the graph in light blue. The particle volume was estimated from the scattering intensity and the resonance position of the particle. The error bar is the standard deviation of all measured steps seen within the time trace of a particle.

this method of the shift induced by the attachment of a single fibronectin molecule are shown in Figure 5.7 for several particle volumes.

Boundary element method

The advantage of BEM compared to QSA is the more exact description of the experimental condition. Not a full layer has to be simulated as in QSA, but the shift between a naked nanorod and a nanorod with an attached protein can directly be investigated. Thus, the protein position can be varied. This gives insight into the dependency of the expected shift on the attachment position (see Figure 5.8b inset). Positions at the side and close to the tip (10° offset) of the rod give the minimum and maximum shift,

Sketch	Protein nb	Shift / nm
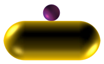	1.	0.073
	1.	0.171
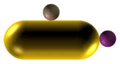	2.	0.171
	2.	0.176
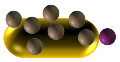	8.	0.171

Table 5.1: Influence of attachment position on the induced shift and its independence from number of attached proteins. Dimensions of the sensing rod: 25 nm × 70 nm. The new protein is shown in purple.

respectively. Furthermore, simulations to investigate the role of the number of proteins already attached were accomplished with the finding that the position of the attachment is of much bigger influence than the percentage of surface coverage (see Table 5.1). The BEM simulations presented here were carried out by .

As BEM needs a lot of simulation time a simplified method was introduced by . Here, not all analyte dimensions had to be simulated independently but were included via the sensing volume they occupy. The equation to calculate the final shift is defined by: $\Delta\lambda_{\text{prot}} = V_{\text{frac}} \cdot S \cdot \Delta n$. To independently derive the parameters included, first, the sensing volume, namely the volume which shows 1/e of the total shift, was calculated by BEM[14]. Therefrom, the volume fraction, V_{frac}, the sensing volume occupied by an analyte, was derived and multiplied with the particle sensitivity, $S = \Delta\lambda/\Delta n$. Last, the refractive index change, Δn, introduced by the attaching molecule was included. The shifts obtained agree well with the values of the carried out simulations (see Figure 5.7).

Optimal rod for single protein sensing

As a further subject, I addressed the question of the optimal rod sample for such single adsorption experiments. A large particle volume gives rise to an intense plasmon peak which can be nicely detected with low noise. The trade off of a large particle volume is the small shift induced by single protein binding (see Figure 5.8b). Decreasing the particle volume increases the uncertainty of the resonance position but in parallel increases the shift. In Figure 5.8c the two antagonists, signal and noise, are plotted. Only in the region shaded gray a signal-to-noise ratio above one is available. Also included in this sub figure are the different noise terms of the setup as discussed in Section 4.3.1. Figure 5.8d illustrates the shift induced per molecule for two rods (*AR* 2.25, *diameter* 20 nm and 35 nm). The total noise for a particular rod is constant and plotted respectively as vertical line. All molecules right of the intersection of shift and noise have a signal-to-noise level above one. Thus, for both rods single analyte molecules with a diameter bigger than 6 nm can be detected. Simulation shows that an increase of the laser power until a particle heating of 1 K is reached lowers the noise term (see Section 2.4). This higher illumination power allows, with the 20 nm diameter rod as sensor, the detection of molecules down to approximately 3.8 nm in diameter.

---

[14] For proteins with a diameter larger than the sensing distance this underestimates the resonance shift as the 1/e threshold is exceeded.

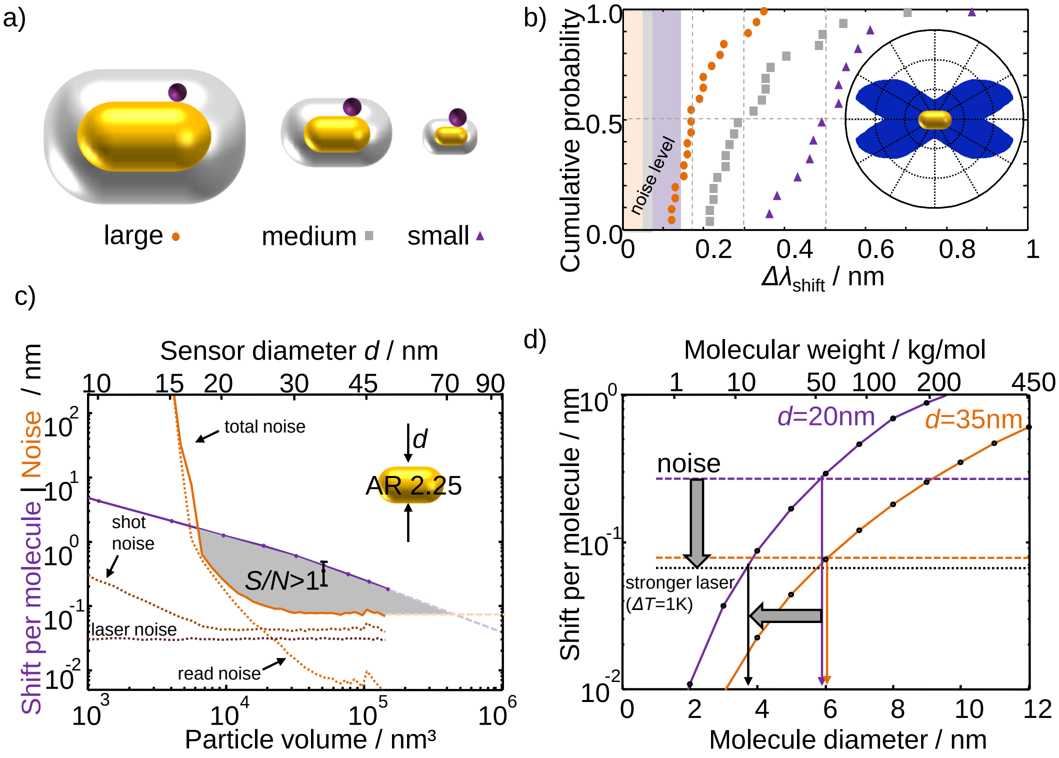

Figure 5.8: a) Change of sensing volume with particle size. Constant analyte size implicates variation in occupied volume fraction. b) Cumulative probability of measured resonance shifts within one trace for three differently sized particles. Average shifts are 0.17 nm for the large rod (orange ellipse), 0.30 nm for the medium rod (gray rectangle), and 0.51 nm for the small rod (purple triangle). The respective noise level is shaded on the left hand side. The large shift tail in the cumulative distribution is caused by the position dependent sensitivity along the rod (the inset shows a simulation for a 12 nm diameter protein on a 35 nm wide nanorod.) c) Simulated shift induced by a 12 nm diameter adsorbing protein (purple) compared to the noise level of our setup (solid orange). In the gray area, the signal-to-noise level is above one. The data point for 35 nm rods is the average shift per molecule as measured experimentally. d) Induced shift for two rod sizes if analyte size is varied. Vertical lines give respective noise value minimizing smallest detectable molecule. For optimal laser power, limited by sensor heating of 1K, analytes of 3.8 nm are detectable with 20 nm diameter rods. The aspect ratio of the nanorods is always 2.25.

5.2.5 Conclusions and future potential

I was able to show the step-wise adsorption of single proteins onto a plasmonic nanosensor. In addition, I explored the dimensions for possible sensors by simulation, finding the optimal sensor for my experimental conditions. For further experiments I propose a setup which is able to measure in the near-infrared, as sensitivity of rods scattering in this regime is superior to rods scattering in lower wavelength regimes (see Figure 5.9). Also I determined the noise of the white light laser to be one of the main noise sources besides shot noise. Thus, including white light calibration for each single point in time would further improve the quality of the spectral resolution.

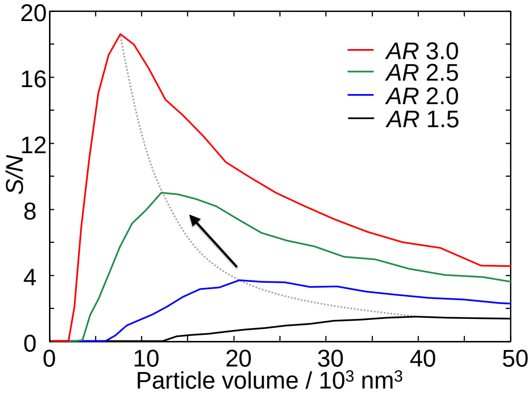

Figure 5.9: Signal-to-noise of single protein adsorption events for different aspect ratios of the sensing nanorod.

5.3 Time resolved binding kinetics and equilibrium fluctuations

Being able to resolve single protein binding, I tried to time-resolve the adsorption process itself – an information fundamentally hidden in ensemble measurements as the huge number of involved molecules attach at any point in time. For this, I manually superimposed and averaged all steps identified with nicely distinguishable starting points of the adsorption experiment carried out earlier within one measurement. Then, exponential adsorption dynamics could be resolved with millisecond resolution (see Figure 5.10a). A plasmonic red shift was observed during the adsorption process with about 1-2 s timescale. I believe that this slow red shift within one adsorption event came from a slow denaturation of the protein on the surface bringing it closer to the particle (see inset of Figure 5.10a). Such denaturing of proteins near metal surfaces is, by itself, a well known phenomenon [148, 153, 154]. My method allows now to study the temporal evolution of this process in detail and should trigger the development of models to explain the denaturing timescale observed.

Furthermore, I present a new method for the investigation of equilibrium dynamics. This new approach is based on the small sensing volume of a nanorod, thus, only few molecules can attach [129, 125] and coverage fluctuations can theoretically be used to retrieve information about binding kinetics. In Figure 5.10b I present the respective data. On the left, plasmon fluctuations measured in pure water are shown. The here seen fluctuations of 0.04 nm are simple setup noise. Whereas, looking at the plasmon fluctuations of the same system in a protein surfactant mixture in buffer conditions (right side) reveals much more structure and change in resonance position. This can be attributed to an equilibrium ad-

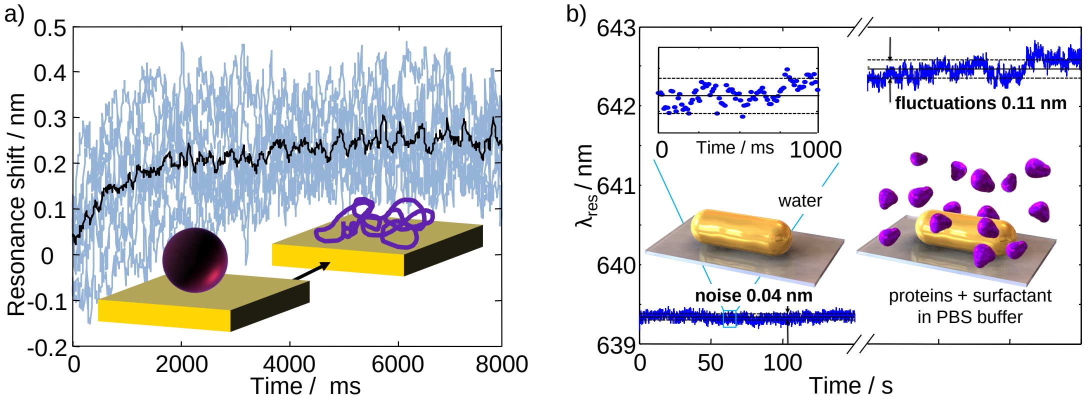

Figure 5.10: a) Mean adsorption behavior (black) averaged from 8 single adsorption events (blue) taken from a single rod. The deviation from a step-like form suggests a protein denaturing on the timescale of 1-2 s (inset) b) Compared to the noise level of 0.04 nm (standard deviation) in pure water, the fluctuation amplitude increases significantly to 0.11 nm in a protein surfactant mixture (25 µg/ml fibronectin, 0.2wt% SDS) due to equilibrium protein coverage fluctuations.

sorption and desorption of the proteins present. Therefore, a first step towards easy binding constant identification was done [155].

Outlook

Adsorption dynamics

For better understanding of the seen exponential adsorption behavior, further studies on parameter series of e.g. temperature, ion concentration, or similar have to be carried out. Also additional experiments with different proteins or the same, but slightly modified protein are of high interest as they might reveal responsible binding regions or importance of certain folding configurations.

Equilibrium and non-equilibrium experiments

Excessive studies with large sets of parameters influencing the process need to be carried out to understand and control coverage fluctuations in a projecting manner.

A potential candidate for equilibrium and non-equilibrium experiments on a system with biological relevance might be Annexin A1. This protein has a dimension of ~4 nm×7 nm×4.5 nm and a molar weight of 30-40 g/mol [156, 157]. Several kinetic studies on large ensembles have been reported in literature [157, 158, 159]. Therefore, its calcium dependent binding constant and the irreversible attachment to POPS-membranes (1-palmitoyl-2-oleoyl-sn-glycero-3-phosphoserine) is well known. QSA calculations, as described in Section 5.2.4, but with an additional membrane functionalization predict shifts by single protein binding in the order of 0.027 nm for a 20 nm×40 nm gold rod. At the current point in time this value is hidden in the noise level of the the Plasmon Fluctuation Setup. However, for infrared rods with an aspect ratio of 5 and a diameter of 10 nm this shift increases to

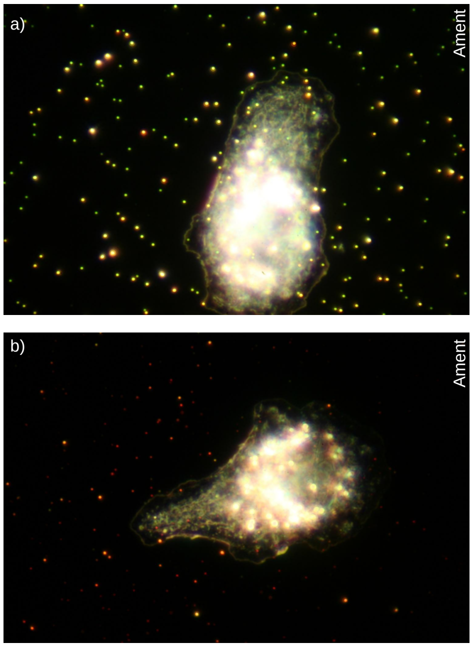

Figure 5.11: Ocular view of cells on top of immobilized nanoparticles. In a) spherical gold nanoparticles are shown. In b) gold nanorods are used. To determine the fluctuations of a living cell membrane the resonance spectrum of a nanorod underneath a cell has to be investigated. The difficulty introduced by the strong scattering of the cell nucleus is clearly visible.

0.11 nm. In combination with the improved signal-to-noise level in the infrared regime this adsorption event should be detectable.

Another interesting biological question aims for the fluctuations of a biological cell membrane. Changes in living cell membranes might give information about vitality, state of attachment or movements currently carried out. The challenge in the case of an eukaryote cell is the shielding of the light scattered by the nucleus (see Figure 5.11). Furthermore, the microscope has to be equipped with a temperature and a CO_2 control to ensure cell viability.

6 Nanodimers under Strong Illumination

Recently, the ’nanoruler’ a distance sensitive system of two close by nanospheres was introduced to measure distances on the nanoscale without bleaching or blinking as experienced for the commonly used distance sensor, fluorescence resonance energy transfer (FRET) [160]. However, so far no investigations were carried out on the behavior of this nanoruler under strong illumination. As such a strong illumination is present in the Plasmon Fluctuation Setup these studies are completed in this Chapter.

The system in focus consists of two connected spheres, also referred to as dimer, and is sensitive to the distance between the spheres as their plasmons couple (see Section 2.3). One main feature of dimers is the ability to measure nanoscale distances in real time. Thus, they are also called nanorulers. Experimentally, time dynamics of such coupled nanoparticles were first observed by Sönnichsen et al. [161]. In 2007, Reinhard et al. used this distance sensor to monitor the bending and cleavage of a DNA strand by an enzyme [162]. Besides this distance sensitivity, a second interesting characteristic of the nanoruler is the availability of the dimer orientation. This additional information can be gathered if measurements are performed with a linear analyzer in the detection beam. These features were exploited in one recent, fascinating experiment using silver dimers connected via a polymer bridge as a sensor for translational and rotational motion on a cell membrane [163]. Further ideas introducing nanoparticle DNA-dimers as building blocks for molecular electronics can be found in the literature [164].

To be able to use these dimers as distance, orientation or stiffness (see Chapter 7) sensor in the Plasmon Fluctuation Setup, it is necessary to check if changes are introduced by the strong illumination of the setup. As major concern, especially the presence of optical forces and heating effects due to light absorption have to be investigated.

Within this chapter, first, I describe the procedure of dimer creation and the arising interparticle gap. Then, the findings of the experimental studies follow, showing that strong illumination induces a collapse of the interparticle gap. Nevertheless, different experiments carried out imply different mechanisms for the approach of the two spheres. Also the theoretical investigation of the two possible mechanisms, heating and optical forces, did not pinpoint either of them as exclusive origin.

6.1 Functionalization and preparation

A common method to produce spatially well defined nanostructures is lithography [165]. Such structures, however, do not have flexible distances nor orientations that can be monitored in time. Therefore, I assembled the dimers directly in the flow cell via ligand receptor recognition. The advantage of a flow cell assembly over in batch prepared dimers is the observation of the assembly in time. Thus, the reduction of misinterpreted trimers or higher aggregates which are also created as the assembly is a stochastic process is achieved.

Functionalization

As linker I used the well known streptavidin-biotin system. The specificity of the interaction, the high affinity, and the stability of the biomolecules make this system a popular choice [166]. Polyethylene glycol (PEG) acts as an additional spacer. This polymer was chosen as it is water soluble and commercially available with different end-groups. Here, chains with a thiol as one end-group for covalent binding on gold, and biotin for the other end-group for specific streptavidin recognition were selected. The shortest PEG spacer used was bought with an amino-group which was altered with 3,3'-dithiobis(sulfosuccinimidylpropionate) (DTSSP) to provide a thiol group. Also streptavidin was attached to DTSSP to provide a gold binding thiol group. The functionalization protocol was kindly provided by and can be found in Appendix B.1 [167].

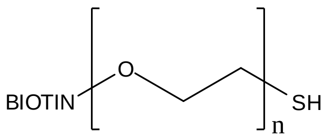

Figure 6.1: Biotin-PEG-SH structure

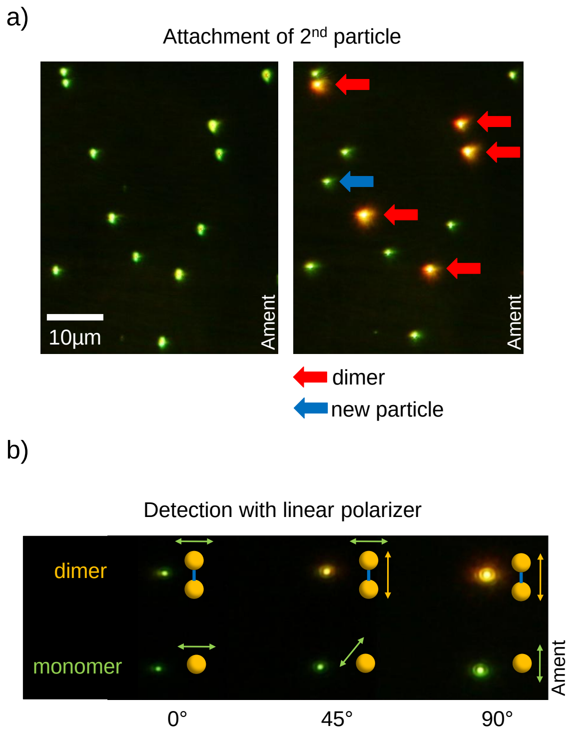

Figure 6.2: a) In the left image, the first introduced monomers are shown. After flowing the secondary particles into the flow cell, some green spots change their color to orange, a good indication for dimerization (red arrows). In addition, one new particle attached to the glass surface (blue arrow). b) The polarization dependent color difference between a dimer and a monomer is shown. In the case of a dimer the color changes when changing the polarization angle. In contrast, the monomer exhibits no color change. The change in intensity of the monomer is due to the illumination method.

Figure 6.3: Dimer spectra with linear analyzer at different rotational positions. The 60° (yellow) and 150° (dark blue) orientation correspond to the perpendicular and parallel illumination of the dimer. The weak existence of the short axis resonance peak cannot be repressed under any condition and is a strong sign for unequally sized nanospheres [56].

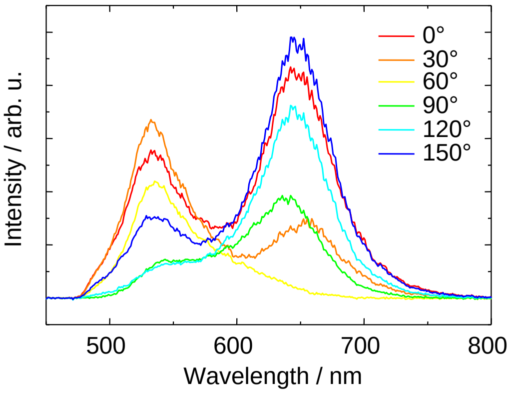

Preparation of dimers in the flow cell

After washing the flow cell intensively with Millipore water, a diluted (1:100 with deionized water) stock solution of PEG-biotin spheres was flown into the flow cell. Particles were immobilized with 1 M NaCl which was flown in as soon as the first particles reached the field of view (normally after $\sim$ 30s). After immobilizing a sufficient number of monomers, the flow cell was washed for at least 10 min to avoid later aggregation of floating particles. Additionally, passivation of the surface was done with a previously prepared passivation mixture (see Appendix B.1.3) by carrying out two cycles consisting of 10 min flow followed by 20 min incubation. The afterwards introduced stock solution of secondary, streptavidin functionalized particles was 1:100 diluted in passivation mixture to assure surface passivation after liquid exchange. Dimerization could then be followed in the microscope in real time. After a sufficient number of dimerization events, which normally took place after 5 min, the flow cell was again washed with the passivation mixture to remove unbound particles. Even though trimerization is suppressed by steric hindrance, it is straight forward to stop dimerization already as soon as approximately 50 % of the monomers experience a red shift. The statistical chance for trimers is then approximately 10 %. To avoid observing possible trimers or aggregates introduced later, preselection was carried out. Only particles which had been green monomers experiencing a reasonable red shift after incubation with secondary particles were taken into consideration (see Figure 6.2a). Furthermore, investigation with a polarizer to check if the two polarization axes corresponding to the long and short dimer axis, respectively, were present, was carried out prior to any measurement (see Figure 6.2b). When turning the polarizer the resonances of the two particle axes had to alternately appear as shown in Figure 6.3. The presence of the short axes peak at all polarization orientations originates most likely from the geometric alignment of the dimer in respect to the objective. More precisely, if both spheres appear on top of each other, no polarization dependence is expected. Note, in this configuration the existence of the long axis peak arises from the NA of the objective. Another mechanism predicting the polarization independent presence of both peaks is an inhomogenity in size of the two connected nanospheres and

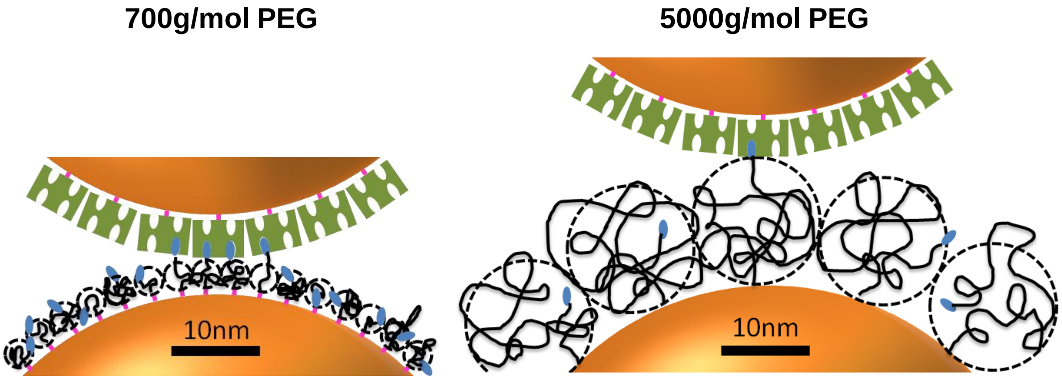

Figure 6.4: Relative scale of two dimers with different spacer lengths (700 g/mol PEG and 5000 g/mol PEG). The Au spheres are sketched in orange. Streptavidin is the green component, biotin is labeled in blue. The PEG chain is marked in black including the Flory diameter (dashed line). The very small DTSSP molecule used to attach the 700 g/mol PEG to the gold surface is imaged in pink.

corresponds to the antisymmetric bounding modes (see Section 2.3) which are repressed for homogeneous particle sizes [56].

Now that I explained particle functionalization and preparation I turn to the size of the interparticle gap. As discussed in Section 2.3 the resonance wavelength of the system strongly depends on this parameter.

6.2 Approximation of dimer gap distance

In this thesis, the approximation of the gap distance between the two spheres of a dimer is only investigated by literature stated values. Therefore, dimensions of all interparticle molecules (streptavidin, PEG-biotin and DTSSP) are summed up to determine the final gap distance. More detailed work including further investigation methods like cryo-TEM and dynamic light scattering (DLS) was carried out by on the same system [167].

The dimensions of streptavidin are given in literature to approximately 4.2 nm×4.2 nm×5.6 nm [168]. The streptavidin binding biotin is much smaller in dimension: approx. 0.52 nm×1.0 nm×2.1 nm [169]. As biotin binds in a pocket of streptavidin its dimension is neglected. Another small molecule is DTSSP with a maximum dimension of 0.6 nm. Besides streptavidin, the main contributor to the gap distance is the coiled PEG spacer. In a good solvent, its dimension can be determined by the Flory

M_W PEG / g/mol	monomers	gap distance / nm
700	10	≈ 8.2
3000	62	≈ 13.7
5000	107	≈ 17.0

Table 6.1: Approximated dimer gap distance induced by different spacer lengths

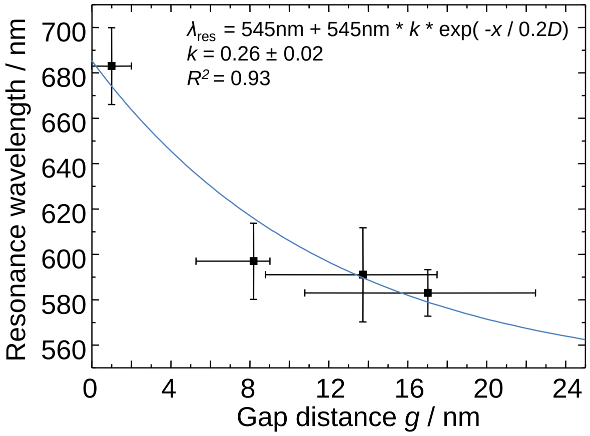

Figure 6.5: Dependency of the dimer resonance position on the gap distance. Data points measured (black) are fitted with the universal scaling law from Jain et al. (blue) [50]. The standard deviation of all respective measurements is used for the error bars in the resonance wavelength. The minimum and maximum gap distance for each data point is taken from other approximations of the radius of gyration of PEG [170, 171]. The data point and its error at 1 nm gap is an assumption from the resonance position.

radius $R_F = aN^{0.6}$, where $a = 3.5\,\text{Å}$ is the size of a PEG monomer and N the number of monomers[15] [172]. The number of monomers is calculated from the molecular mass of the PEG molecule. As the structure of a PEG monomer is $[(CH_2)_2O]$ the molecular weight calculates to 44 g/mol. Before dividing the molecular weight of the entire PEG chain by the monomer weight, the molecular weights for the two end-groups need to be subtracted. They are 244 g/mol for biotin, and either 33 g/mol for thiol or 16 g/mol for the amino-group. In the case of 10, 62, and 107 monomers the Flory radius calculates to 1.4 nm, 4.1 nm, and 5.8 nm, respectively. Adding up all components gives a gap distance of 8.2 nm for the 700 g/mol PEG spacer. For the medium spacer of 3000 g/mol PEG, a distance of 13.7 nm, and for the largest spacer of 5000 g/mol PEG, a distance of 17.0 nm can be assumed (see Table 6.1). An on-scale drawing of the respective distances and sizes can be seen in Figure 6.4. The magnitude of the gap distances obtained here are in agreement with the experimental results of [167].

Furthermore, for all dimers with different spacer sizes the average resonance positions over the gap distance obtained are fitted with the universal scaling law introduced in Section 2.3 (see Figure 6.5). Again good agreement within the boundaries of the precision of the measurement can be observed.

6.3 Experiments on dimers under strong illumination

Now, I present data of an illumination induced plasmon resonance red shift of gold and silver nanodimers. Even though the steric hindrance of this polymer holds the particles at a roughly constant distance under weak illumination, strong illumination induces a red shift of the resonance wavelength. Such a red shift is a

---

[15] Other literature sources present slightly different power laws. Kawaguchi et al. calculates the mean square radius of gyration by: $< R_G^2 >= 4.08 \cdot 10^{-2}\, M_W^{1.16} \frac{\text{Å}}{\text{g/mol}}$ [170]. Devanand and Selser give for the radius of gyration $R_G = 0.215\, M_W^{0.583 \pm 0.031}\,\text{Å}$ [171].

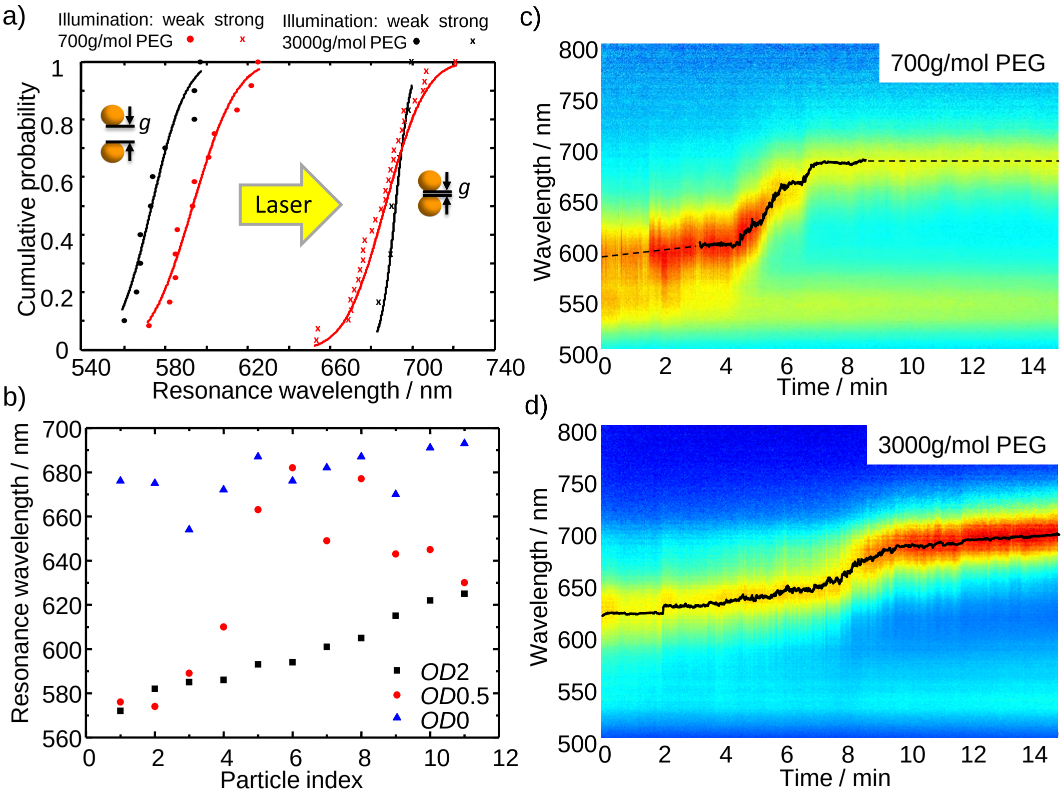

Figure 6.6: a) Cumulative probability of particle resonance positions before and after strong illumination for 700 g/mol PEG spacer (blue) and 3000 g/mol PEG spacer (green). The tremendous red shift can be explained by particles approaching each other. b) Determination of the threshold power needed to induce the collapse. For 700 g/mol PEG dimers an attenuation with a neutral density filter with optical density 0.5 will collapse approximately 50 % of the dimers. c) and d) Full spectral plot of the resonance shift followed in real time for 700 g/mol PEG and 3000 g/mol PEG spacer for a single dimer in each case.

strong hint for two particles approaching each other. In the following, I discuss the characteristics of this approach, like its dependence on the power and wavelength of the illuminating laser, or the partial reversibility on short time scales. Several experiments to investigate the origin of the particle collapse were carried out without the definite identification of the mechanism behind it.

The resonance wavelengths of several dimers with two different spacer lengths are shown in Figure 6.6a for weak and strong illumination. Under weak illumination, the spacer length influences the resonance wavelength, as a longer spacer induces a resonance wavelength further in the blue (see Section 2.3). During strong illumination, the resonance wavelength shifts into the red, there no significant difference between the two spacers is present anymore. For such a red shift, two sources can be considered: either an optical force generated by the coupled near fields of the two nanoparticles, or heating which causes the spacer polymers to 'gas out' and pull the particles together. In the following, I will reflect on the results of several experiments and discuss the impact on each of the two theories.

6.3.1 Threshold power

An interesting parameter is the threshold power at which the gradual red shift can be observed. This was tested with a variable reflective[16] neutral density filter positioned in the illumination beam. At optical densities (OD) higher than 0.5 and at 100 % laser power, no red shift was observed for dimers with a 700 g/mol PEG spacer. In the case of OD 0.5, a red shift could be observed in roughly 50 % of the dimers. Looking at Figure 6.6b, interestingly, this power was generally sufficient for dimers with a starting resonance wavelength higher than 585 nm. Furthermore, an increase of the illumination power lead to an accelerated red shift.

Also the spacer length influenced the time until final collapse. For smaller PEG spacers, the collapse was faster (see Figure 6.6c and d). Statistics of the different time scales were not acquired.

6.3.2 Responsible wavelength regime

Extensive studies on the wavelength range causing the red shift were performed. Thus, the resonance wavelength of the sample when illuminated with individual wavelength regimes was investigated. Starting with the full spectrum between 460 nm and 2400 nm (covered by the white light laser), first, the entire NIR part was cut out of the laser beam by specific reflection of the visible regime. Additional absorption filters were included to exclude further parts of the white light laser. The final wavelength regime used for dimer illumination is reported directly with the finding of the experiment:

Illumination with the regime of 460 nm - 600 nm introduced also a slight red shift of approximately 30 nm within 15 min. In the presence of the entire wavelength regime, a shift of approximately 100 nm could be seen within this time scale. Illumination with the regime of 590 nm - 650 nm for 15 min introduced the maximum resonance shift of 100 nm. The wavelength regime of 650 nm - 750 nm induced also a big shift (10 nm in 3 min). As the power of all wavelength regimes were of comparable magnitude, the first conclusion can be drawn. Wavelengths longer than the resonance wavelength, which was approximately at 600 nm, caused a stronger shift than wavelengths shorter than the resonance wavelength. As such a behavior is expected for optical forces this strongly suggests optical forces as origin of the collapse [85, 87].

Furthermore, I coupled a **808 nm diode** laser via several mirrors onto the sample (see Figure 6.7a). Running this laser diode for 15 min with a maximum power of approximately 300 mW, measured at the sample plane, did not cause any changes in the resonance position of the observed dimer. Even though the provided power was higher then in earlier cases, other drawbacks had to be taken into account.

---

[16] Note: Absorptive neutral density filters crack due to the high amount of energy deposed in the material.

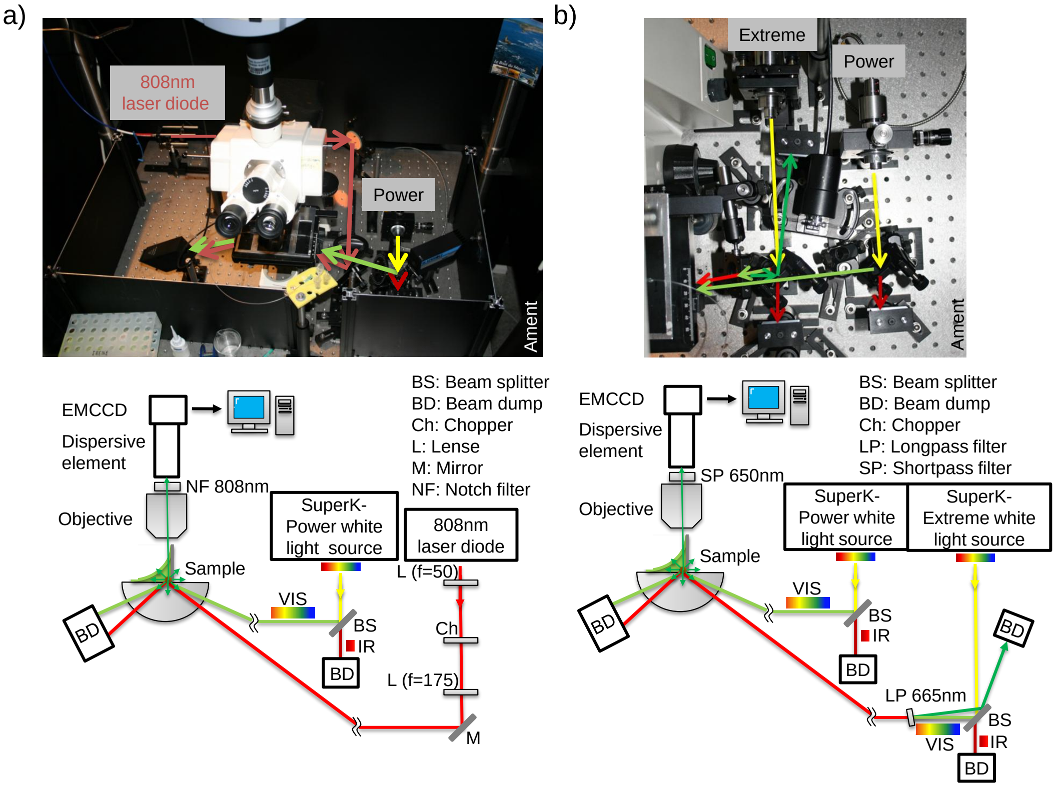

Figure 6.7: Additional variations in the illumination of the Plasmon Fluctuation Setup. a) shows the exclusion of the NIR component of the original SuperK-Power white light laser and an additional 808 nm laser diode. b) shows the coupling in of a second white light laser, SuperK-Extreme, where only the 665 nm to 750 nm regime is used for sample manipulation. The NIR part of the original white light is coupled out. In the detection pathway a 650 nm short pass filter avoids detection of light from the SuperK-Extreme laser source.

First, it was difficult to focus such a strongly divergent light source onto a small spot. Second, measuring the spot size of NIR light at a TIR interface was not straight forward but was rather an estimation from the spot size of the laser beam before entering the prism. As the spot size is directly related to the power density at the sample, no accurate conclusion can be drawn. Either the density was too low, or the wavelength did not induce collapse. Yet, all longer wavelength regimes showed a resonance shift, thus, the first assumption seems more probable. If this is the case, perhaps only minor red shifts were caused by the laser diode. This was tested by chopping the diode light at a frequency of 30 Hz, expecting to recover a periodic signal with the same frequency in the time trace of the resonance position. However, correlation between the resonance wavelength and illumination from the diode laser could not be found. As a side remark I point out that this finding might be a hint towards the importance of the pulsed illumination as the average power of white light laser and diode laser are comparable but the white light laser is pulsed.

Another method to analyze and manipulate the dimer signal simultaneously is to couple in a **second white light laser** as shown in Figure 6.7b. To avoid detection of the manipulating laser, the sample was illuminated only with wavelengths between 665 nm to 750 nm. A short pass filter of 650 nm cut this regime out in the detection path way. As a control, the background of only weak white illumination was compared to the background of an additional strong white illumination and found to be similar. The experiments done with this configuration were aiming at the question of reversibility of the collapse of the linkers as discussed in the next paragraph.

6.3.3 Reversibility of the collapse

An interesting question to inquire is the reversibility of the dimer red shift. If optical forces are the reason one would assume, at least to some extent, that the collapse is reversible. The full back shift might be hindered due to rearrangement of the interparticle spacers and additionally forming biotin-streptavidin connections. Also discussed in literature is the stabilization of an achieved gap distances via van der Waals forces [97].
If heating is the origin an initial blue shift of up to 2.6 nm for dimers with a 700 g/mol PEG spacer and 26.3 nm for the 3000 g/mol PEG spacer can be expected due to full PEG stretching (volume expansion) when heated. If the laser power causes permanent destruction of the linker polymer, non-instantaneous distance changes can be assumed to be irreversible.
Also possible is the combination of optical forces and the destruction of gap molecules via heating in the junction, followed by additional linkage of previously free biotin-streptavidin molecules at the outer, now closer regions.

For the first experiment, a neutral density filter with $OD\,2$ was inserted and taken out periodically from the illumination beam of the SuperK-Power white light source. Investigation of a dimer with a 3000 g/mol PEG spacer under these variable illumination conditions revealed no back shift of the resonance wavelength in the low illumination period (see Figure 6.8a). Definite red shifts in the strong illumination period could nevertheless be observed. The discrete intersections at illumination intensity changes are attributed to small resonance wavelength discrepancies induced by the additional surface of the neutral density filter or a slight volume expansion of the spacer due to temperature increase.

The second experiment used both white light lasers as described in Section 6.3.2. Here, a shorter period of alternation was used and the more sensitive 700 g/mol PEG dimer was chosen. Figure 6.8b shows the result. An oscillation in the resonance wavelength can clearly be seen. Additionally, intensity changes were observed. As particles approaching each other result also in an intensity increase, it is surprising to see the inverse effect. The intensity of the dimer system decreased when illuminated. The same effect was also present for the longer PEG spacer of 3000 g/mol (see Figure 6.8c upper row). Here, the strong laser was turned on only once. However, the intensity increase via illumination was also observed (see Figure 6.8c lower row). A possible explanation is the slight reorientation of the

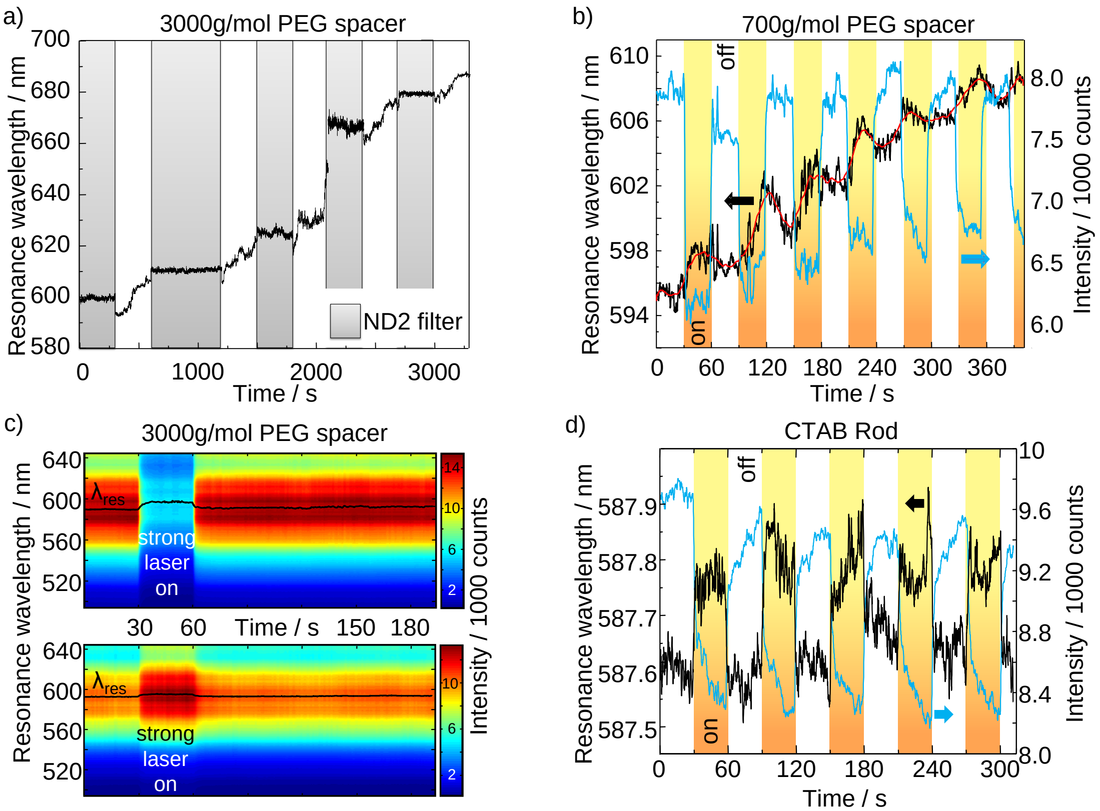

Figure 6.8: a) The graph shows the illumination intensity dependent resonance wavelength of a dimer with a 3000 g/mol PEG spacer over time. Gray background corresponds to a neutral density filter of optical density two inserted into the illumination beam. b) The illumination intensity of a 700 g/mol PEG dimer is altered by illuminating additionally with a second white light laser between 665 nm and 750 nm. Periods when the second white light laser is turned on are marked with a yellow background. A change in resonance wavelength (black) as well as in intensity (blue) appears. The red curve is a smoothed resonance wavelength. Noticeable are the different time scales used for the two experiments in a) and b). c) Plasmon intensity changes of two different dimers with altered illumination intensity investigated with a linear analyzer parallel to the long interparticle axes. Upper row, this dimer shows an intensity decrease due to the strong illumination. Lower row, this dimer shows an intensity increase due to the strong illumination. In both rows a red shift due to illumination was measured. d) Resonance wavelength behavior of a rod under altered illumination intensities. Periods when the second white light laser is turned on are marked with a yellow background. The resonance wavelength (black) as well as the particle intensity (blue) vary.

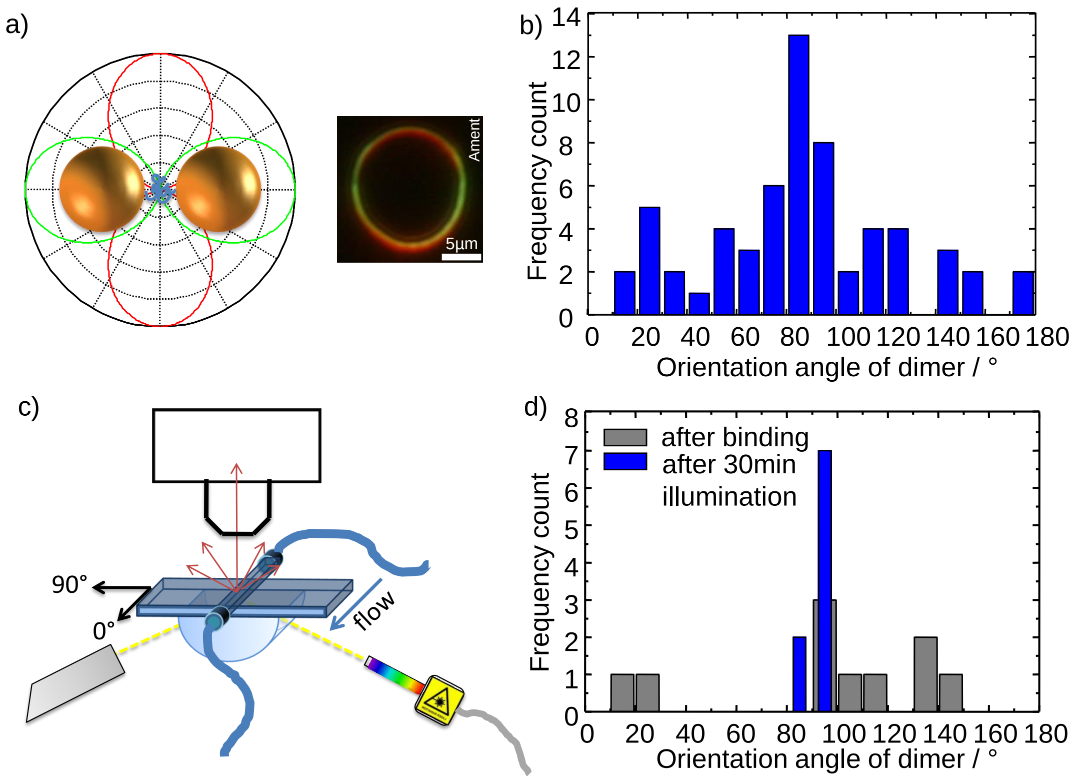

Figure 6.9: a) On the left, a scheme of the scattering pattern of a dimer is shown. On the right this pattern can be seen obtained from a measurement with a rotational polarizer and lateral offset. b) Dimer orientation after illumination of all measured particles. This data was taken from all experiments. Therefore, the illumination time is not well defined. c) Experimental settings for the orientation experiment. The fluid flow and the illumination direction are orthogonal. d) Dimer polarization before and after illumination.

dimer in the more intense evanescent field due to the absorption and gradient forces present under illumination (see Section 2.6). Such a reorientation will be discussed in a later paragraph within this section. Astonishingly, the same effect of changing wavelengths appeared in the case of a rod under alternating illumination strengths (see Figure 6.8d). One explanation can be a volume increase of the CTAB layer due to the increased particle temperature. This would then push the rod further away from the surface of total internal reflection which again results in an intensity decrease and an apparent resonance red shift (see Section 2.5).

6.3.4 Monomer illumination

Astonishing is the fact that after a strong monomer illumination of 1 h with the SuperK-Extreme laser at 100%, dimerization was completely inhibited. Even after 1 h of incubation with the respective counter spheres no dimers had formed in the illuminated region. At not illuminated regions the process of dimer formation was not followed. However, in these regions polarization dependent spots changing between red and green were found after the dimerization time.

In the control experiment where only the weaker SuperK-Power laser was turned on, 50 % of the monomers formed dimers within 10 min. However, detachment of the second particle could not be observed, neither when illuminated with strong laser light nor under weak illumination.

6.3.5 Dimer orientation

A strong hint for optical forces is the preferred dimer orientation after illumination. Investigation of all dimers measured showed a strong orientation parallel to the illumination plane (see Figure 6.9b). It has to be noted, that for this statistic, dimers were not explicitly checked to be already in the final position of collapse. As this dimer orientation matches the direction of flow, the experiment was repeated with a turned flow cell to avoid a possible influence (see Figure 6.9c). Here, the illumination time was long enough to allow complete collapse in all dimers. Now, reorientation is even more pronounced, proving that the flow direction is not the cause of the dimers' orientation (see Figure 6.9d). A χ^2-test on the independence of the orientations obtained revealed a probability of 13 % before illumination, whereas, after illumination this probability decreased to almost zero. As the value of 13 % is quite low, a higher statistic would be advisable for this experiment. Reorientation after collapse was also tested, but this was not the case.

6.3.6 Temperature bath

To study the influence of cooling on the dimer collapse, the surrounding fluid was cooled in an ice bath. The tempered liquid was then sucked through the flow cell. A 40x oil immersion objective was used to avoid having condensed water in the detection beam path. Despite constant cooling of the sample, the continuous red shift could still be observed.

6.3.7 Silver dimers

Assuming optical forces to provide the mechanism for the collapse, the particle distance change should be inverse for silver dimers illuminated with the right wavelength regime. This opposite effect is discussed in Section 2.6 and results from the different dielectric function of silver. As test, I have performed the same experiment as before, but with silver dimers.

Functionalization of 40 nm silver spheres was carried out similar to the preparation of gold spheres (see Section 6.1) with 3000 g/mol PEG used as the spacer. When introduced into a flow cell, particles immobilized onto the glass surface without the presence of additional salt. The resonance position of silver monomers was measured in the ensemble spectrometer (see Appendix C.2) to be approximately at 415 nm. Because 460 nm is the lowest wavelength produced by the WLL, only

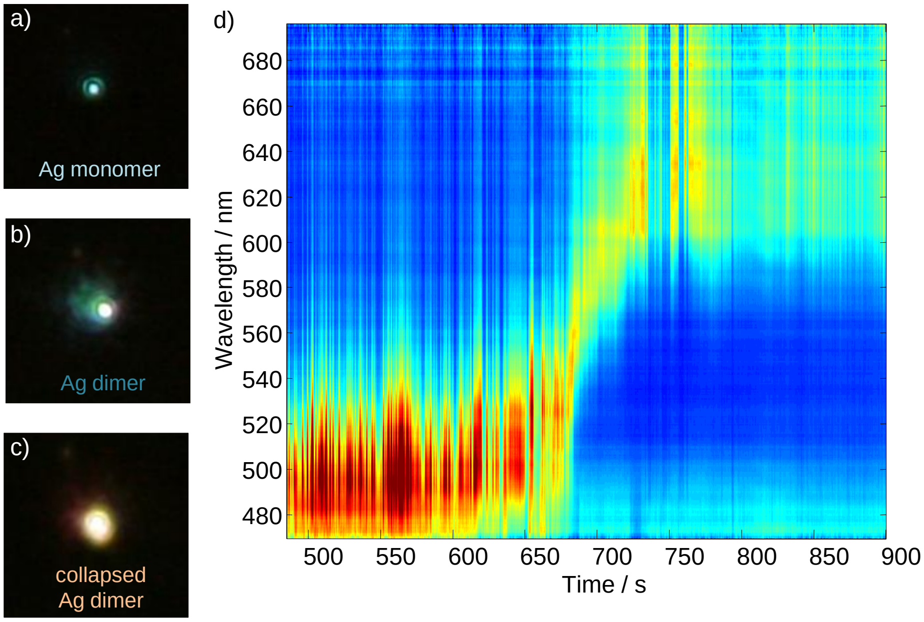

Figure 6.10: The diffraction limited spots of a) a silver monomer, b) a silver dimer, and c) a collapsed silver dimer are shown. d) The collapse is monitored in real time. The strong intensity fluctuations come from a particle loosely binding to the surface.

the long wavelength shoulder of the resonance peak could be seen for monomers (see Figure 6.10a). Dimerization with the second particle increased the spot intensity and changed the resonance wavelength to approximately 490 nm (see Figure 6.10b). Illumination with 100 % laser power also induced a strong red shift in the silver particles (see Figure 6.10c and d). Nevertheless, silver has, due to its different dielectric function, a wavelength regime where repulsive forces are expected (Section 2.6). Further investigations including the variation of illumination wavelengths would be highly interesting. But, because of the difficulties of creating and handling silver dimers, no such experiments were carried out within this thesis.

6.4 Theoretical investigation

Detailed theoretical background on nanoparticle heating and optical forces between nanoparticles can be found in the Sections 2.4 and 2.6. However, a brief review with a focus on the parameter values used during the experiments shall not be missing in this Chapter.

Nanoparticle heating

Equation 2.15 is used to calculate the temperature increase of a spherical particle. If the thermal constant for polymers is inserted into the equation a temperature

rise of about 0.27 K is achieved for a single sphere in the Plasmon Fluctuation Setup. This value roughly doubles for dimers due to the presence of the second sphere.
Even though I argued in the theory section that the laser should be considered as continuous. I take to look at the temperature increase obtained by the power density during the pulse. For a sphere surrounded by polymer a tremendous temperature rise of about 275 K would be expected. Therefore, if the assumption of only considering an average intensity is incorrect, the deposed heat might denature the polymer.

Optical forces between nanoparticles

The calculation of interparticle forces is as complex as the prediction of the resonance wavelength of coupled nanoparticles (see Section 2.3). Thus, in our days, no analytic description exist which predicts the force between illuminated close by nanoparticles. However, numerical results based on e.g. DDA are published [97, 98, 99]. These publications use either gold or silver nanodimers and illuminate with one single wavelength only. Laser powers used for simulation vary between $1\,\mathrm{kW/cm^2}$ and $1\,\mathrm{MW/cm^2}$. As comparison the white light laser implemented in the Plasmon Fluctuation Setup has a laser power per wavelength of $250\,\mathrm{W/cm^2}$ during the pulse and an average power per wavelength of $0.1\,\mathrm{W/cm^2}$. As not only a single wavelength was used during the experiments performed in this thesis an integration over the respective regime is required. Looking at the wavelength regime of 650 nm - 750 nm which is closest to the 800 nm used in the publication of Hallock et al., thus, gives a power of $2.5\,\mathrm{kW/cm^2}$ during the pulse or $10\,\mathrm{W/cm^2}$ in average. As the optical force scales linear with the illumination power a rough estimation can be made for the attractive force using the data of Hallock et al. [97]. The force obtained for a gold dimer with 60 nm diameter spheres in the Plasmon Fluctuation Setup are ~34 fN during the pulse or ~136 aN for the power average. Considering the interparticle polymer as spring with the spring constant, k=10^{-4}N/m, then a displacement of approximately 0.34 nm can be assumed during the pulse. As the interparticle gap is only in the order of 10 nm - 15 nm this small displacement might be sufficient to obtain the gradual red shift seen due to reorganization of the polymer outside the gap.

However, comparison of this optical force with the van der Waals force between the two spheres reveals its low magnitude. The van der Waals force can be calculated via $F_{\mathrm{vdW}} = \frac{AR}{12g^2}$ [98], with the Hammaker constant $A = 1 \cdot 10^{-19}$J for gold [97], particle radius R, and inter particle gap g. For 60 nm diameter gold spheres at a distance of 10 nm the van der Waals force derives to 2.5 pN. Note that this force should strongly squeeze the interparticle polymer even leaving the linear regime of the assumed spring.

Conclusion of the theoretical investigation

The theoretical investigations of nanoparticle heating and optical forces between nanoparticles do slightly favor heating as mechanism. However, no definite prediction is possible.

In the next paragraph I summarize the findings of experiment and theory and give a short outlook on further experiments which might indicate the origin of the dimer collapse.

6.5 Conclusion

In Table 6.2 the implications of the experiments investigating the mechanism of the collapse are recapitulated. The presence of a threshold power, the faster collapse with stronger illumination, and the influence of the PEG length do not pinpoint one origin for the dimer collapse. A strong sign for optical forces is the wavelength dependent effect with a maximum just above the plasmon resonance as expected by theory. Intuitively, full reversibility of the collapse is expected in the case of optical forces, but the formation of additional biotin-streptavidin bindings can account for as seen incomplete reversibility. The fact that strong illumination of monomers for a long period inhibits the formation of dimers can only be explained with a denaturation of the binding protein. However, if heating is the reason, one would assume detachment of the secondary particle when strongly illuminated, which was not observed. An argument for optical forces is the realignment of the dimer due to strong illumination. Short term reversibility, and the independence from liquid temperature also supports optical forces. Also, recall the small temperature increase theoretically obtained: the calculated temperature increase in the case of a dimer fully surrounded by polymer is $< 1\,\mathrm{K}$.

Observation	Heating	Optical force
Threshold power	+	+
Stronger illumination leads to faster collapse	+	+
PEG length influences time till collapse	+	+
Strongest effect due to wavelengths just above resonance	-	+
No long term reversibility	+	0
Short term reversibility	-	+
Illuminated monomers do not form dimers	+	-
2nd particle does not detach	-	+
Dimer alignment after strong illumination	-	+
Cooling sample does not influence effect	-	+
Gold rod shows an effect	+	-

Table 6.2: Comparison of possible causes for the dimer collapse. If the observation is in agreement with the cause, it is marked with '+'. If it cannot be explained by it, it is marked with '-'. If no conclusion is possible, it is marked with '0'.

Nevertheless, the predicted temperature change during the pulse might easily explain polymer destruction. Also, the fact that changes were seen on a gold rod points towards heating effects. All together, neither of the two mechanisms is able to explain all seen effects. Thus, a combination of optical forces and a heating effect is the most probable explanation for all seen behaviors.

Outlook

The route for the future of the dimers studied here includes additional experiments to certainly uncover the responsible mechanism(s) for the dimer approach. In my eyes, most promising seems to be a detailed study of silver dimers with varied wavelength regimes. If the collapse can be inverted when the particles are illuminated at about their resonance wavelength a definite prove for the presence of optical forces would be given. To learn more about the actual temperature at the particle surface further studies including temperature responsive polymers similar as in Chapter 3 could be useful. Perhaps even the implementation of temperature responsive dyes might be advisable if their light is of resonance and a work around the problem of quenching can be achieved. Additionally, I advise a study investigating the surface coverage of the polymer. If the particles are only covered sparsely with the polymer, no polymer deformation or denaturation is needed to explain the particle approach seen.

7 Nanodimers as Sensors for Spacer Stiffness or mysterious slow distance fluctuations in polymer coupled nanodimers

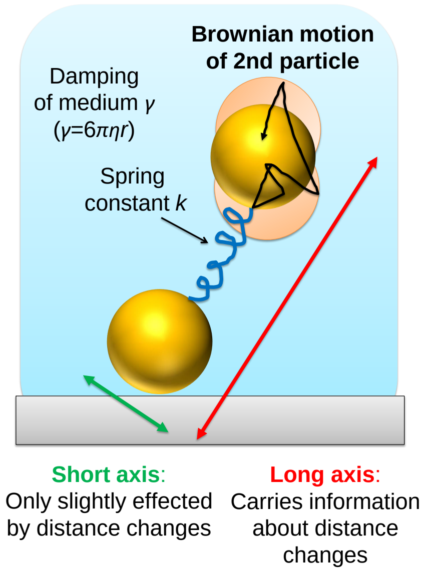

Figure 7.1: Distance fluctuations of the dimer caused by the movement of the secondary particle due to Brownian motion can be investigated via the resonance wavelength of the long axis.

The stiffness of a polymer chain is an important design parameter in polymer synthesis. It is usually determined by measuring the end-to-end distance, either as function of an external force or by looking at equilibrium fluctuations. Common techniques include fluorescence resonance energy transfer (FRET), electron paramagnetic resonance (EPR), optical tweezers, and atomic force microscopy (AFM). However, these methods work only for relatively small end-to-end distances (below 10 nm) or, in the case of optical tweezers, for very large end-to-end distances (above 1µm). AFM is so far limited to forces above pN. As discussed in Section 2.3, a dimer of plasmonic nanoparticles is extremely sensitive to changes of the interparticle distance and therefore can serve as nanoruler [161, 162, 163, 167]. With the improved time-resolution for measuring plasmonic spectra that I developed (see Chapter 4), such plasmonic nanorulers could serve as an alternative method to measure polymer stiffness. For this a polymer is attached at each end to a plasmonic nanoparticle (see Figure 7.1). Then, as seen in Section 2.3, the resonance wavelength of the system reports on the time resolved distance of the two spheres defined by the polymer configuration. This method has the advantage of much better photo-stability than dyes used in FRET, covers a larger distance regime and the strong light scattering efficiency of plasmonic particles allows for much higher time-resolution down to microseconds.

Before I explain the basic concept of the plasmon nanoruler, I give a brief overview on today's techniques to measure nanometer distances. The most conventional method is based on fluorescence resonance energy transfer (FRET) [173]. Major drawbacks of this method are the limited available distance range of 1 nm to 8 nm and the strong orientation dependence of the dye on energy transfer. In 2002, the concept of electron paramagnetic resonance (EPR) to determine nanoscale distances was introduced. [174]. However, this method, based on the dipole dipole coupling between two spins, is again limited to distances smaller than 8 nm. A more direct method to measure polymer stiffness attaches two ends of a polymer to two micrometer-scale beads which are trapped optically [175]. The exerted force on the traps can be measured when the polymer is deformed. Conformational forces can also be measured with atomic force microscopes (AFM) [176].

To explicitly test plasmonic nanoparticle dimers as stiffness sensors I took time traces with an exposure time in the millisecond regime and analyzed the resonance wavelengths. The long axis plasmon resonance showed strong fluctuations considerably above the noise level. The autocorrelation of these fluctuations resulted in a typical decay time in the order of seconds, several orders of magnitude longer than the time-regime predicted by calculations for equilibrium fluctuations of the system. To understand the origin of those slow fluctuations, I varied several experimental parameters, namely the viscosity of the surrounding medium, the polymer used as linker, the polymer length, the size of the second particle, and applied external force. None of this variations resulted in a clear trend and the origin for the slow fluctuations remains mysterious.

Please notice, all measurements in Section 7 were carried out without knowledge about dimer collapse described in Section 6.3.

7.1 Experimental results

Time traces of the resonance wavelength of monomers, short and long axis of the dimer were acquired. The laser power for the dimer fluctuation experiments was 50 % and the exposure time was set to 10 ms. The EMCCD amplification, called gain, was adjusted to optimize acquisition intensities. In the case of monomers, a gain of 100 was normal; for dimer measurements, no gain was needed. Furthermore, a linear polarizer was introduced in the detection path to measure the two axes of the dimer independently. The time dependent resonance wavelength was checked for autocorrelation $G(t') = \frac{<\delta I(t) \cdot \delta I(t+t')>}{<I(t)>^2}$ for $t'>t$ to exclude the autocorrelation always present at this condition. If autocorrelation was present, the curve was fitted by an exponential decay with time, τ. For monomers and short dimer axes, only minor changes in the resonance wavelength were seen and no autocorrelation was found. In the case of long dimer axes, resonance wavelength variations of several nanometers were present. The autocorrelation time, τ, was on the order of seconds (see Figure 7.2).

To better understand the origin of the fluctuation causing autocorrelation, several parameters were varied. As theory predicts $\tau = \gamma/k$ (see Section 7.2), a change in the environmental damping, γ, should influence the decay time. Also dependency of the decay time on the spacer stiffness, k, could be expected. Furthermore, I tested the influences of the interparticle gap distance, the size of the second particle, and an external forces on the autocorrelation time. The different findings for each experiment are presented in the following.

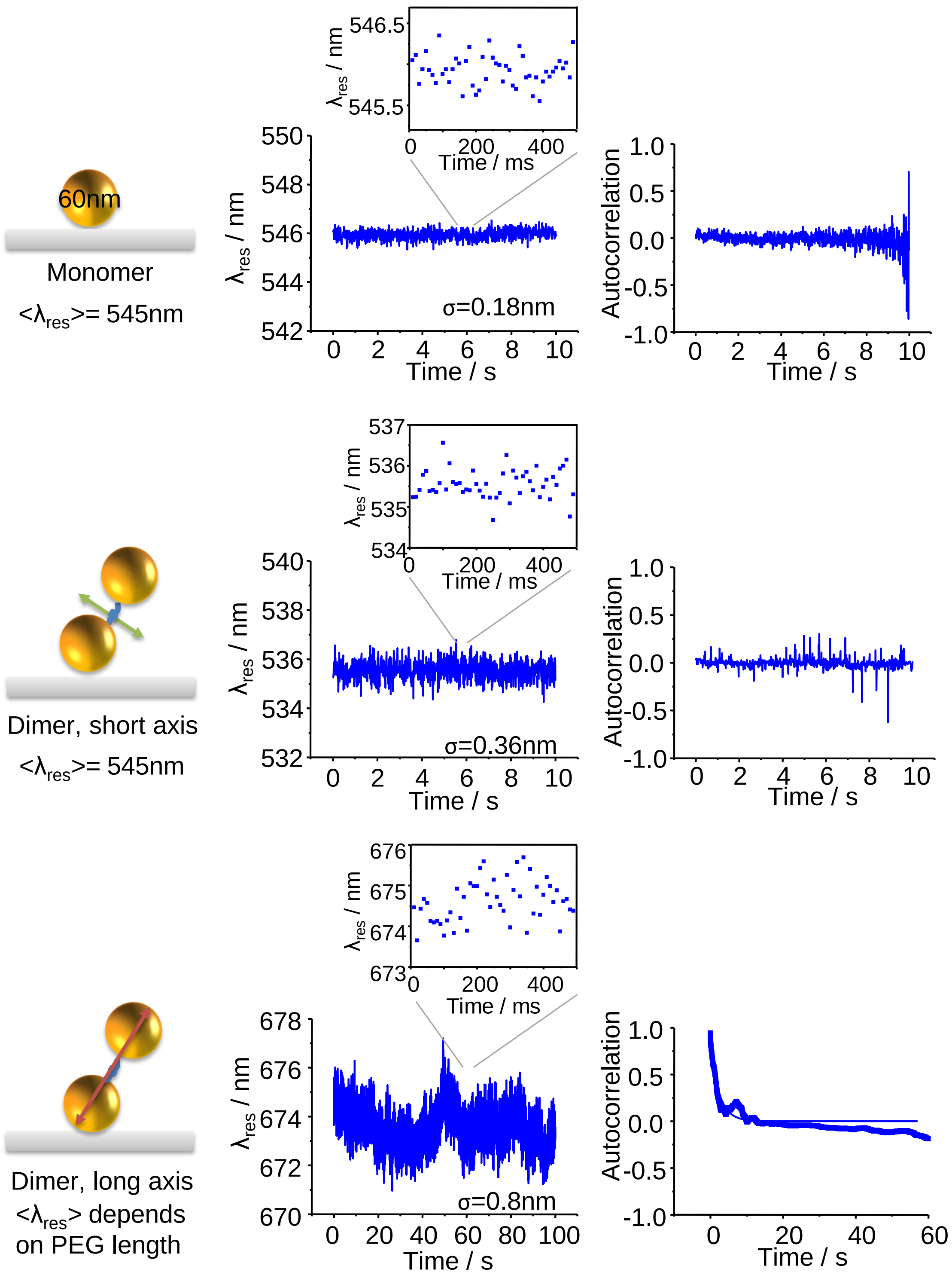

Figure 7.2: Left column: respective illustration for each row. Middle column: typical time trace of the resonance wavelength and enlarged detail of the trace. Right column: respective autocorrelation function. Wavelength fluctuations for monomers and short dimer axes correspond to noise, no autocorrelation can be observed. In contrast, fluctuations in resonance wavelengths of long dimer axes are much more pronounced producing an autocorrelation above noise. The autocorrelation decay time is on the order of seconds.

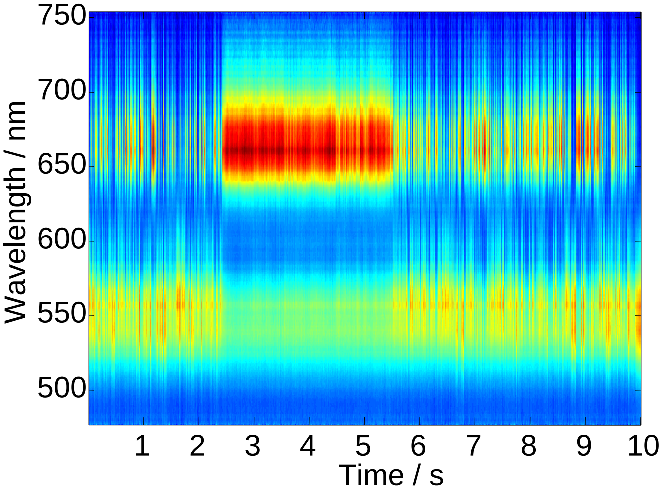

Figure 7.3: Spectrum variation in intensity and resonance wavelength of a loosely bound particle in 20% glycerin solution.

Viscosity of the surrounding liquid

To change the environmental damping, the viscosity of the surrounding medium was increased. This was done by exchanging the buffer solution with a buffered glycerin mixture. Glycerin fractions with increasing values between 5 % and 40 % were used. However, a change of solution might alter the system condition, e.g. the distance between particles might be modified due to the different solvent. Furthermore, the strength of the particle's attachment to the glass surface decreased. Thus, particles were not that well attached anymore. In the spectrum, this was evidenced by the resonance wavelength and/or intensity changing strongly with time (see Figure 7.3). Such loosely bound particles easily detached from the surface and could not be measured anymore. Hence, the sample size for nanoparticle statistics decreased. However, for glycerin concentrations up to 40 %, no significant change in τ was measured (see Figure 7.4a)

Different spacers

Theoretically, the decay time of the autocorrelation function should be influenced by spacer stiffness. Thus, insertion of another spacer is of interest. However, such a change in the spacer polymer is not straight forward as preparation conditions have to be optimized. Therefore, a system introduced by was used [167]. She exchanged the PEG molecule by an elastin-like polypeptide [177] (provided by) maintaining the biotin streptavidin recognition. The preparation method is described in Appendix B.2. I used the E4-20 sample which introduced an average dimer gap distance of 10 nm under weak illumination. Therefore, the distance is comparable to the shortest PEG spacer. Exposure time and EM gain were kept similar to previous experiments. The number of gathered frames was three times larger than for PEG dimers. Figure 7.4b presents the measured correlation times. Here, it seems that the spacer material influences the decay time. However, separation of

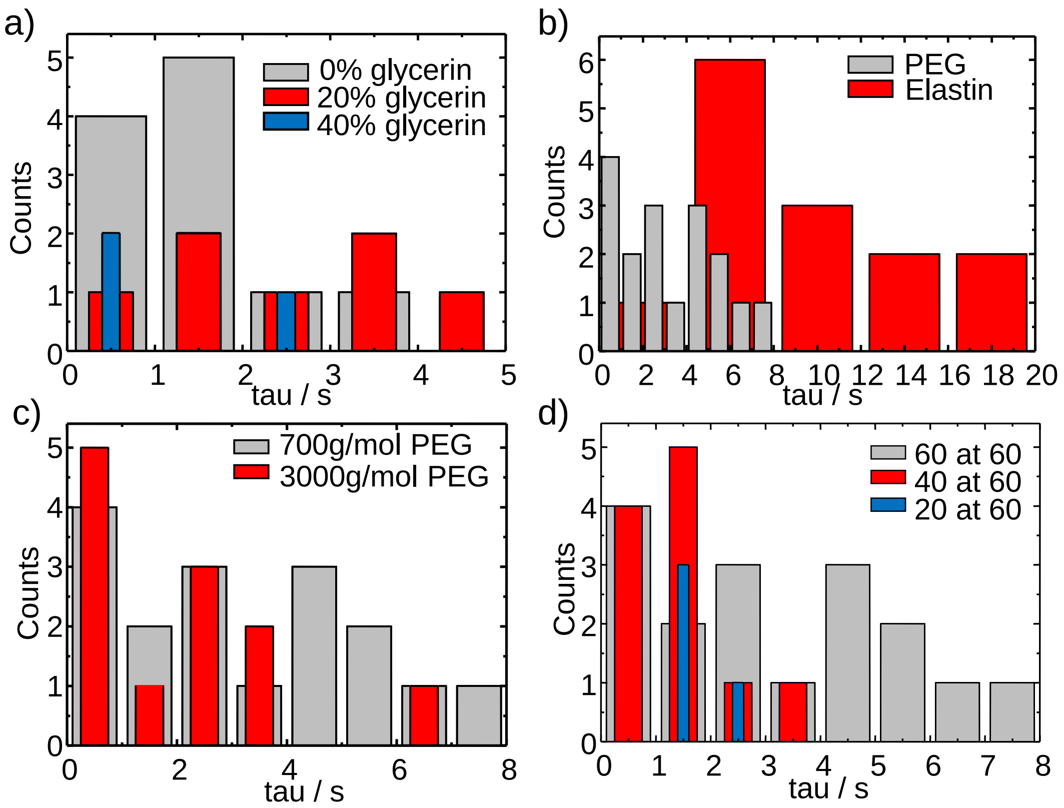

Figure 7.4: Correlation times with varied parameters: a) viscosity of the surrounding medium is varied. b) material of the spacer is changed. c) length of the spacer is altered. d) size of the second particle is varied.

the long time trace into three of the length previously used, showed huge variations of decay times between different sections of the same trace. Thus, again no clear conclusions can be given and further investigations are needed to clarify the influence of the spacer on the autocorrelation.

The elastin-like polypeptide is known to coil in higher salt concentrations. Therefore, the salt concentration of the surrounding medium was varied from buffer solution to 5 M NaCl. This induced a strong red shift as predicted by theory. However, the final resonance position had the same value as given under strong illumination (see Chapter 6). Also, no reversibility could be seen when exchanging the surrounding medium back to buffer solution. Thus, the origin of the shift is not clear and a collapse due to strong illumination, as described in Section 6.3, is probable.

Spacer length

The particle distance was varied by using different PEG lengths (see Section 6.1 and 6.2). Two different distances were used: 8.2 nm including 10 PEG repetition units, and 13.7 nm including 62 PEG repetition units. Such a change in repetition units is predicted to change the polymer stiffness by a factor of 6 and therefore to influence the decay time by the same amount (see Section 7.2). Additionally, assuming interparticle forces to play a role on the distance fluctuations these forces should be varied by the change in distance resulting again in a different decay time. However, the autocorrelation decay time was not significantly altered by this increase in separation distance (see Figure 7.4c).

Size of second particle

In addition, also a series with changing secondary particle sizes was carried out. Dimensions of the secondary particle were 20 nm, 40 nm, and 60 nm, while the diameter of the primary particle was kept fixed at 60 nm. 700 g/mol PEG-biotin with only 10 repetition units of PEG monomers was always used as spacer (see Section 6.2). Indeed, the resonance wavelengths measured vary with the volume of the secondary particle. For 20 nm spheres, an average shift of 52 nm, for 40 nm particle a shift of 105 nm, and for the original 60 nm spheres an average shift of approximately 138 nm was observed. Thus, bigger secondary particles cause a resonance wavelength further in the red regime (see Figure 7.5). This is in good agreement with theory as the strength of interparticle coupling also depends on particle volume. Furthermore, it should be noted that the scattering intensity decreased with decreasing particle size. Again this is in agreement with theoretical predictions. Notice, measurements were carried out without knowledge of dimer collapse. Despite this observation, no significant change was seen in the autocorrelation function (see Figure 7.4d).

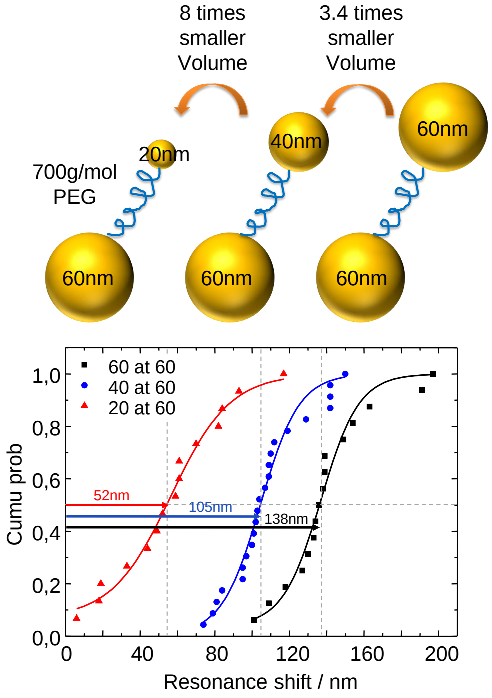

Figure 7.5: Cumulative probability of the resonance positions of dimers with differently sized secondary particles.

External force

An external force on the particles can be created through constant liquid flow. To approximate the magnitude of such a force, the speed of the liquid at the sample position needs to be calculated. I assume the law of Hagen-Poiseuille for laminar flow,

$$\dot{V} = \frac{A^3 B\,\Delta p}{12\eta l}\underbrace{\left[1 - 0.630\frac{A}{B}\right]}_{K} \tag{7.1}$$

to be valid for the rectangular capillary profile of my flow cell[17] [178]. A and B are height and width of the capillary profile (see Figure 7.6). They are $A = 100\,\mu\mathrm{m}$ and $B = 2\,\mathrm{mm}$. Thus, for the flow cell used, the geometry factor, K, is approximately 0.97. The pressure induced flow rate $\dot{V}$ was set between 1-10 ml/min. The viscosity of the liquid, η, for water is 1 mPa s. $l = 30\,\mathrm{cm}$ is used for the length of the flow cell, even though the profile changes in the tubing attached. With these parameters the difference in pressure Δp can be calculated. Combining Equation 7.1 with the height dependent flow speed, $v(z) = \frac{\Delta p}{2\eta l}(A-z)z$[18], yields the flow rate dependent flow speed:

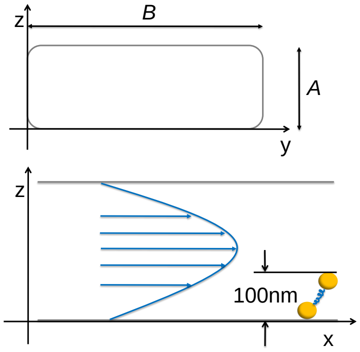

Figure 7.6: Flow cell dimensions introducing laminar flow

$$v(z) = \frac{6\dot{V}}{KA^3B}(A-z)z \tag{7.2}$$

With the drag coefficient, $\gamma = 6\pi\eta r$, the force on the particle can be calculated:

$$F = -\gamma\dot{x} = -6\pi\eta r v \tag{7.3}$$

For the conditions presented here a force in the range of pN is exerted. In equilibrium, the position of this force is compensated by the counter force of the polymer. Thus, $\gamma\dot{x} = kx$, from which the equilibrium position x can be derived. Depending on the flow rate, a change in the equilibrium position between 1-14 nm is expected. However, neither changes in the resonance position nor in the autocorrelation decay time were observed under external force (see Figure 7.7). The reason for this may lay in the fact, that the dimer collapse described in Section 6.3 had already taken place. In future projects, it might be interesting to repeat the experiment with lower illumination power.

Changing the distance to the surface

As the origin of the autocorrelation might be a particle-surface interaction, I tried to increase the distance of the primary particle to the surface. To do so, an

---

[17] Formula 7.1 is an approximation as no analytical solution for the problem exists. Furthermore, it is only valid if $A/B \rightarrow 0$.

[18] In this formula the side walls are neglected completely, treating the problem like two infinite planes. As A $>>$ B this is true in first approximation if the dimer is situated away from the side walls of the flow cell.

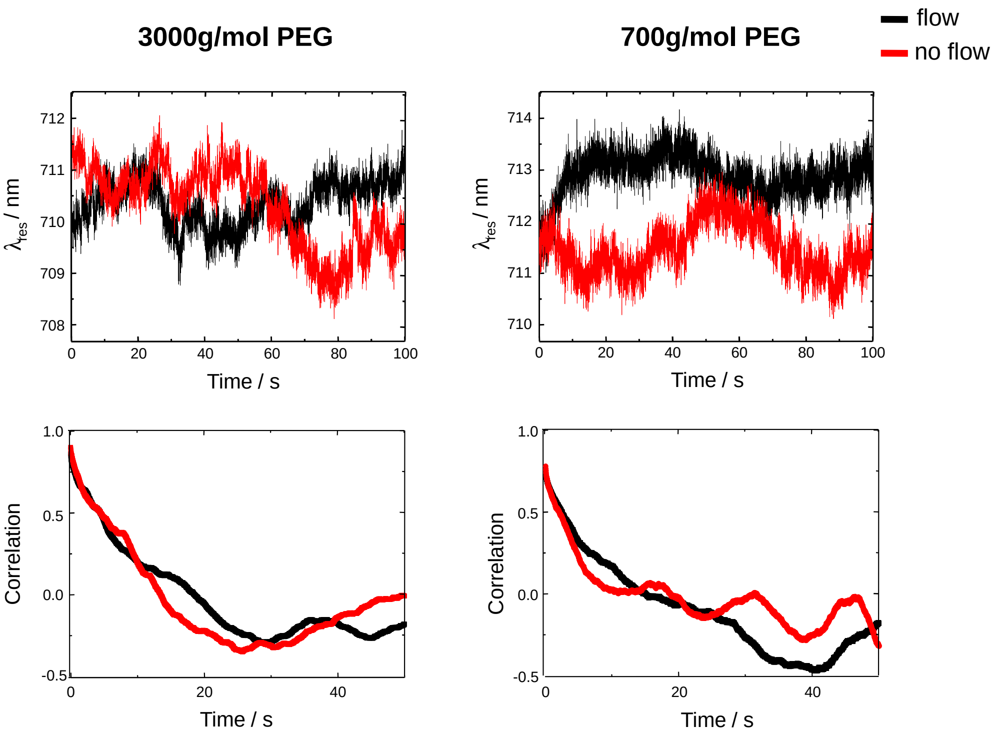

Figure 7.7: Influence of external force on decay time of a dimer with a 3000 g/mol PEG spacer (left) and a 700 g/mol PEG spacer (right). In the upper row, the resonance wavelength over time is plotted without an external flow (red) and with an external flow of 10 ml/min (black). In the lower row, the respective autocorrelation function can be seen. No significant difference can be recognized.

additional layer of bovine serum albumin (BSA, Sigma-Aldrich) was immobilized on the glass surface. 1 % of BSA molecules were additionally functionalized with a biotin group to present an anchor point. During the following preparation, the flow solution was always enriched with 1 mg/ml BSA to ensure glass passivation. After incubation with streptavidin molecules, biotinilated gold spheres were flown into the flow cell and attached to the streptavidin. This step was followed by an incubation with streptavidin functionalized gold spheres to attempt to achieve dimerization. However, under all conditions tested a huge amount of new particles were immobilized. This dramatic increase hindered a potential observation of dimers. A probable reason might be poor saturation of BSA-biotin in the first place, providing anchor groups to the streptavidin gold spheres.

Variation of camera settings

As mentioned before for the ELP, different lengths of the measured time traces influence the decay time extracted from the data. A systematic study where the number of frames, the exposure time, and the cycle time were varied was carried out on a dimeric system of two 60 nm gold spheres with 3000 g/mol PEG as spacer. The laser power was set to 50%; no gain was used. In Figure 7.8 the influence of

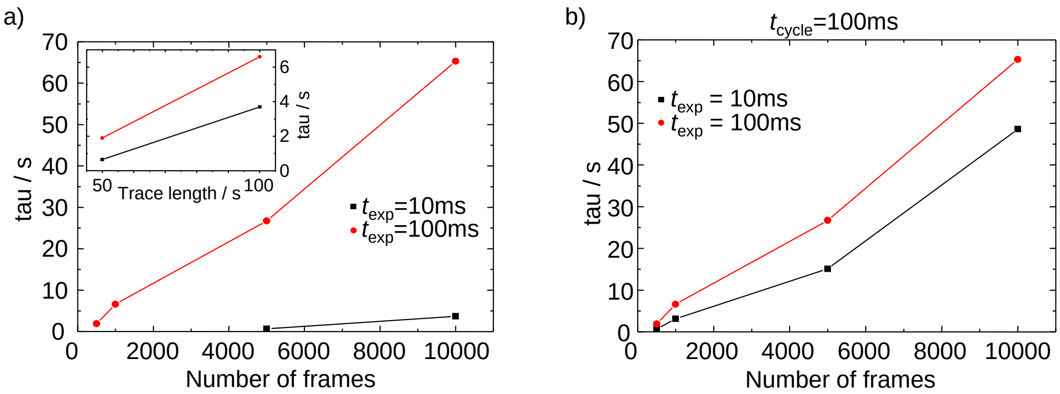

Figure 7.8: a) The number of frames taken is varied for two different exposure times. The cycle time is not fixed, but always 3.7 ms longer than the exposure time. In the inset, time traces of the same absolute time period are compared. b) The number of taken frames is varied for two different exposure times, the cycle time is fixed to 100 ms.

the parameters varied on the autocorrelation decay time is shown. Experiments uncover a clear dependence of the autocorrelation time from the absolute time length of the traces gathered. Notice, autocorrelation functions were again not smooth but showed drastic differences from a nice exponential decay.

7.2 Theoretical calculation of the polymer stiffness

To model a dimer system consisting of one immobilized sphere and one sphere loosely attached to it, several simplification can be assumed: the particle which is immobilized directly to the surface is neglected and only one polymer connects the remaining particle to the surface. This connecting polymer is considered a spring with a certain stiffness or spring constant, k. The theoretical description of motion in such a system is given by the Langevin equation [179]. Calculation of the autocorrelation function, $< x(0)x(t) >$, shows its dependence on the drag due to the viscosity, γ, and the spring constant, k:

$$< x(0)x(t) > \propto e^{-\frac{k}{\gamma}t} \tag{7.4}$$

$\gamma = 6\pi\eta r$: viscosity drag with particle radius r and medium viscosity η

k: spring constant

Equation 7.4 describes an exponential decay with the following time constant:

$$\tau = \gamma/k$$

The drag due to viscosity, γ, of a 60 nm sphere in water ($\eta = 1\,\mathrm{mPa\,s}$) is on the order of $10^{-9}\,\mathrm{Ns/m}$. Literature stated values for the spring constant, k, for PEG with molar weight of 3400 g/mol is in the range of $10^{-4}\,\mathrm{N/m}$ [181]. This value was

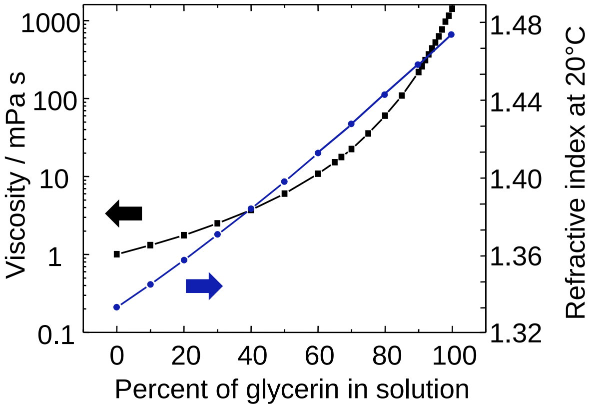

Figure 7.9: Viscosity (black squares) and refractive index (blue circles) of glycerin water mixtures at 20°C [180].

measured and is rough agreement with the value calculated via $k = 3k_\mathrm{B}T/R_F^2 = 3k_\mathrm{B}T/(aN^{0.58})^2$ using the Boltzmann factor k_B, the temperature T , the Flory radius R_F, the monomer length a, and the number of monomers N (for values see Section 6.2, see Figure 7.10). At room temperature, the decay time τ calculates than to be in the order of 6 µs. In the case of pure glycerin ($\eta = 1410\,\mathrm{mPa\,s}$ [180], see Figure 7.9), τ increases to about 8 ms. However, if the glycerin concentration in the mixture is only 40 %, a feasible value for experiments, the decay time increases just by a factor 4 and lays at about 24 µs.

Additionally, I want to point out that slightly smaller values for the stiffness, also refereed to as entropic spring constant, of the polymer can be found in literature [182]. This approach uses rather the mean square end-to-end distance than the Flory radius to calculate the stiffness of the polymer: $k = 3k_\mathrm{B}T/(Na^2)$ [183]. Entering the values for the PEG used here gives stiffness values in the regime of 10^{-3} N/m and therefore even shorter correlation times in comparison to the correlation time obtained by the stiffness cited before.

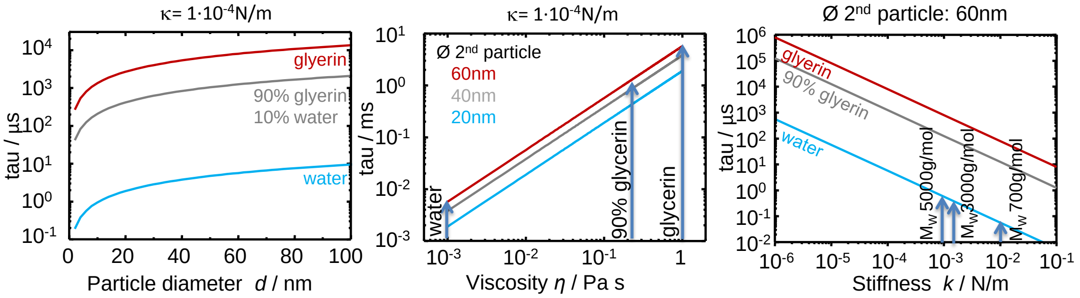

Figure 7.10: Correlation times predicted by theory for stiffness measurements with varied parameters

7.3 Conclusion

All experiments concerning correlation of resonance wavelength along the dimer long axes were carried out without the knowledge of strong illumination collapsing the system. Thus, it might be possible that Brownian motion is not the origin of the changes in the resonance wavelength, but a rearrangement or denaturation of the polymer in the interparticle gap during the collapse. Against this hypothesis holds the fact that comparable autocorrelation decay times were measured on other setups with illumination powers far below the power threshold for a collapse induced optically. In conclusion, no parameter tested significantly changed the autocorrelation decay time besides spacer material, but even there further tests are needed. The reason for this is subject to speculation: either an unthought of source is the origin of the autocorrelation measured, or the changes are too low to be detected due to poor statistics. Also not understood are different decay times within one time trace if sections are investigated, as it was seen for the elastin-like polypeptide time traces. Perhaps different time components are present in the traces. Depending on the conditions, one or another is more pronounced. This might also explain the roughness of the autocorrelation functions measured.

Outlook

Even though the proof of principle experiment to measure spacer stiffness with the help of nanodimers was not successful yet, future projects should continue the pursuit. Higher time resolution to enter the low microsecond regime, parallel white light calibration, and higher dimer statistics seem to be reasonable routes to follow. Varying sampling time as normally done for FCS or DLS could also be helpful as it would give a meaningful autocorrelation function over several magnitudes of exposure time.

8 Plasmon Correlation Sensing

In our days, the established method to measure diffusion constants and concentrations of dye labeled molecules is fluorescence correlation spectroscopy (FCS). However, FCS is limited to concentrations below most natural concentrations in biological systems, e.g. cells. Hence, I follow the idea of using a plasmonic nanoparticle as sensor to achieve the detection of these concentrations.

Two different detection volumes were tested (see Figure 8.1). In the more simple model, which is mainly an easier to accomplish pretest, the field of camera view is limited by a pinhole. Thus, all particles displayed on the camera are in the detection volume. Intensity changes due to plasmonic particles diffusing in and out of the field of view are detected. Such a method is very similar to the already published method of total internal reflection fluorescence correlation spectroscopy (TIR-FCS) [184]. The more advanced second method takes advantage of the idea of using only the sensing volume of a plasmonic particle as detection volume. With this method, the detection volume is reduced to attoliters and theoretically single unlabeled molecules diffusing in and out of the sensing volume can be observed at a concentration reasonable for a biological environment.

As both plasmon correlation sensing methods are very similar to the well established fluorescence correlation spectroscopy (FCS) I will first briefly introduce this common method. Then, I present the results obtained for the two different sensing volumes.

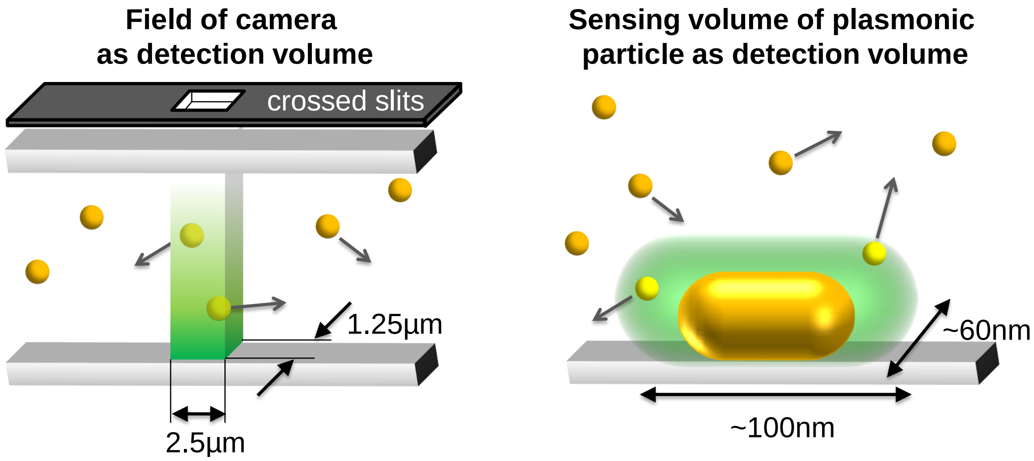

Figure 8.1: Illustration of different detection volumes for plasmon correlation sensing. On the left side the detection volume is constricted by two crossed slits limiting the monitored area on the CCD chip. The resonance intensity of particles diffusing in and out of the detection volume is taken as signal. On the right side the detection volume is given by the sensing volume of the rod. Here, the resonance wavelength of the rod is used as respective signal.

8.1 Fluorescence correlation spectroscopy

Fluorescence correlation spectroscopy is a correlation analysis of intensity fluctuations produced by diffusing dye labeled molecules in and out of a detection volume. Today, FCS is a powerful technique commonly used to obtain information about the dynamic characteristic of a system [185, 186, 187]. It is mainly used to gather information about diffusion constants, concentrations, and interactions of different molecules.
As side remark: Another very similar technique to fluctuation spectroscopy is dynamic light scattering (DLS) which I will not present here. I rather refer the interested reader to the textbook 'Dynamic Light Scattering' of Berne and Pecora [188].

The detection volume used in FCS is the diffraction limited focal volume created by confocal optics. The size of such a volume element is on the order of 200 nm for the radius of the lateral dimension and 2 µm in height. Within this small volume of illumination dyes will be excited. Therefore, as long as a dye is inside the excitation volume it will emit light which can be detected. Due to Brownian motion the number of emitters will vary, thus, the intensity fluctuates. Measuring the intensity of the fluorescence signal over time will hold several pieces of information. To extract this information, the autocorrelation function normalized with the mean square intensity is used (see Appendix C.3). At time $\tau = 0$ the amplitude of the normalized autocorrelation function tells the mean number of objects in the volume of illumination: $G(0) =< N >^{-1}$. It is best to only have a small number of dyes in the volume of illumination. Otherwise fluctuations cancel out and no significant signal can be obtained. The mean residence time in the detection volume is given by the correlation time, τ_D. In an FCS experiment, this parameter depends on the diffusion constant D and the radius of the illuminated spot r_0:

$$\tau_D = \frac{r_0^2}{4D} \tag{8.1}$$

r_0: lateral semi-minor axis of the diffraction limited volume
D: diffusion constant (see Equation 8.2 for spherical diffusers)

For diffusers of spherical shape, normally used in the experiments of this chapter, the diffusion constant D is given by the Stokes-Einstein relation:

$$D = \frac{k_\mathrm{B} T}{6\pi\eta R_\mathrm{H}} \tag{8.2}$$

$k_\mathrm{B} = 1.3806 \cdot 10^{-23} J/K$: Boltzmann constant
T: temperature of the system in Kelvin
η: dynamic viscosity of the surrounding medium
R_H: hydrodynamic radius of the particle

As mentioned earlier, also the interactions among different dye-labeled molecules can be investigated.

Important boundary conditions

The theory presented for FCS is only valid for a volume of illumination situated far away from any adsorbing or reflecting surface. If this is valid, the effective volume calculates to $V_{\mathsf{eff}} = \pi^{\frac{3}{2}} r_0^2 z_0$ with z_0 being the long axis dimension of the spheroid of illumination, generally created in confocal microscopy [187]. If boundary conditions have to be accounted for, analysis is more complex. Particularly, hydrodynamics of the particles change significantly near a solid wall. Furthermore, additional forces for electrostatic double layers and van der Waals forces have to be considered. Even though first important theoretical work dates back to the 1960s [189, 190], experimental work on this subject is still carried out to find a general term for more complex boundary conditions [82, 191, 192].

Now that I introduced the common method of FCS, I move on to the experiments carried out at the Plasmon Fluctuation Setup. First, one section on the field of camera used as detection volume. This experiment, a pretest, is easier to accomplish as diffusing particles can be bigger compared to the afterwards studied configuration. Thus, the diffusing particles scatter enough light to be visible without additional amplifier.

8.2 Field of camera as detection volume

The Plasmon Fluctuation Setup is equipped with a pinhole. Therefore, light coming only from a point-like area is diffracted and its spectrum is pictured on the camera chip. The actual size of the spot monitored is determined by the dimensions of the slit. In the case presented these dimensions are 100 µm×50 µm. With a magnifying objective of 40x, thus, an area of 2.5 µm×1.25 µm is displayed. The height above this area is limited due to TIR illumination mode and can roughly be estimated to be 200 nm for light with a wavelength of 600 nm (see Section 2.5). Experiments with similar settings can be found in literature [193, 194, 195]. There, the effective volume is discussed to be[19] $V_{\mathsf{eff}} = \frac{A_{\mathsf{det}}}{2} \frac{(\int I(z)dz)^2}{\int I(z)^2 dz} = A_{\mathsf{det}}\gamma$. This converts for my settings as follows: A_{det} is the area detected by the camera and γ is the penetration depth of the evanescent wave (see Section 2.5). For the settings used here, the effective volume is $6.25 \cdot 10^{-13}$ml. As I discussed in the section before, a concentration of one to a few particles in the detection volume is optimal. Therefore, a concentration of $1.6 \cdot 10^{12}$ particles/ml should be used theoretically. Smaller concentrations result in less frequent events. Also the shape of the diffuser has to be considered. Only in the case of spherical particles

---

[19] Like in the case of the penetration depth of an evanescent wave (see Section 2.5), deviations by factor two can again be found in literature.

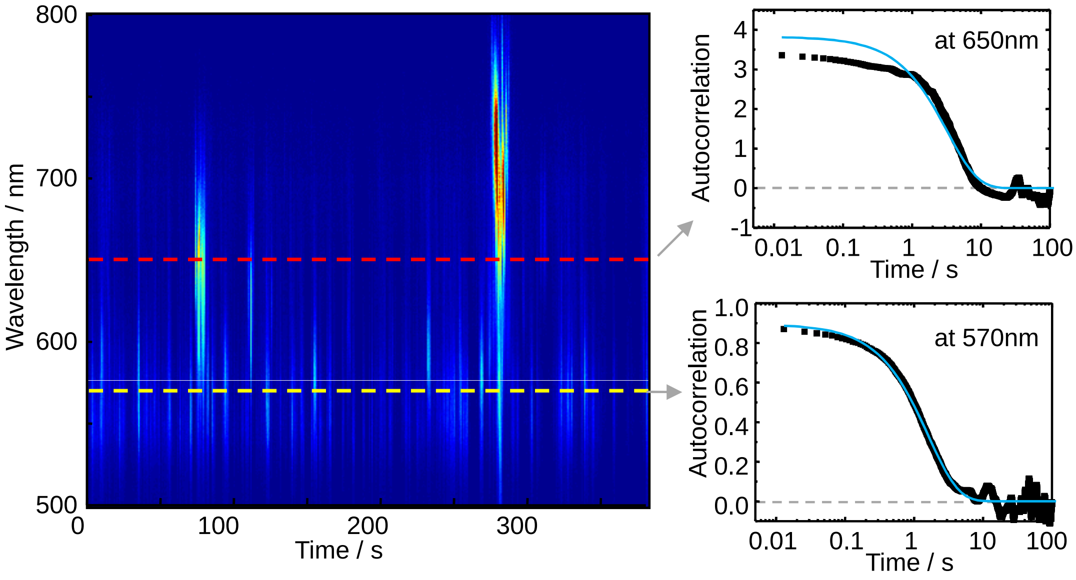

Figure 8.2: On the left, data typically measured to determine the autocorrelation time is presented. Intensity autocorrelation at 570 nm (yellow dashed line) gives a decay time of $\tau = (1.62 \pm 0.02)$ s and belongs to the diffusion of gold spheres. Intensity autocorrelation at 650 nm (red dashed line) results in a longer decay time of $\tau = (3.33 \pm 0.03)$ s which is originated by larger particles, e.g. rods or aggregates. The blue curves in the graphs on the right are the exponential fits.

a term for rotational diffusion can be avoided. Therefore, spherical particles are chosen.

BBInternational gold spheres are delivered at a concentration of $9{\cdot}10^{10}$ particles/ml for 40 nm spheres and $2.6{\cdot}10^{10}$ particles/ml for 60 nm spheres (data provided by the manufacturer). To obtain a good particle concentration the particles were centrifuged down, the supernatant was removed, and the pellet was filled up with a hundredth of the original volume with either water or glycerin. As exposure times 500 µs, 2 ms, and 10 ms were used. The normalized autocorrelation value measured at $\tau = 0$ s which is inverse to the mean number of particles in the effective volume is normally between 0.2 and 15. Thus, a mean number of 0.07-5 particles can be assumed to be in the effective volume.

Figure 8.2 shows on the left a behavior of the intensity typically measured over time. The respective autocorrelation function of two different wavelengths and their fits are presented on the right. Values measured are shown in Table 8.1. Additionally, the theoretical values were calculated. Therefore, the correlation time was approximated with Equation 8.1. A lateral radius of 500 nm for the volume of illumination was assumed. For all measurements, the magnitude of theoretical and experimental values agree (see Table 8.1). Deviations probably come from the rough approximation of the effective radius and the hindered Brownian motion due to the glass surface [196]. If glycerin was chosen as solvent some experimental challenges appeared. They are discussed later in this chapter under 'Challenges of the experiment'. Comparison of correlation times of differently sized particles in water shows the expected longer correlation time for bigger particles. Deviations between different exposure times were not further investigated, but might be attributed to refocusing, causing a change in the boundary condition of the effective volume.

To test if the different correlation times between the two solvents are reasonable, I have used Equation 8.2. The only difference between the two experiments is the different viscosity, η. Particle size and temperature are the same for both measurements. With the valid assumption of a well defined viscosity for water (1 mPas), I can calculate the viscosity in the glycerin experiment: Correlation times of 60 nm particles (12.5 ms in water, 1.5 s in glycerin) differ by a factor of 120. This results in the reasonable mixture of approximately 86 % glycerin and 14 % water for the high viscosity experiment (see Figure 7.9). A factor of 400 (5.25 ms in water, 2.1 s in glycerin) between the different viscosities of 40 nm spheres yields a 94 % glycerin and 6 % water mixture. The differences in mixing ratio seen for the two glycerin solutions can easily appear within different samples due to minor variations of supernatant removal.
Note, the correlation times presented are determined by autocorrelation of the intensity at 570 nm. This wavelength was chosen, as it is approximately the resonance position of spheres in glycerin. Interestingly, correlation times at 537 nm and 570 nm agree very well, as the plasmon shoulder is present at both wavelength. Whereas, correlation time at 650 nm (data not included in Table 8.1) is retarded compared to correlation times at 570 nm. An explanation is the contribution of mainly bigger particles or aggregates which scatter at these red wavelengths. Due to their higher spatial dimension the diffusion constant (see Equation 8.2) is lower. Furthermore, the autocorrelation is less well described by a single exponential decay as particle shapes are not defined (see Figure 8.2).

exposure time	40nm, water	60nm, water	40nm, glycerin	60nm, glycerin
500 µs	(2.5±0.5) ms	(12.7±1.5) ms	-	-
2 ms	(8±0.8) ms	(12.3±1.3) ms	(2.4±1.3) s	-
10 ms	-	-	(1.8±0.7) s	(1.5±0.2) s
theoretical	11 ms	17 ms	2.85 s	4.85 s

Table 8.1: Experimental and theoretical correlation times of Au spheres diffusing through the field of camera detection. The errors present the standard deviation of all respective measurements. The accuracy of the fit of the autocorrelation function is $R^2 > 0.95$.

Challenges of the experiment

Water has a lower viscosity than glycerin, therefore, shorter correlation times are expected. These are more difficult to be resolved with my setup. On the other hand, as viscosity of glycerin changes dramatically if a small amount of water is included, experiments in water do not suffer from the difficulty to reproduce exactly the same viscosity between different experiments. Also the steady state, when no more particle drift is induced by fluid flow, is reached much faster in the case of water.

8.3 Sensing volume of plasmonic rod as detection volume

The next step of plasmon correlation sensing uses the sensing volume of an immobilized particle as effective volume. As the sensing distance of a gold rod with a plasmon peak around 650 nm is in the order of 10 nm, the sensing volume is reduced down to zepto- to attoliters[20]. I remind the reader that the size of the sensing volume defines the concentration of the sample as only a small number of sample molecules should be present in parallel inside the sensing volume (see Section 8.1). Thus, the small sensing volume of a nanoparticle allows to increase the analyte density above nanomolar concentration, a value which can be found in real biological systems. Closely related experiments with diffusing dyes have been carried out before [197]. There, the expected drastic volume reduction, implementing access to higher analyte concentrations, was found. Nevertheless, dye diffusion suffers from disadvantages, e.g. distance dependent quenching, dye orientation dependence or even simple bleaching effects. In the here presented plasmon correlation sensing, these disadvantages do not occur.

Concept and theoretical investigation of feasibility

The concept of plasmon correlation sensing is the following: A diffusing particle or molecule which enters the sensing volume induces a resonance shift in the sensor. This shift is taken as signal, comparable to intensity changes in FCS.

To theoretically determine the quality or even only the feasibility of such a measurement I used the same method as for the signal-to-noise determination in Chapter 5. Prior to that, I chose the particle size of the diffuser and the viscosity of the solution as they were required for the signal-to-noise calculations but during which they are kept constant.

Particle size of the diffusers should be as large as possible to minimize the diffusion constant D which again maximizes the residence time, τ (see Figure 8.3, A detailed discussion on the residence time follows later in this section.), within the sensing volume (see Section 8.1). However, if the particles are so large that it is possible to easily see them diffusing under the microscope, they will contribute too much light to the signal. Their signal will simply add to the plasmon peak of the sensor, even if they are not in the sensing volume, but well above the sensing particle. Therefore, 10 nm diameter particles were chosen for the simulation.

---

[20] Side remark: This sensing volume is approximately as big as the volume of the rod.

Another parameter which influences the residence time is the viscosity. A **high viscosity** which is realized with glycerin further increases the average time how long the diffuser can be sensed by the particle.

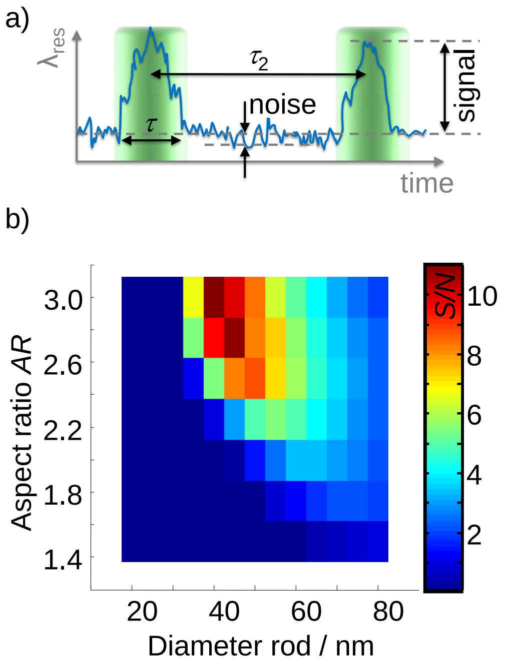

Figure 8.3: a) Parameter description of the plasmon correlation sensor. b) Signal-to-noise of differently sized plasmon correlation sensors. The simulations were carried out for 10 nm diffusing particles with a refractive index of 2.7, in 90 % glycerin solution, 50 µs exposure time and at room temperature.

The amount of **shift (signal)** induced to the sensor depends on size and material of the diffusing particle as well as on the dimensions of the sensor. Furthermore, it is influenced by the spatial position of the analyte within the sensing volume. However, due to reduction in complexity this position dependency is neglected for the determination of the signal-to-noise. Nevertheless, I remind the reader that diffusing particles at the tip of the sensor and in close proximity to the gold surface introduce the largest shift (see Section 5.2.4). Particles on a side of the sensor have a slightly smaller influence. As in Section 5.2.4, again QSA is used to calculate the highest shift induced by a diffuser.

To be able to calculate the signal-to-noise level, also the **noise** of the system has to be determined. This is done similar to the noise determination in Chapter 4 and 5. Briefly, ten thousand resonance spectra of an unperturbed sensor were acquired, each resonance position was determined and the standard deviation was taken as noise. I recapitulate from earlier findings, smaller exposure times and smaller particle sizes lead to higher noise (see Figure 4.4b). These noise terms measured were then compared to noise terms predicted by simulation (see Section 5.2.4) and found to be in reasonable agreement.

The respective **signal-to-noise** level for different sensor sizes is shown in Figure 8.3. As diffusing particles 10 nm spheres with a refractive index of 2.7 for titanium dioxide were used. Further parameters are a 90 % glycerin solution ($\eta = 219\,\mathrm{mPa\,s}$), 50 µs exposure time and room temperature.

An additional parameter which has to be considered for the feasibility of the experiment is the time during which this shift occurs - the **residence time**, τ (see Figure 8.3). As the sensing volume is tiny, the residence time is also really small. For a

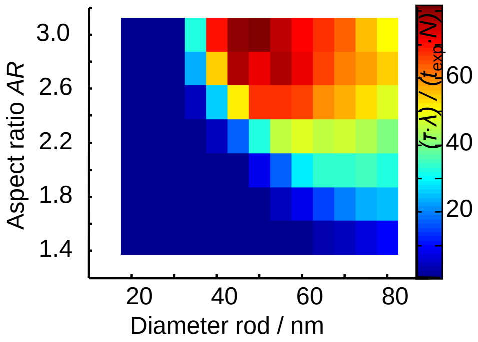

Figure 8.4: Altered signal-to-noise of differently sized plasmon correlation sensors. For the signal the shift is multiplied with the residence time and divided by the exposure time. Simulations were carried out for 10 nm diffusing particles with a refractive index of 2.7, in 90 % glycerin solution, 50 µs exposure time and at room temperature.

rough approximation, Equation 8.1 is taken, using the sensing distance of the particle as the effective radius [198]. For a 35 nm×78 nm rod, a distance of 11 nm can be assumed[21]. Thus, the resulting volume is one magnitude smaller than in the 'field of camera as detection volume' experiment. A new implementation of the signal for the signal-to-noise calculation, where the signal is used as multiplication of shift, residence time and inverse exposure time, slightly alters the optimal dimension for the sensor (see Figure 8.4). The calculated residence times are shown in Table 8.2. From these theoretical residence times, it is clear, that 'crop mode' has to be chosen for sufficient time resolution.

The last parameter which needs to be considered for the realization of an experiment is the time between events, the event repeatability, τ_2 (see Figure 8.3). This parameter is concentration dependent and can in theory be easily adapted to match any requirement. However, this parameter introduces some challenges in sample preparation. Methods to prepare the high concentrations needed, increase chances for aggregation which spoils the measurement.

particle diameter	5 nm	10 nm	40 nm	60 nm
water	0.7 µs	1.4 µs	5.5 µs	8.3 µs
glycerin	0.2 ms	0.3 ms	1.4 ms	2.1 ms

Table 8.2: Theoretical residence times of Au spheres diffusing through the sensing volume of the plasmonic particle. The viscosity of water is 1 mPa s and the value used for glycerin 250 mPa s.

Experiments

I tested a series of particles in water, even though calculated correlation times are expected to be smaller than the minimum time resolution of the setup. Slight errors of parameters assumed can push the theoretical correlation time into the detectable region above 50 µs. As diffusing particles I tested CdSe quantum dots (QD) with sizes of 7-10 nm and a fluorescence emission above 900 nm kindly provided by . These QDs had the

---

[21] This value was taken from calculations carried out by (see Section 5.2.4).

problem of immobilizing on the glass surfaces of the flow cell, increasing the background drastically.
The same problem appeared when seeds, normally used for gold rod production, were used. Here, an increase in the *FWHM* of the sensing particle as well as a blue shift were observed. These are indicators for attachment of the seeds to the sensing rod and do not allow a reliable measurement.
Furthermore, the possibility of using highly concentrated 15 nm gold spheres (remaining sample of) was tested. Here, too many aggregates were present and thus no measurement possible.
Carrying out the experiment in the presence of TiO_2 particles with an average diameter between 20-50 nm (provided by
and a concentration of about $4 \cdot 10^{14}$ particles/ml dispersed in pure glycerin did show the presence of strong scattering centers, probably remaining aggregates.

8.4 Conclusion

Plasmon correlation spectroscopy using the field of camera detection was demonstrated and I verified the general possibility to use the setup for such an experiment. However, similar setups got well established recently and provide an even better decay time analysis due to logarithmic scaling of the measurement time.
The assay to give the proof of principle with plasmon fluctuation sensing using the sensing volume of a single nanoparticle was not completed within this thesis. Reasons are probably correlation times at the edge of maximum setup time resolution and the need for even better spectral resolution. The experimental noise of the sensing rods is just slightly below the induced shift expected by simulations. To achieve plasmon fluctuation sensing with the current setup the following settings probably provide the best chances to succeed: 10 nm, high refractive index spheres dispersed in glycerin seem to be the most promising candidates. As sensor I propose a rod with a width of 50 nm and an aspect ratio above 2.6 but still with a resonance below 700 nm to be detectable.

Additional to the simulations presented in this chapter it seems straight forward to simulate an entire time trace. With such a time trace one can obtain an idea for the real shift expected and not only the maximum shift as investigated in this thesis is considered.

9 Summary

In conclusion, this thesis presents a successful improvement in time resolution and spectral resolution for plasmon spectra acquisition. The tremendous enhancement of the setup was demonstrated and used for a series of highly interesting experiments on single plasmonic nanostructures as sensors and is recalled in the following paragraphs.

I showed the possibility to use single functionalized nanoparticles as local pH-sensors for volumes on the nanoscale (see Chapter 3). To achieve this, gold nanorods were functionalized with a pH-responsive polymer layer. Depending on the pH the polymer chain stretched or coiled due to changes in its charging. This conformation change was accompanied by a refractive index change which induced a shift in the resonance wavelength of the sensing particle monitored in the microscope. Due to their small responsive volume in the attoliter regime these pH-sensitive nanoparticles can be used for precise pH-mapping without the disadvantage of bleaching or blinking as experienced for dye pH-sensors.

My 'home-built' setup, the plasmon fluctuation microscope, combines two major improvements compared to state of the art setups (see Chapter 4). They are the stronger light source, in the form of a white light laser, and the more sensitive detector. Thus, with this setup one can monitor particle spectra with a maximum time resolution of 50 µs, which is an advancement of approximately 4-6 orders of magnitude from previously available setups. Furthermore, the spectral stability of the setup is massively enhanced to prior stability and lies at about 0.03 nm. The maximum number of frames for data collection is about $4{\cdot}10^5$ so far limited by the capacity of the computer memory. Assuming a cycle time of 10 ms, this allows measurements for more than one hour.

The most outstanding achievements of this thesis show the attachment of single proteins onto individual nanoparticles as discrete jumps in the resonance wavelength (see Chapter 5) and thus a dramatic enhancement in plasmon nanoparticle sensitivity. Investigation of the step height and the times between events nicely matched values theoretically predicted. Also further control experiments analyzing the shift height dependence from protein size, protein desorption, Poissonian distribution of the arriving events, and systematic changes in step height with the number of proteins attached confirmed the hypothesis of single protein events.
Being able to detect single binding events with millisecond time resolution I could provide data from a time resolved protein adsorption event. The characteristic time scale obtained laid in the order of 1-2 s and probably resulted from the surface induced protein denaturation. In future experiments on series of modified proteins, this method will characterize sub-parts of proteins responsible for certain functions like binding, stability etc.
Furthermore, I measured the equilibrium adsorption and desorption of proteins

to the surface of the nanorod. By investigation of differences in fluctuations for different coverage conditions, information about binding kinetics will be retrievable. With this new method for the investigation of equilibrium dynamics a first step towards easily measuring binding constants was carried out.

Additionally, a system of two spherical nanoparticles connected via a spacer molecule, referred to as a dimer or nanoruler, was investigated (see Chapter 6). Here, the interesting effect of the particles' approach due to strong laser illumination was discussed. Parameters like the threshold power and the responsible wavelength regime were investigated. Furthermore, the reversibility of the collapse, orientation of the dimer relative to laser light and the influence of a temperature bath were explored. The results found could not pinpoint optical force or heating as exclusive mechanism responsible for the collapse of the dimer but rather suggested a combination of both. The collapse of the nanoruler under strong illumination rejects it as distance sensor in the Plasmon Fluctuation Setup but opens new areas of application like the construction of a light induced nanoshutter.

Also the possibility to use dimers as stiffness sensors for the interparticle spacer was studied (see Chapter 7). This nanosensor for stiffness would enter a regime of distance or strength so far not covered by methods commonly used. As only one particle of the dimer was immobilized to the glass surface of the sample chamber, the other particle moved due to Brownian motion. Of course, this movement should be strongly confined by the spacer stiffness and furthermore be influenced by the viscosity of the surrounding medium. Therefore, the secondary particle's position should hold information about the previously mentioned parameters. As the two particles of the dimer were in close proximity, their plasmons coupled, reporting on the current interparticle distance. Reading out this time dependence of the resonance wavelength and knowing the viscosity of the medium, one should be able to gather information about the spacer stiffness. Nevertheless, the slow distance fluctuations seen are not understood so far. Further experiments on a logarithmic time scale with even higher time resolution, more statistics, and additionally varied parameters are needed to achieve proof of principle results for determining stiffness by dimeric systems.

Another application for nanoparticles as sensors is closely related to fluorescence correlation spectroscopy with the difference that only the sensing volume of the nanoparticle is used as detection volume. Thus, unlabeled diffusing analytes at concentrations similar to those found in biological systems, which are too high for fluorescence correlation spectroscopy, can in principle be investigated. In Chapter 8, I presented my experiments in this field of research. So far, the proof of principle for this method was not completed, nevertheless a route for future experiments was outlined.

My work entered a new time regime for plasmon sensing. Time resolution down to 50 µs can now be achieved. With this improvement I enable spectra acquisition of unprecedented speed and quality. Thus, this thesis provides a base not only for further miniaturization of sensors but allows the new methodical principle of fluctuation sensing on equilibrium and non-equilibrium systems. With this fluctuation sensing the study of binding kinetics, interesting in a manifold number of areas, will be made easily accessible .

Appendix

A Synthesizing Gold Nanorods

Theoretically all metals, alloys or semiconductors which provide a dielectric function with a large negative real dielectric constant ($\epsilon'(\nu) \ll 0$) and a small imaginary dielectric constant ($\epsilon''(\nu) \approx 0$) exhibit a plasmon peak [125]. Nevertheless, the most common materials in our days are gold and silver as their resonance wavelength is in the visible regime and they are little reactive. Furthermore, well established wet-chemical methods for synthesizing these particles with a long term stability exist [199]. In the following I briefly describe the recipes used within this thesis. Gold nanorods are produced in a two step synthesis. The advantage of a two step synthesis over a one step one is a smaller polydispersity of the sample as only one seeding event occurs. The recipe for synthesizing big gold rods was kindly provided by .

A.1 Seed preparation

The general procedure for gold seeds with a size between 2 nm and 4 nm is as follows. Onto 50 µl of 0.1 M tetracholoauric acid ($HAuCl_4 \cdot 3H_2O$, Sigma) 5 ml of deionized water (throughout from a Millipore system with 18MΩ) and 5 ml of 0.2 M cetyltrimethylammonium bromide (CTAB, Sigma) solution was given. The gold was then reduced by the strong reducing agent sodium borohydride ($NaBH_4$, Sigma-Aldrich). Therefore, 600 µl of ice cold 0.02 M solution was added. The mixture was strongly shaken for 30 s and the seeds could be used within 15 min after preparation indicated by a strong brownish color. If stored for some time this color changed to red, indicating the aggregation and the seeds which could not be used anymore.

A.2 Gold rods

The actual gold rods were prepared in a second step, the growing step. Again 50 µl of 0.1 M tetrachloroauric acid was mixed with 5 ml of deionized water and 5 ml of 0.2 M CTAB solution. Additionally a small amount, normally around 5-20 µl, of silver nitrate (0.04M $AgNO_3$, Sigma-Aldrich) was added to the sample. Then, 70 µl of 0.0788 M ascorbic acid (Sigma-Aldrich) was added and caused the solution to turn colorless as ascorbic acid is a weak reduction agent. To this growth solution 12 µl of the before prepared gold seeds were given as nucleation centers where the reactions were started. The reaction could be followed by eye as the solution experienced a gradual color change from colorless to blue within minutes. Nevertheless, the rods continuously changed over larger time scales. The here given procedure results in rods around 650 nm resonance wavelength. Depending on the exact amounts of reagents a tuning of size and therefore resonance wavelength of the obtained rods is achieved. A more detailed description and analysis can be found elsewhere [167].

A.3 Medium gold rods

The gold rods used here with a medium particle volume were prepared with a slightly different growth. The 50 µl tetrachloroauric acid was mixed with 3848 µl deionized water and 5000 µl of 0.2 M CTAB solution. Additionally 1 ml of 0.25 M sodium chloride solution was added. The amount of silver nitrate was 20 µl at a concentration of 0.04 M. Then, 70 µl of 0.078 M ascorbic acid was added. The same seeds as for normal gold rods and the same amount were used: 12 µl. The medium rods used within this thesis were prepared about three years ago. During this time the sample was stored in the dark at room temperature. The resonance wavelength of the used sample was 635 nm and its average dimension 35 nm×78 nm.

A.4 Big gold rods

To prepare gold rods with a higher particle volume a slight variation of the normal growth solution was necessary. The tetrachloroauric acid was prepared with deionized water and CTAB solution as before. The amount of silver nitrate was altered to 20-50 µl with the same concentration of 0.04 M. Additionally 200 µl of 1 M hydrochloric acid (HCl, Merck) was added, followed by 80 µl of 0.1 M ascorbic acid. The before used seeds were diluted 1:10 with deionized water directly before adding 12.5 µl to the growth solution. The reaction was much slower compared to the one of normal rods, a color change could be observed the next day.

B Particle Functionalization

B.1 Particle functionalization for dimer preparation

B.1.1 Functionalization with PEG-biotin

Gold nanoparticle spheres were bought from BBInternational in diameters of 60 nm, 40 nm and 20 nm and used as bought. For functionalization with the two longer PEG spacers (PEG_{62}: $M_W = 3000$ g/mol and PEG_{108}: $M_W = 5000$ g/mol, Iris Biotech GmbH) a direct functionalization via the thiol end-group is possible. Therefore, 300 µl of the respective gold spheres were centrifuged down (5470 rcf, 5 min if not assigned differently this configuration was used for all further centrifugation steps) and the supernatant was removed. Then, 100 µl of 2 mM freshly prepared aqueous PEG solution was added. Incubation at room temperature for at least 2 hours on a shaking table was allowed. The excessive PEG was removed by adding 400 µl of deionized water (18 MΩ) and washing the sample with another centrifugation step. The functionalized particles are stored at 4°C and were stable for at least 1 month.

For the shortest PEG spacer used here (PEG_{10}: $M_W = 683$ g/mol, Iris Biotech GmbH) a slightly different procedure was necessary as the polymer carried an amino-group at the respective end. 200 µl of the gold spheres were centrifuged down and the supernatant was removed. Then, in a first functionalization step the particle was coated with 3,3'-Dithiobis (sulfosuccinimidylpropionate) (DTSSP, Pierce). Therefore, the resulting pellet was filled up with 100 µl freshly prepared 3 mg/ml aqueous DTSSP solution. The mixture was incubated for 20 min on the shaking table, filled up with 400 µl deionized water and then centrifuged down again. On the pellet 100 µl of 5 mM freshly prepared aqueous PEG solution was add, followed by a 1.5 hours incubation period on the shaking table. Removal of excessive PEG was achieved by another washing step via addition of 400 µl deionized water and centrifugation. The obtained pellet was filled up with 100 µl of 0.5x TRIS-Borat-EDTA-buffer (TBE, Roth) and stored at 4 °C until use within 1 month.

B.1.2 Functionalization with streptavidin

The streptavidin functionalization of gold nanospheres was achieved by first binding DTSSP to the protein. Therefore, 50 µl of 0.3 mM DTSSP was dissolved in phosphate buffered saline (PBS, 0.01 M, Sigma) and added to 50 µl of a 1 mg/ml streptavidin (Calbiochem) PBS solution. Incubation at room temperature for 30 min on the shaking table was allowed. In order to remove unreacted DTSSP a Zeba Spin Desalting Column 7K MWCO (Pierce) was used. In parallel 500 µl of sphere solution was centrifuged down. On the pellet 50 µl of the modified, desalted streptavidin solution was added and left for incubation over night at room temperate on the shaking table. To remove excessive proteins the sample was washed by adding 400 µl deionized water and centrifugation. Again the pellet was filled up with 25 µl deionized water. Storage at 4°C allowed a stability for maximal 1 month. Nevertheless, streptavidin functionalized particles were less stable then their biotin-functionalized opponent.

B.1.3 Conjugation buffer and passivation mixture

To obtain a surface passivation of the glass surface in the flow cell after immobilization of the first particle a passivation mixture was prepared. This passivation mixture contained 60 % SuperBlock (Pierce), 30 % deionized water and 10 % conjugation buffer (10 mM Tris-HCl pH 7.5, 10 mM EDTA, 2 M NaCl, 0.1 % Tween 20, all Sigma).

B.2 Elastin-like polypeptide functionalization

In contrast to the PEG dimerization, where the polymer linker was attached in batch, here the elastin-like polypeptide (ELP) was attached to the first immobilized sphere in the flow cell. Thus the flow cell was first washed extensively with pure water. Then 1 µl of as bought 60 nm citrate gold spheres was dispersed in

100 µl water and rinsed through the flow cell. To immobilize the particles 1 M NaCl was introduced, followed by an extensive washing step with pure water. Then, ELP solution was prepared by mixing 100 µl of 125 µM biotinilated E4-20 ELP, 3 µl of 100 mM TCEP, and 30 µl of 0.25x conjugation buffer. The E4-20 ELP was provided by
and biotinilated by .
The amino acid repetition sequence of ELP E4 is Val-Gly-Val-Pro-Gly. E4-20 has a molar weight of 8.4 kg/mol and includes 20 repeating units. This ELP solution was run for 30 s through the flow cell followed by a 45 min incubation period. These two steps were carried out twice. To avoid attachment of additional particles on the glass surface a passivation as in the PEG dimerization was performed: two cycles of 10 min flow and 30 min incubation with passivation mixture. Also the following dimerization step was similar to the PEG-dimer synthesis. Briefly, 1 µl stock solution of 60 nm streptavidin functionalized spheres is diluted in 100 µl passivation mixture was introduced into the flow cell. Dimerization was followed by eye and stopped after an appropriate number of dimers had formed.

C Technical Devices and Mathematical Tools

C.1 FastSPS dark field setup

The fastSPS setup is based on a standard transmission dark field microscope from Zeiss with a white light excitation from a 100 W tungsten lamp. Illumination occurred with a dark field condenser with high numerical aperture (NA 1.2-1.4). The sample in Chapter 3 was observed with a 63x water-immersion objective (NA 0.95 W) all other samples were investigated with a 40x air objective (NA 0.65). Furthermore, particle light is selected by a liquid crystal device (LC2002, Holoeye) used as an electronically addressable spatial shutter and detected with a CCD camera (Pixis400, Princeton Instruments). For spectral imaging, a spectrometer is coupled (SP-2150i, Acton; spectral resolution 1.6 nm). As the fastSPS setup can investigate a high number of particles in parallel, a feature so far not implemented at the Plasmon Fluctuation Setup, I used it to gain statistical information about samples and sample changes. Further information on the fastSPS setup can be found elsewhere [200, 201].

C.2 Fiber spectrometer

The fiber spectrometer used within this thesis was bought from Ocean Optics. The model is a USB2000 with a detection range between 350 nm and 1000 nm.

C.3 Autocorrelation function

The autocorrelation function tells the self-similarity or differently spoken the memory of the signal at different times t and $t+\tau$. The difference of the current signal to the mean signal, meaning the signal fluctuation $\delta F(t) = F(t) - < F >$, is multiplied to the signal fluctuation at another point in time $t + \tau$.

$$< \delta F(0) \cdot \delta F(\tau) > = < F(0) \cdot F(\tau) > - < F >^2 = < \delta A^2 > \exp \frac{-\tau}{\tau_r} \tag{C.1}$$

With the definition:

$$< F(0) \cdot F(\tau) > = \lim_{\mathrm{T}\to\infty} \frac{1}{\mathrm{T}} \int F(t)F(t+\tau)dt \tag{C.2}$$

At $\tau = 0$ the value of the autocorrelation function of the fluctuation is the square of the standard deviation. Thus a normalization with σ^2 gives values between -1 and 1, respectively for full correlation and anticorrelation. No correlation is presented by the value zero and normally reached in the limit of $\mathrm{T} \to \infty$.

In FCS if intensities are autocorrelated a different normalization is common. Here, normalization with the square of the mean value of the function $< F >^2$ is appropriate:

$$G(\tau) = \frac{< \delta F(t) \cdot \delta F(t+\tau) >}{< F >^2} = \frac{< F(t) \cdot F(t+\tau) >}{< F >^2} - 1 \tag{C.3}$$

With this normalization an additional information at $\tau = 0$ can be read out: $G(0)=1/N$.

References

[1] Stockman, M. I. (2011) Nanoplasmonics: The physics behind the applications. *Physics Today 64*, 39–44.

[2] Kneipp, J., Li, X. T., Sherwood, M., Panne, U., Kneipp, H., Stockman, M. I., and Kneipp, K. (2008) Gold nanolenses generated by laser ablation-efficient enhancing structure for surface enhanced Raman scattering analytics and sensing. *Analytical Chemistry 80*, 4247–4251.

[3] Polman, A. (2008) APPLIED PHYSICS Plasmonics Applied. *Science 322*, 868–869.

[4] Zijlstra, P., Chon, J. W. M., and Gu, M. (2009) Five-dimensional optical recording mediated by surface plasmons in gold nanorods. *Nature 459*, 410–413.

[5] Smith, D. R., Pendry, J. B., and Wiltshire, M. C. K. (2004) Metamaterials and negative refractive index. *Science 305*, 788–792.

[6] Liu, N., Guo, H., Fu, L., Kaiser, S., Schweizer, H., and Giessen, H. (2008) Three-dimensional photonic metamaterials at optical frequencies. *Nature Materials 7*, 31–37.

[7] Liu, N., Liu, H., Zhu, S., and Giessen, H. (2009) Stereometamaterials. *Nature Photonics 3*, 157–162.

[8] Liu, M., Zentgraf, T., Liu, Y. M., Bartal, G., and Zhang, X. (2010) Light-driven nanoscale plasmonic motors. *Nature Nanotechnology 5*, 570–573.

[9] Hasman, E. (2010) PLASMONICS New twist on nanoscale motors. *Nature Nanotechnology 5*, 563–564.

[10] Lal, S., Clare, S. E., and Halas, N. J. (2008) Nanoshell-Enabled Photothermal Cancer Therapy: Impending Clinical Impact. *Accounts of Chemical Research 41*, 1842–1851.

[11] Hartland, G. V. (2011) Optical Studies of Dynamics in Noble Metal Nanostructures. *Chemical Reviews 111*, 3858–3887.

[12] Giannini, V., Fernandez-Dominguez, A. I., Heck, S. C., and Maier, S. A. (2011) Plasmonic Nanoantennas: Fundamentals and Their Use in Controlling the Radiative Properties of Nanoemitters. *Chemical Reviews 111*, 3888–3912.

[13] Mayer, K. M., and Hafner, J. H. (2011) Localized Surface Plasmon Resonance Sensors. *Chemical Reviews 111*, 3828–3857.

[14] Ashcroft, D. N., Neil W.; Mermin *Festkörperphysik*; Oldenbourg Wissenschaftsverlag GmbH, 2007.

[15] Johnson, P. B., and Christy, R. W. (1972) Optical-constants of Noble-metals. *Physical Review B 6*, 4370–4379.

[16] Kittel, C. *Einführung in die Festkörperphysik*; Oldenbou, 2006.

[17] Maier, S. A. *Plasmonics Fundamentals and Applications*; Springer, 2007.

[18] Prescott, S. W., and Mulvaney, P. (2006) Gold nanorod extinction spectra. *Journal of Applied Physics 99*, 123504.

[19] Pecharroman, C., Perez-Juste, J., Mata-Osoro, G., Liz-Marzan, L. M., and Mulvaney, P. (2008) Redshift of surface plasmon modes of small gold rods due to their atomic roughness and end-cap geometry. *Physical Review B 77*, 035418.

[20] Yu, K. F., Kelly, K. L., Sakai, N., and Tatsuma, T. (2008) Morphologies and surface plasmon resonance properties of monodisperse bumpy gold nanoparticles. *Langmuir 24*, 5849–5854.

[21] Mulvaney, P., Perez-Juste, J., Giersig, M., Liz-Marzan, L. M., and Pecharroman, C. (2006) Drastic surface plasmon mode shifts in gold nanorods due to electron charging. *Plasmonics 1*, 61–66.

[22] Scaife, B. K. P. *Principles of Dielectrics*; Clarendon Press, Oxford, 1989.

[23] Kreibig, U., and Vollmer, M. *Optical Properties of Metal Clusters*; Springer, 1995.

[24] Jain, P. K., and El-Sayed, M. A. (2010) Plasmonic coupling in noble metal nanostructures. *Chemical Physics Letters 487*, 153–164.

[25] Hu, M., Novo, C., Funston, A., Wang, H. N., Staleva, H., Zou, S. L., Mulvaney, P., Xia, Y. N., and Hartland, G. V. (2008) Dark-field microscopy studies of single metal nanoparticles: understanding the factors that influence the linewidth of the localized surface plasmon resonance. *Journal of Materials Chemistry 18*, 1949–1960.

[26] Perez-Juste, J., Pastoriza-Santos, I., Liz-Marzan, L. M., and Mulvaney, P. (2005) Gold nanorods: Synthesis, characterization and applications. *Coordination Chemistry Reviews 249*, 1870–1901.

[27] Liu, M. Z., and Guyot-Sionnest, P. (2004) Synthesis and optical characterization of Au/Ag core/shell nanorods. *Journal of Physical Chemistry B 108*, 5882–5888.

[28] Raschke, G., Kowarik, S., Franzl, T., Sönnichsen, C., Klar, T. A., Feldmann, J., Nichtl, A., and Kurzinger, K. (2003) Biomolecular recognition based on single gold nanoparticle light scattering. *Nano Letters 3*, 935–938.

[29] Purcell, E. M., and Pennypac.CR, (1973) Scattering and Absorption of Light By Nonspherical Dielectric Grains. *Astrophysical Journal 186*, 705–714.

[30] Myroshnychenko, V., Rodriguez-Fernandez, J., Pastoriza-Santos, I., Funston, A. M., Novo, C., Mulvaney, P., Liz-Marzan, L. M., and de Abajo, F. J. G. (2008) Modelling the optical response of gold nanoparticles. *Chemical Society Reviews 37*, 1792–1805.

[31] Wriedt, T. (1998) A review of elastic light scattering theories. *Particle & Particle Systems Characterization 15*, 67–74.

[32] Trügler, A. Optical properties of metallic nanoparticles. Ph.D. thesis, Karl Franzens Universität Graz, 2011.

[33] Stewart, M. E., Anderton, C. R., Thompson, L. B., Maria, J., Gray, S. K., Rogers, J. A., and Nuzzo, R. G. (2008) Nanostructured plasmonic sensors. *Chemical Reviews 108*, 494–521.

[34] Khalavka, Y., Becker, J., and Sönnichsen, C. (2009) Synthesis of Rod-Shaped Gold Nanorattles with Improved Plasmon Sensitivity and Catalytic Activity. *Journal of the American Chemical Society 131*, 1871–1875, PMID: 19154114.

[35] Baciu, C. L., Becker, J., Janshoff, A., and Sönnichsen, C. (2008) Protein-Membrane Interaction Probed by Single Plasmonic Nanoparticles. *Nano Letters 8*, 1724–1728, PMID: 18459744.

[36] Willets, K. A., and Van Duyne, R. P. (2007) Localized surface plasmon resonance spectroscopy and sensing. *Annual Review of Physical Chemistry 58*, 267–297.

[37] Haes, A. J., and Van Duyne, R. P. (2002) A nanoscale optical biosensor: Sensitivity and selectivity of an approach based on the localized surface plasmon resonance spectroscopy of triangular silver nanoparticles. *Journal of the American Chemical Society 124*, 10596–10604.

[38] Jain, P. K., Huang, X., El-Sayed, I. H., and El-Sayad, M. A. (2007) Review of some interesting surface plasmon resonance-enhanced properties of noble metal nanoparticles and their applications to biosystems. *Plasmonics 2*, 107–118.

[39] Blaber, M. G., Arnold, M. D., Harris, N., Ford, M. J., and Cortie, M. B. (2007) Plasmon absorption in nanospheres: A comparison of sodium, potassium, aluminium, silver and gold. *Physica B-condensed Matter 394*, 184–187.

[40] Haes, A. J., and Van Duyne, R. P. (2003) Nanosensors enable portable detectors for environmental and medical applications. *Laser Focus World 39*, 153–156.

[41] Hao, E., and Schatz, G. C. (2004) Electromagnetic fields around silver nanoparticles and dimers. *Journal of Chemical Physics 120*, 357–366.

[42] Mirkin, C. A., Letsinger, R. L., Mucic, R. C., and Storhoff, J. J. (1996) A DNA-based method for rationally assembling nanoparticles into macroscopic materials. *Nature 382*, 607–609.

[43] Xia, F., Zuo, X. L., Yang, R. Q., Xiao, Y., Kang, D., Vallee-Belisle, A., Gong, X., Yuen, J. D., Hsu, B. B. Y., Heeger, A. J., and Plaxco, K. W. (2010) Colorimetric detection of DNA, small molecules, proteins, and ions using unmodified gold nanoparticles and conjugated polyelectrolytes. *Proceedings of the National Academy of Sciences of the United States of America 107*, 10837–10841.

[44] Rechberger, W., Hohenau, A., Leitner, A., Krenn, J. R., Lamprecht, B., and Aussenegg, F. R. (2003) Optical properties of two interacting gold nanoparticles. *Optics Communications 220*, 137–141.

[45] Su, K. H., Wei, Q. H., Zhang, X., Mock, J. J., Smith, D. R., and Schultz, S. (2003) Interparticle coupling effects on plasmon resonances of nanogold particles. *Nano Letters 3*, 1087–1090.

[46] Nordlander, P., Oubre, C., Prodan, E., Li, K., and Stockman, M. I. (2004) Plasmon hybridizaton in nanoparticle dimers. *Nano Letters 4*, 899–903.

[47] Prodan, E., Radloff, C., Halas, N. J., and Nordlander, P. (2003) A hybridization model for the plasmon response of complex nanostructures. *Science 302*, 419–422.

[48] Yang, S. C., Kobori, H., He, C. L., Lin, M. H., Chen, H. Y., Li, C. C., Kanehara, M., Teranishi, T., and Gwo, S. (2010) Plasmon Hybridization in individual Gold Nanocrystal Dimers: Direct Observation of Bright and Dark Modes. *Nano Letters 10*, 632–637.

[49] Gunnarsson, L., Rindzevicius, T., Prikulis, J., Kasemo, B., Kall, M., Zou, S. L., and Schatz, G. C. (2005) Confined plasmons in nanofabricated single silver particle pairs: Experimental observations of strong interparticle interactions. *Journal of Physical Chemistry B 109*, 1079–1087.

[50] Jain, P. K., Huang, W. Y., and El-Sayed, M. A. (2007) On the universal scaling behavior of the distance decay of plasmon coupling in metal nanoparticle pairs: A plasmon ruler equation. *Nano Letters 7*, 2080–2088.

[51] Maier, S. A., Brongersma, M. L., Kik, P. G., and Atwater, H. A. (2002) Observation of near-field coupling in metal nanoparticle chains using far-field polarization spectroscopy. *Physical Review B 65*, 193408/1–193408/4.

[52] Atay, T., Song, J. H., and Nurmikko, A. V. (2004) Strongly interacting plasmon nanoparticle pairs: From dipole-dipole interaction to conductively coupled regime. *Nano Letters 4*, 1627–1631.

[53] Romero, I., Aizpurua, J., Bryant, G. W., and de Abajo, F. J. G. (2006) Plasmons in nearly touching metallic nanoparticles: singular response in the limit of touching dimers. *Optics Express 14*, 9988–9999.

[54] Marhaba, S., Bachelier, G., Bonnet, C., Broyer, M., Cottancin, E., Grillet, N., Lerme, J., Vialle, J. L., and Pellarin, M. (2009) Surface Plasmon Resonance of Single Gold Nanodimers near the Conductive Contact Limit. *Journal of Physical Chemistry C 113*, 4349–4356.

[55] Madoyan, K., Melikyan, A., and Minassian, H. (2010) Semianalytical theory of plasmon nanoruler. *Applied Physics B-lasers and Optics 100*, 875–881.

[56] Sheikholeslami, S., Jun, Y. W., Jain, P. K., and Alivisatos, A. P. (2010) Coupling of Optical Resonances in a Compositionally Asymmetric Plasmonic Nanoparticle Dimer. *Nano Letters 10*, 2655–2660.

[57] Kottmann, J. P., and Martin, O. J. F. (2001) Retardation-induced plasmon resonances in coupled nanoparticles. *Optics Letters 26*, 1096–1098.

[58] Brown, L. V., Sobhani, H., Lassiter, J. B., Nordlander, P., and Halas, N. J. (2010) Heterodimers: Plasmonic Properties of Mismatched Nanoparticle Pairs. *Acs Nano 4*, 819–832.

[59] Mirin, N. A., Bao, K., and Nordlander, P. (2009) Fano Resonances in Plasmonic Nanoparticle Aggregates. *Journal of Physical Chemistry A 113*, 4028–4034.

[60] Yang, L. L., Yan, B., and Reinhard, B. M. (2008) Correlated Optical Spectroscopy and Transmission Electron Microscopy of Individual Hollow Nanoparticles and their Dimers. *Journal of Physical Chemistry C 112*, 15989–15996.

[61] Huang, F. M., and Baumberg, J. J. (2010) Actively Tuned Plasmons on Elastomerically Driven Au Nanoparticle Dimers. *Nano Letters 10*, 1787–1792.

[62] Ramakrishna, G., Dai, Q., Zou, J. H., Huo, Q., and Goodson, T. (2007) Interparticle electromagnetic coupling in assembled gold-necklace nanoparticles. *Journal of the American Chemical Society 129*, 1848–1849.

[63] Gluodenis, M., and Foss, C. A. (2002) The effect of mutual orientation on the spectra of metal nanoparticle rod-rod and rod-sphere pairs. *Journal of Physical Chemistry B 106*, 9484–9489.

[64] Tabor, C., Van Haute, D., and El-Sayed, M. A. (2009) Effect of Orientation on Plasmonic Coupling between Gold Nanorods. *Acs Nano 3*, 3670–3678.

[65] Funston, A. M., Novo, C., Davis, T. J., and Mulvaney, P. (2009) Plasmon Coupling of Gold Nanorods at Short Distances and in Different Geometries. *Nano Letters 9*, 1651–1658.

[66] Shao, L., Woo, K. C., Chen, H. J., Jin, Z., Wang, J. F., and Lin, H. Q. (2010) Angle- and Energy-Resolved Plasmon Coupling in Gold Nanorod Dimers. *Acs Nano 4*, 3053–3062.

[67] Baffou, G., Quidant, R., and de Abajo, F. J. G. (2010) Nanoscale Control of Optical Heating in Complex Plasmonic Systems. *Acs Nano 4*, 709–716.

[68] Ekici, O., Harrison, R. K., Durr, N. J., Eversole, D. S., Lee, M., and Ben-Yakar, A. (2008) Thermal analysis of gold nanorods heated with femtosecond laser pulses. *Journal of Physics D-applied Physics 41*, 185501.

[69] Volkov, A. N., Sevilla, C., and Zhigilei, L. V. (2007) Numerical modeling of short pulse laser interaction with Au nanoparticle surrounded by water. *Applied Surface Science 253*, 6394–6399.

[70] Link, S., and El-Sayed, M. A. (2001) Spectroscopic determination of the melting energy of a gold nanorod. *Journal of Chemical Physics 114*, 2362–2368.

[71] Zijlstra, P., Chon, J. W. M., and Gu, M. (2009) White light scattering spectroscopy and electron microscopy of laser induced melting in single gold nanorods. *Physical Chemistry Chemical Physics 11*, 5915–5921.

[72] Tang, B., An, J., Zheng, X. L., Xu, S. P., Li, D. M., Zhou, J., Zhao, B., and Xu, W. Q. (2008) Silver Nanodisks with Tunable Size by Heat Aging. *Journal of Physical Chemistry C 112*, 18361–18367.

[73] Huang, X. H., Jain, P. K., El-Sayed, I. H., and El-Sayed, M. A. (2006) Determination of the minimum temperature required for selective photothermal destruction of cancer cells with the use of immunotargeted gold nanoparticles. *Photochemistry and Photobiology 82*, 412–417.

[74] Sunderland, C. J., Steiert, M., Talmadge, J. E., Derfus, A. M., and Barry, S. E. (2006) Targeted nanoparticles for detecting and treating cancer. *Drug Development Research 67*, 70–93.

[75] Lukianova-Hleb, E. Y., Hanna, E. Y., Hafner, J. H., and Lapotko, D. O. (2010) Tunable plasmonic nanobubbles for cell theranostics. *Nanotechnology 21*, 085102.

[76] Govorov, A. O., Zhang, W., Skeini, T., Richardson, H., Lee, J., and Kotov, N. A. (2006) Gold nanoparticle ensembles as heaters and actuators: melting and collective plasmon resonances. *Nanoscale Research Letters 1*, 84–90.

[77] Lee, J., Govorov, A. O., and Kotov, N. A. (2005) Nanoparticle assemblies with molecular springs: A nanoscale thermometer. *Angewandte Chemie-international Edition 44*, 7439–7442.

[78] Richardson, H. H., Hickman, Z. N., Govorov, A. O., Thomas, A. C., Zhang, W., and Kordesch, M. E. (2006) Thermooptical properties of gold nanoparticles embedded in ice: Characterization of heat generation and melting. *Nano Letters 6*, 783–788.

[79] Eichler, H.-J. et al. In *Bergmann Schaefer, Lehrbuch der Experimentalphysik Band 3, Optik, Wellen- und Teilchenoptik*; Niedrig, H., Ed.; de Gruyter, 2004.

[80] Hecht, E. *Eugene Hecht, Optik*; Addison-Wesley Publishing Company, 1989.

[81] Volpe, G., Brettschneider, T., Helden, L., and Bechinger, C. (2009) Novel perspectives for the application of total internal reflection microscopy. *Optics Express 17*, 23975–23985.

[82] Choi, C. K., Margraves, C. H., and Kihm, K. D. (2007) Examination of near-wall hindered Brownian diffusion of nanoparticles: Experimental comparison to theories by Brenner (1961) and Goldman et al. (1967). *Physics of Fluids 19*, 103305.

[83] Hertlein, C., Riefler, N., Eremina, E., Wriedt, T., Eremin, Y., Helden, L., and Bechinger, C. (2008) Experimental verification of an exact evanescent light scattering model for TIRM. *Langmuir 24*, 1–4.

[84] Ashkin, A., Dziedzic, J. M., Bjorkhom, J. E., and Chu, S. (1986) Observation of A Single-beam Gradient Force Optical Trap For Dielectric Particles. *Optics Letters 11*, 288–290.

[85] Pelton, M., Liu, M. Z., Kim, H. Y., Smith, G., Guyot-Sionnest, P., and Scherer, N. E. (2006) Optical trapping and alignment of single gold nanorods by using plasmon resonances. *Optics Letters 31*, 2075–2077.

[86] Zelenina, A. S., Quidant, R., Badenes, G., and Nieto-Vesperinas, M. (2006) Tunable optical sorting and manipulation of nanoparticles via plasmon excitation. *Optics Letters 31*, 2054–2056.

[87] Arias-Gonzalez, J. R., and Nieto-Vesperinas, M. (2003) Optical forces on small particles: attractive and repulsive nature and plasmon-resonance conditions. *Journal of the Optical Society of America A-optics Image Science and Vision 20*, 1201–1209.

[88] Selhuber-Unkel, C., Zins, I., Schubert, O., Sönnichsen, C., and Oddershede, L. B. (2008) Quantitative optical trapping of single gold nanorods. *Nano Letters 8*, 2998–3003.

[89] Singer, W., Nieminen, T. A., Gibson, U. J., Heckenberg, N. R., and Rubinsztein-Dunlop, H. (2006) Orientation of optically trapped nonspherical birefringent particles. *Physical Review E 73*, 021911.

[90] Tong, L. M., Miljkovic, V. D., and Kall, M. (2010) Alignment, Rotation, and Spinning of Single Plasmonic Nanoparticles and Nanowires Using Polarization Dependent Optical Forces. *Nano Letters 10*, 268–273.

[91] Guffey, M. J., and Scherer, N. F. (2010) All-Optical Patterning of Au Nanoparticles on Surfaces Using Optical Traps. *Nano Letters 10*, 4302–4308.

[92] Krishnan, M., Mojarad, N., Kukura, P., and Sandoghdar, V. (2010) Geometry-induced electrostatic trapping of nanometric objects in a fluid. *Nature 467*, 692–U75.

[93] Urban, A. S., Lutich, A. A., Stefani, F. D., and Feldmann, J. (2010) Laser Printing Single Gold Nanoparticles. *Nano Letters 10*, 4794–4798.

[94] Dienerowitz, M., Mazilu, M., and Dholakia, K. (2008) Optical manipulation of nanoparticles: a review. *Journal of Nanophotonics 2*, 021875.

[95] Svoboda, K., and Block, S. M. (1994) Optical Trapping of Metallic Rayleigh Particles. *Optics Letters 19*, 930–932.

[96] Seol, Y., Carpenter, A. E., and Perkins, T. T. (2006) Gold nanoparticles: enhanced optical trapping and sensitivity coupled with significant heating. *Optics Letters 31*, 2429–2431.

[97] Hallock, A. J., Redmond, P. L., and Brus, L. E. (2005) Optical forces between metallic particles. *Proceedings of the National Academy of Sciences of the United States of America 102*, 1280–1284.

[98] Chu, P., and Mills, D. L. (2007) Laser-induced forces in metallic nanosystems: The role of plasmon resonances. *Physical Review Letters 99*, 127401.

[99] Sepulveda, B., Alegret, J., and Kall, M. (2007) Nanometric control of the distance between plasmonic nanoparticles using optical forces. *Optics Express 15*, 14914–14920.

[100] Svedberg, F., Li, Z. P., Xu, H. X., and Kall, M. (2006) Creating hot nanoparticle pairs for surface-enhanced Raman spectroscopy through optical manipulation. *Nano Letters 6*, 2639–2641.

[101] Ohlinger, A., Nedev, S., Lutich, A. A., and Feldmann, J. (2011) Optothermal Escape of Plasmonically Coupled Silver Nanoparticles from a Three-Dimensional Optical Trap. *Nano Letters 11*, 1770–1774.

[102] Tong, L., Miljkovic, V. D., Johansson, P., and Kall, M. (2010) Plasmon Hybridization Reveals the Interaction between Individual Colloidal Gold Nanoparticles Confined in an Optical Potential Well. *Nano Letters* DOI: 10.1021/nl1036116.

[103] Miljkovic, V. D., Pakizeh, T., Sepulveda, B., Johansson, P., and Kall, M. (2010) Optical Forces in Plasmonic Nanoparticle Dimers. *Journal of Physical Chemistry C 114*, 7472–7479.

[104] Zhang, W. H., Huang, L. N., Santschi, C., and Martin, O. J. F. (2010) Trapping and Sensing 10 nm Metal Nanoparticles Using Plasmonic Dipole Antennas. *Nano Letters 10*, 1006–1011.

[105] Atkin, R., Bradley, M., and Vincent, B. (2005) Core-shell particles having silica cores and pH-responsive poly(vinylpyridine) shells. *Soft Matter 1*, 160–165.

[106] Liu, H., Li, C. H., Liu, H. W., and Liu, S. Y. (2009) pH-Responsive Supramolecular Self-Assembly of Well-Defined Zwitterionic ABC Miktoarm Star Terpolymers. *Langmuir 25*, 4724–4734.

[107] Van Butsele, K., Fustin, C. A., Gohy, J. F., Jerome, R., and Jerome, C. (2009) Self-Assembly and pH-Responsiveness of ABC Miktoarm, Star Terpolymers. *Langmuir 25*, 107–111.

[108] Jacques, V., Murray, J. D., Marquier, F., Chauvat, D., Grosshans, F., Treussart, F., and Roch, J. F. (2008) Enhancing single-molecule photostability by optical feedback from quantum jump detection. *Applied Physics Letters 93*, 203307.

[109] Jain, P. K., Lee, K. S., El-Sayed, I. H., and El-Sayed, M. A. (2006) Calculated absorption and scattering properties of gold nanoparticles of different size, shape, and composition: Applications in biological imaging and biomedicine. *Journal of Physical Chemistry B 110*, 7238–7248.

[110] Portney, N. G., and Ozkan, M. (2006) Nano-oncology: drug delivery, imaging, and sensing. *Analytical and Bioanalytical Chemistry 384*, 620–630.

[111] Aili, D., Enander, K., Baltzer, L., and Liedberg, B. (2008) Assembly of polypeptide-functionalized gold nanoparticles through a heteroassociation- and folding-dependent bridging. *Nano Letters 8*, 2473–2478.

[112] Chen, Y., and Mao, C. D. (2008) pH-Induced Reversible Expansion/Contraction of Gold Nanoparticle Aggregates. *Small 4*, 2191–2194.

[113] Pastoriza-Santos, I., Gomez, D., Perez-Juste, J., Liz-Marzan, L. M., and Mulvaney, P. (2004) Optical properties of metal nanoparticle coated silica spheres: a simple effective medium approach. *Physical Chemistry Chemical Physics 6*, 5056–5060.

[114] Zhang, M. M., Liu, L., Zhao, H. Y., Yang, Y., Fu, G. Q., and He, B. L. (2006) Double-responsive polymer brushes on the surface of colloid particles. *Journal of Colloid and Interface Science 301*, 85–91.

[115] Nuopponen, M., and Tenhu, H. (2007) Gold nanoparticles protected with pH and temperature-sensitive diblock copolymers. *Langmuir 23*, 5352–5357.

[116] Li, D. X., He, Q., Cui, Y., and Li, J. B. (2007) Fabrication of pH-responsive nanocomposites of gold nanoparticles/poly(4-vinylpyridine). *Chemistry of Materials 19*, 412–417.

[117] Sarkar, D., and Somasundaran, P. (2004) Conformational dynamics of poly(acrylic acid). A study using surface plasmon resonance spectroscopy. *Langmuir 20*, 4657–4664.

[118] Reith, D., Muller, B., Muller-Plathe, F., and Wiegand, S. (2002) How does the chain extension of poly (acrylic acid) scale in aqueous solution? A combined study with light scattering and computer simulation. *Journal of Chemical Physics 116*, 9100–9106.

[119] Adamczyk, Z., Bratek, A., Jachimska, B., Jasinski, T., and Warszynski, P. (2006) Structure of poly(acrylic acid) in electrolyte solutions determined from simulations and viscosity measurements. *Journal of Physical Chemistry B 110*, 22426–22435.

[120] Williams, A., and Ibrahim, I. T. (1981) Carbodiimide Chemistry - Recent Advances. *Chemical Reviews 81*, 589–636.

[121] Pierrat, S., Hartinger, E., Faiss, S., Janshoff, A., and Soennichsen, C. (2009) Rotational Dynamics of Laterally Frozen Nanoparticles Specifically Attached to Biomembranes. *Journal of Physical Chemistry C 113*, 11179–11183.

[122] Person, S., Deutsch, B., Mitra, A., and Novotny, L. (2011) Material-Specific Detection and Classification of Single Nanoparticles. *Nano Letters 11*, 257–261.

[123] Curry, A., Nusz, G., Chilkoti, A., and Wax, A. (2007) Analysis of total uncertainty in spectral peak measurements for plasmonic nanoparticle-based biosensors. *Applied Optics 46*, Opt Soc Amer.

[124] Zayats, A. V., Smolyaninov, I. I., and Maradudin, A. A. (2005) Nano-optics of surface plasmon polaritons. *Physics Reports-review Section of Physics Letters 408*, 131–314.

[125] Anker, J. N., Hall, W. P., Lyandres, O., Shah, N. C., Zhao, J., and Van Duyne, R. P. (2008) Biosensing with plasmonic nanosensors. *Nature Materials 7*, 442–453.

[126] Hall, W. P., Modica, J., Anker, J., Lin, Y., Mrksich, M., and Van Duynet, R. P. (2011) A Conformation-and Ion-Sensitive Plasmonic Biosensor. *Nano Letters 11*, 1098–1105.

[127] Dahlin, A. B., Tegenfeldt, J. O., and Hook, F. (2006) Improving the instrumental resolution of sensors based on localized surface plasmon resonance. *Analytical Chemistry 78*, 4416–4423.

[128] Gerion, D., and Day, G. J. (2010) Label-Free and Labeled Technology for Protein Characterization and Quantitation. *Biopharm International 23*, 38.

[129] McFarland, A. D., and Van Duyne, R. P. (2003) Single silver nanoparticles as real-time optical sensors with zeptomole sensitivity. *Nano Letters 3*, 1057–1062.

[130] Liu, G. L., Yin, Y. D., Kunchakarra, S., Mukherjee, B., Gerion, D., Jett, S. D., Bear, D. G., Gray, J. W., Alivisatos, A. P., Lee, L. P., and Chen, F. Q. F. (2006) A nanoplasmonic molecular ruler for measuring nuclease activity and DNA footprinting. *Nature Nanotechnology 1*, 47–52.

[131] Liu, N., Tang, M. L., Hentschel, M., Giessen, H., and Alivisatos, A. P. (2011) Nanoantenna-enhanced gas sensing in a single tailored nanofocus. *Nat Mater 10*, 631–636.

[132] Alivisatos, P. (2004) The use of nanocrystals in biological detection. *Nature Biotechnology 22*, 47–52.

[133] Larsson, E. M., Alegret, J., Kall, M., and Sutherland, D. S. (2007) Sensing characteristics of NIR localized surface plasmon resonances in gold nanorings for application as ultrasensitive biosensors. *Nano Letters 7*, 1256–1263.

[134] Nusz, G. J., Marinakos, S. M., Curry, A. C., Dahlin, A., Hook, F., Wax, A., and Chilkoti, A. (2008) Label-free plasmonic detection of biomolecular binding by a single gold nanorod. *Analytical Chemistry 80*, 984–989.

[135] Sannomiya, T., Hafner, C., and Voros, J. (2008) In situ Sensing of Single Binding Events by Localized Surface Plasmon Resonance. *Nano Letters 8*, 3450–3455.

[136] Eigen, M., and Rigler, R. (1994) Sorting Single Molecules - Application To Diagnostics and Evolutionary Biotechnology. *Proceedings of the National Academy of Sciences of the United States of America 91*, 5740–5747.

[137] Chen, S., Svedendahl, M., Van Duyne, R. P., and Kall, M. (2011) Plasmon-Enhanced Colorimetric ELISA with Single Molecule Sensitivity. *Nano Letters 11*, 1826–1830.

[138] Armani, A. M., Kulkarni, R. P., Fraser, S. E., Flagan, R. C., and Vahala, K. J. (2007) Label-free, single-molecule detection with optical microcavities. *Science 317*, 783–787.

[139] Vollmer, F., and Arnold, S. (2008) Whispering-gallery-mode biosensing: label-free detection down to single molecules. *Nature Methods 5*, 591–596.

[140] Nie, S. M., and Emery, S. R. (1997) Probing single molecules and single nanoparticles by surface-enhanced Raman scattering. *Science 275*, 1102–1106.

[141] Sorgenfrei, S., Chiu, C. Y., Gonzalez, R. L., Yu, Y. J., Kim, P., Nuckolls, C., and Shepard, K. L. (2011) Label-free single-molecule detection of DNA-hybridization kinetics with a carbon nanotube field-effect transistor. *Nature Nanotechnology 6*, 125–131.

[142] Cui, Y., Wei, Q. Q., Park, H. K., and Lieber, C. M. (2001) Nanowire nanosensors for highly sensitive and selective detection of biological and chemical species. *Science 293*, 1289–1292.

[143] Acimovic, S. S., Kreuzer, M. P., Gonzalez, M. U., and Quidant, R. (2009) Plasmon Near-Field Coupling in Metal Dimers as a Step toward Single-Molecule Sensing. *Acs Nano 3*, 1231–1237.

[144] Becker, J., Trügler, A., Jakab, A., Hohenester, U., and Sönnichsen, C. (2010) The Optimal Aspect Ratio of Gold Nanorods for Plasmonic Bio-sensing. *Plasmonics 5*, 161–167.

[145] Mayer, K. M., Hao, F., Lee, S., Nordlander, P., and Hafner, J. H. (2010) A single molecule immunoassay by localized surface plasmon resonance. *Nanotechnology 21*, 255503.

[146] Mosher, D. F., and Furcht, L. T. (1981) Fibronectin - Review of Its Structure and Possible Functions. *Journal of Investigative Dermatology 77*, 175–180.

[147] Hemmersam, A. G., Rechendorff, K., Foss, M., Sutherland, D. S., and Besenbacher, F. (2008) Fibronectin adsorption on gold, Ti-, and Ta-oxide investigated by QCM-D and RSA modelling. *Journal of Colloid and Interface Science 320*, 110–116.

[148] Dolatshahi-Pirouz, A., Jensen, T., Foss, M., Chevallier, J., and Besenbacher, F. (2009) Enhanced Surface Activation of Fibronectin upon Adsorption on Hydroxyapatite. *Langmuir 25*, 2971–2978.

[149] Yu, Q. M., Chen, S. F., Taylor, A. D., Homola, J., Hock, B., and Jiang, S. Y. (2005) Detection of low-molecular-weight domoic acid using surface plasmon resonance sensor. *Sensors and Actuators B-chemical 107*, 193–201.

[150] Liu, J., and Messow, U. (2000) Diffusion-controlled adsorption kinetics at the air/solution interface. *Colloid and Polymer Science 278*, 124–129.

[151] Koteliansky, V. E., Glukhova, M. A., Benjanian, M. V., Smirnov, V. N., Filimonov, V. V., Zalite, O. M., and Venyaminov, S. Y. (1981) A Study of the Structure of Fibronectin. *European Journal of Biochemistry 119*, 619–624.

[152] Guemouri, L., Ogier, J., Zekhnini, Z., and Ramsden, J. J. (2000) The architecture of fibronectin at surfaces. *Journal of Chemical Physics 113*, 8183–8186.

[153] Anand, G., Sharma, S., Dutta, A. K., Kumar, S. K., and Belfort, G. (2010) Conformational Transitions of Adsorbed Proteins on Surfaces of Varying Polarity. *Langmuir 26*, 10803–10811.

[154] Karlsson, M., Ekeroth, J., Elwing, H., and Carlsson, U. (2005) Reduction of irreversible protein adsorption on solid surfaces by protein engineering for increased stability. *Journal of Biological Chemistry 280*, 25558–25564.

[155] Luthgens, E., and Janshoff, A. (2005) Equilibrium coverage fluctuations: A new approach to quantify reversible adsorption of proteins. *Chemphyschem 6*, 444–448.

[156] Rosengarth, A., Gerke, V., and Luecke, H. (2001) X-ray structure of full-length annexin 1 and implications for membrane aggregation. *Journal of Molecular Biology 306*, 489–498.

[157] Faiss, S., Kastl, K., Janshoff, A., and Steinem, C. (2008) Formation of irreversibly bound annexin AI protein domains on POPC/POPS solid supported membranes. *Biochimica Et Biophysica Acta-biomembranes 1778*, 1601–1610.

[158] Kastl, K., Ross, M., Gerke, V., and Steinem, C. (2002) Kinetics and thermodynamics of annexin A1 binding to solid-supported membranes: A QCM study. *Biochemistry 41*, 10087–10094.

[159] Kastl, K., Menke, M., Luthgens, E., Faiss, S., Gerke, V., Janshoff, A., and Steinem, C. (2006) Partially reversible adsorption of annexin A1 on POPC/POPS bilayers investigated by QCM measurements, SFM, and DMC simulations. *Chembiochem 7*, 106–115.

[160] Jares-Erijman, E. A., and Jovin, T. M. (2003) FRET imaging. *Nature Biotechnology 21*, 1387–1395.

[161] Sönnichsen, C., Reinhard, B. M., Liphardt, J., and Alivisatos, A. P. (2005) A molecular ruler based on plasmon coupling of single gold and silver nanoparticles. *Nat Biotech 23*, 741–745.

[162] Reinhard, B. M., Sheikholeslami, S., Mastroianni, A., Alivisatos, A. P., and Liphardt, J. (2007) Use of plasmon coupling to reveal the dynamics of DNA bending and cleavage by single EcoRV restriction enzymes. *Proceedings of the National Academy of Sciences of the United States of America 104*, 2667–2672.

[163] Rong, G. X., Wang, H. Y., and Reinhard, B. M. (2010) Insights from a Nanoparticle Minuet: Two-Dimensional Membrane Profiling through Silver Plasmon Ruler Tracking. *Nano Letters 10*, 230–238.

[164] Lubitz, I., and Kotlyar, A. (2011) Self-Assembled G4-DNA-Silver Nanoparticle Structures. *Bioconjugate Chemistry 22*, 482–487.

[165] Haynes, C. L., and Van Duyne, R. P. (2001) Nanosphere lithography: A versatile nanofabrication tool for studies of size-dependent nanoparticle optics. *Journal of Physical Chemistry B 105*, 5599–5611.

[166] Wong, J., Chilkoti, A., and Moy, V. T. (1999) Direct force measurements of the streptavidin-biotin interaction. *Biomolecular Engineering 16*, 45–55.

[167] Zins, I. Plasmonic Nanorods and Nanoparticle-Assemblies - Synthesis, Characterization, and Usage as Sensors. Ph.D. thesis, Johannes Gutenberg Universität Mainz, 2011.

[168] Anzai, J., Kobayashi, Y., and Takeshita, H. (1997) Enzyme multilayer-modified biosensors. Use of streptavidin and deglycosylated avidin for constructing glucose oxidase and lactate oxidase multilayers. *Analytical Sciences 13*, 859–861.

[169] Hu, P., Tanii, T., Zhang, G. J., Hosaka, T., and Ohdomari, I. (2007) Ultrasensitive detection of biomolecules using functionalized multi-walled carbon nanotubes. *Sensors and Actuators B-chemical 124*, 161–166.

[170] Kawaguchi, S., Imai, G., Suzuki, J., Miyahara, A., and Kitano, T. (1997) Aqueous solution properties of oligo- and poly(ethylene oxide) by static light scattering and intrinsic viscosity. *Polymer 38*, 2885–2891.

[171] Devanand, K., and Selser, J. C. (1991) Asymptotic-behavior and Long-range Interactions In Aqueous-solutions of Poly(ethylene Oxide). *Macromolecules 24*, 5943–5947.

[172] Jeppesen, C., Wong, J. Y., Kuhl, T. L., Israelachvili, J. N., Mullah, N., Zalipsky, S., and Marques, C. M. (2001) Impact of polymer tether length on multiple ligand-receptor bond formation. *Science 293*, 465–468.

[173] Ha, T., Enderle, T., Ogletree, D. F., Chemla, D. S., Selvin, P. R., and Weiss, S. (1996) Probing the interaction between two single molecules: Fluorescence resonance energy transfer between a single donor and a single acceptor. *Proceedings of the National Academy of Sciences of the United States of America 93*, 6264–6268.

[174] Jeschke, G. (2002) Distance measurements in the nanometer range by pulse EPR. *Chemphyschem 3*, 927–932.

[175] van Mameren, J., Vermeulen, K. C., Gittes, F., and Schmidt, C. F. (2009) Leveraging Single Protein Polymers To Measure Flexural Rigidity. *Journal of Physical Chemistry B 113*, 3837–3844.

[176] Butt, H. J., Cappella, B., and Kappl, M. (2005) Force measurements with the atomic force microscope: Technique, interpretation and applications. *Surface Science Reports 59*, 1–152.

[177] Flügel, S. Oligodeoxynucleotide-Polypeptide Block Copolymers. Ph.D. thesis, Johannes Gutenberg Universität Mainz, 2010.

[178] Bruus, H. *Theoretical Microfluidics*; Oxford Press, 2008.

[179] Reichl, L. E. *A Modern Course in Statistical Physics*; Wiley-Interscience, 1998.

[180] Viscosity of Aqueous Glycerine Solutions & Refractive Index. The Dow Chemical Company: http:
www.dow.com.

[181] Anne, A., Demaille, C., and Moiroux, J. (2002) Terminal attachment of polyethylene glycol (PEG) chains to a gold electrode surface. Cyclic voltammetry applied to the quantitative characterization of the flexibility of the attached PEG chains and of their penetration by mobile PEG chains. *Macromolecules 35*, 5578–5586.

[182] Maaloum, M., and Courvoisier, A. (1999) Elasticity of single polymer chains. *Macromolecules 32*, 4989–4992.

[183] Rubinstein, R. H., Michael ; Colby *Polymer Physics*; Oxford University Press, 2003.

[184] Thompson, N. L., Burghardt, T. P., and Axelrod, D. (1981) Measuring Surface Dynamics of Biomolecules By Total Internal-reflection Fluorescence With Photobleaching Recovery Or Correlation Spectroscopy. *Biophysical Journal 33*, 435–454.

[185] Krichevsky, O., and Bonnet, G. (2002) Fluorescence correlation spectroscopy: the technique and its applications. *Reports On Progress In Physics 65*, 251–297.

[186] Medina, M. A., and Schwille, P. (2002) Fluorescence correlation spectroscopy for the detection and study of single molecules in Biology. *Bioessays 24*, 758–764.

[187] Schwille, P. (2001) Fluorescence correlation spectroscopy and its potential for intracellular applications. *Cell Biochemistry and Biophysics 34*, 383–408.

[188] Berne, R., Bruce J.; Pecora *Dynamic Light Scattering With Applications to Chemistry, Biology, and Physics*; Dover Publications, Inc., 2000.

[189] Brenner, H. (1961) The Slow Motion of A Sphere Through A Viscous Fluid Towards A Plane Surface. *Chemical Engineering Science 16*, 242–251.

[190] Goldman, A. J., Cox, R. G., and Brenner, H. (1967) Slow Viscous Motion of A Sphere Parallel To A Plane Wall .i. Motion Through A Quiescent Fluid. *Chemical Engineering Science 22*, 637–651.

[191] Kihm, K. D., Banerjee, A., Choi, C. K., and Takagi, T. (2004) Near-wall hindered Brownian diffusion of nanoparticles examined by three-dimensional ratiometric total internal reflection fluorescence microscopy (3-D R-TIRFM). *Experiments In Fluids 37*, 811–824.

[192] Holmqvist, P., Dhont, J. K. G., and Lang, P. R. (2006) Anisotropy of Brownian motion caused only by hydrodynamic interaction with a wall. *Physical Review E 74*, 021402.

[193] Starr, T. E., and Thompson, N. L. (2001) Total internal reflection with fluorescence correlation spectroscopy: Combined surface reaction and solution diffusion. *Biophysical Journal 80*, 1575–1584.

[194] Levene, M. J., Korlach, J., Turner, S. W., Foquet, M., Craighead, H. G., and Webb, W. W. (2003) Zero-mode waveguides for single-molecule analysis at high concentrations. *Science 299*, 682–686.

[195] Lieto, A. M., and Thompson, N. L. (2004) Total internal reflection with fluorescence correlation spectroscopy: Nonfluorescent competitors. *Biophysical Journal 87*, 1268–1278.

[196] Leutenegger, M., Gosch, M., Perentes, A., Hoffmann, P., Martin, O. J. F., and Lasser, T. (2006) Confining the sampling volume for Fluorescence Correlation Spectroscopy using a sub-wavelength sized aperture. *Optics Express 14*, 956–969.

[197] Wang, Q., Lu, G., Hou, L., Zhang, T., Luo, C., Yang, H., Barbillon, G., Lei, F. H., Marquette, C. A., Perriat, P., Tillement, O., Roux, S., Ouyang, Q., and Gong, Q. (2011) Fluorescence correlation spectroscopy near individual gold nanoparticle. *Chemical Physics Letters 503*, 256–261.

[198] Estrada, L. C., Aramendia, P. F., and Martinez, O. E. (2008) 10000 times volume reduction for fluorescence correlation spectroscopy using nano-antennas. *Optics Express 16*, 20597–20602.

[199] Nikoobakht, B., and El-Sayed, M. A. (2003) Preparation and growth mechanism of gold nanorods (NRs) using seed-mediated growth method. *Chemistry of Materials 15*, 1957–1962.

[200] Becker, J., Schubert, O., and Sönnichsen, C. (2007) Gold nanoparticle growth monitored in situ using a novel fast optical single-particle spectroscopy method. *Nano Letters 7*, 1664–1669.

[201] Becker, J. Plasmons as Sensors. Ph.D. thesis, Johannes Gutenberg Universität Mainz, 2010.

Acknowledgments

As a thesis cannot be achieved without the help of others, this is now the moment to say thanks to several people:

[Removed to protect privacy]

Curriculum Vitae

[personal data removed]

List of Publications

- **'Influence of spatial structure on the maintenance of sexual reproduction'**
  I. Ament, S. Scheu, B. Drossel
  Journal of Theoretical Biology, (2008), Vol. 254, Pages 520-528

- **'Au@MnO Nanoflowers: Hybrid Nanocomposites for Selective Dual Functionalization and Imaging'**
  T. D. Schladt, M. I. Shukoor, K. Schneider, M. N. Tahir, F. Natalio, I. Ament, J. Becker, F. D. Jochum, S. Weber, O. Köhler, P. Theato, L. M. Schreiber, C. Sönnichsen, H. C. Schröder, W. E. G. Müller, W. Tremel
  Angewandte Chemie - International Edition, (2010), Vol. 49, Pages 3976-3980

- **'Phase separated Cu@Fe_3O_4 heterodimer nanoparticles from organometallic reactants'**
  B. Nakhjavan, M. N. Tahir, F. Natalio, HT. Gao, K. Schneider, T. Schladt, I. Ament, R. Branscheid, S. Weber, U. Kolb, C. Sönnichsen, L. M. Schreiber, W. Tremel
  Journal of Materials Chemistry, (2011), Vol. 21, Pages 8605-8611

- **'Nanoscale pH-sensing with polymer-coated gold nanorods'**
  I. Ament, J. Becker, C. Sönnichsen
  in preparation

- **'Single unlabeled protein detection on individual nanoparticles'**
  I. Ament, J. Prasad, A. Henkel, S. Schmachtel, C. Sönnichsen
  under review at *Nature Nanotechnology*